



**UCGE Reports  
Number 20324**

Department of Geomatics Engineering

**New Segmentation Algorithms for Dual and Full  
Polarimetric SAR Data**

(URL: <http://www.geomatics.ucalgary.ca/graduatetheses>)

by

**Mohammed Dabboor**

**January 2011**



UNIVERSITY OF CALGARY

NEW SEGMENTATION ALGORITHMS FOR DUAL AND FULL  
POLARIMETRIC SAR DATA

by

MOHAMMED DABBOOR

A THESIS

SUBMITTED TO THE FACULTY OF GRADUATE STUDIES  
IN PARTIAL FULFILMENT OF THE REQUIREMENTS FOR THE  
DEGREE OF DOCTOR OF PHILOSOPHY

DEPARTMENT OF GEOMATICS ENGINEERING

CALGARY, ALBERTA

JANUARY, 2011

© MOHAMMED DABBOOR 2011



## Abstract

Synthetic Aperture Radar (SAR) systems are effective tools for monitoring different land cover types. Radar systems are weather and sun illumination independent, two factors which usually inhibit the use of optical satellite imagery. This thesis investigates new segmentation methodologies for polarimetric SAR data. Two divisive segmentation methodologies are discussed, one for full polarimetric SAR data and a second one for dual polarized SAR data. The proposed methodologies for both cases, full and dual polarimetric SAR data, are nonparametric in terms of applying a nonparametric histogram thresholding algorithm. The proposed methodology for the full polarimetric case has the characteristic of preserving the information of the scattering mechanisms that the different land cover types represent.

A new agglomerative methodology is presented for full polarimetric SAR data segmentation. A new probabilistic distance is proposed for the agglomerative hierarchical merging of small clusters into an appropriate number of larger clusters. The proposed probabilistic distance measures the distance between two complex Wishart distributions, independently of the number of samples in each distribution.

The proposed methodologies, divisive and agglomerative, are developed so that they overcome drawbacks of existing segmentation approaches. The proposed methodologies are applied to SAR data from three spaceborne SAR systems, ALOS, TerraSAR-X and RADARSAT-2. For validation purposes, the segmentation results of the proposed methodologies are compared with results obtained by a number of recognized segmentation approaches. The comparison of results from the developed methods demonstrates significant improvements over conventional methods and overcome the drawbacks identified.

## Acknowledgements

This research work would not be possible without the invaluable help and guidance of a number of great people. I am indebted to my supervisors Prof. Dr. Michael Collins and Prof. Dr. Alexander Braun. Sincere and special thanks go to Prof. Dr. Vassilia Karathanassi from the Laboratory of Remote Sensing at the National Technical University of Athens, where important parts of this thesis were done during research visits there. All gave their best in providing me with a stimulating and relaxed environment. I deeply appreciate their support which was much more than scientific!

Many thanks go to Prof. Dr. Demetrius Rokos, Prof. Dr. Demetre Argialas, Dr. Polychronis Kolokousis, Christos Iossifides and Angelos Tzotzos from the Laboratory of Remote Sensing at the National Technical University of Athens for their useful help and discussions. Thanks to my examiners Dr. Michael Sideris, Dr. John Yackel and Dr. Samuel Foucher.

I wish to thank the Japanese Space Agency (JAXA) for providing the PALSAR ALOS SAR data, the German Space Agency (DLR) for providing the TerraSAR-X SAR data and the Canadian Space Agency (CSA) for providing the RADARSAT-2 SAR data. Furthermore, I gratefully acknowledge the financial support from the Natural Sciences and Engineering Research Council of Canada (NSERC) and the University of Texas at Dallas.

I do not want to forget to thank all the people in Greece and Canada who simply offered me their friendship and did not make me feel alone during my long academic trip (12 years!) far away from my family and my home country Palestine! Many thanks go to my friend Mohannad for the useful discussions we used to have. All my love goes to my father Darwish (the best mathematician ever!), my mother Nadia, my brothers and my darling Nehal.

*It's not that I'm so smart, it's just that I stay with problems longer.*

*Albert Einstein (1879-1955)*

*To my parents,*

*Darwish and Nadia*

## Table of Contents

Approval Page.....	ii
Abstract.....	iii
Acknowledgements.....	iv
Table of Contents.....	vi
List of Tables.....	viii
List of Figures and Illustrations.....	ix
Symbols and Abbreviations.....	xii
CHAPTER ONE: INTRODUCTION.....	1
1.1 Literature review.....	1
1.1.1 Approaches Based on Divisive Clustering.....	2
1.1.2 Approaches Based on Agglomerative Clustering.....	4
1.2 Motivation and Problem Statement.....	5
1.3 Research Objectives.....	6
1.4 Thesis Structure.....	7
CHAPTER TWO: BASIC POLARIMETRIC SAR CONCEPTS.....	8
2.1 Radar Polarimetry Historical Background.....	8
2.2 Polarimetric Scattering Vector.....	9
2.3 Deterministic and Non-deterministic Scatterers.....	11
2.4 Polarimetric Scattering Mechanisms.....	12
2.5 Polarimetric Decomposition Methods.....	15
2.5.1 The Pauli Decomposition method.....	17
2.5.2 The Cloude-Pottier Decomposition Method.....	18
2.5.3 The Freeman-Durden Decomposition Method.....	22
CHAPTER THREE: POLARIMETRIC SAR DATA AND STUDY AREAS.....	25
3.1 ALOS Full Polarimetric SAR Data.....	25
3.2 RADARSAT-2 Full Polarimetric SAR Data.....	28
3.3 TerraSAR-X Dual Polarized SAR Data.....	32
CHAPTER FOUR: POLARIMETRIC SAR DIVISIVE CLUSTERING.....	34
4.1 Introduction.....	34
4.2 Delon’s Histogram Thresholding Algorithm.....	35
4.3 Divisive Hierarchical Full Polarimetric SAR Segmentation.....	38
4.3.1 Methodology.....	38
4.3.2 Implementation.....	41
4.3.2.1 Pre-processing.....	41
4.3.2.2 First Segmentation Level.....	44
4.3.2.3 Second Segmentation Level.....	46
4.3.2.4 Third Segmentation Level.....	48
4.3.3 Comparison with the k-means Algorithm.....	49
4.4 Divisive Hierarchical Dual Polarimetric Segmentation.....	52
4.4.1 Methodology.....	52

4.4.2 Implementation.....	55
4.4.2.1 Preprocessing.....	55
4.4.2.2 Segmentation Results.....	56
4.4.2.3 Discussion.....	65
4.5 Summary.....	68
CHAPTER FIVE: POLARIMETRIC SAR AGGLOMERATIVE CLUSTERING .....	70
5.1 Introduction.....	70
5.2 Wishart Chernoff Probabilistic Distance .....	70
5.2.1 The Complex Wishart Distribution .....	70
5.2.2 Chernoff Error Bound.....	71
5.3 Agglomerative Clustering.....	78
5.3.1 Methodology.....	78
5.3.2 Implementation and Discussion .....	80
5.4 Application to RADARSAT-2 Full Polarimetric SAR Images .....	90
5.5 Summary.....	99
CHAPTER SIX: CONCLUSIONS AND FUTURE PERSPECTIVES .....	101
6.1 Conclusions.....	101
6.2 Future Perspectives .....	104
REFERENCES .....	105

## List of Tables

Table 2.1: Notable SAR missions.....	9
Table 2.2: Pauli matrices and their interpretation. ....	17
Table 3.1: System parameters of ALOS polarimetric mode.....	25
Table 3.2: System parameters of the quad-polarized mode of RADARSAT-2.....	28
Table 3.3: System parameters of TerraSAR-X polarimetric mode.....	32
Table 4.1: Number of segments for each segmentation case.....	50
Table 5.1: Error in classification in percent for selected land cover regions of the POLARSAR image. ....	89
Table 5.2: Number of classes, temperature and weather condition for each RADARSAT-2 image and acquisition time. Data source for temperature and weather condition data is the National Climate Data and Information Archive of Canada.....	90

## List of Figures and Illustrations

Figure 2.1: a) Scattering from smooth surface, b) Scattering from rough surface, c) Double bounce scattering, d) Volume scattering.....	13
Figure 2.2: Radar signal penetration for different bands.....	15
Figure 2.3: Backscattering decomposition into trihedral and two dihedrals with different tilt angles.....	18
Figure 2.4: The $\alpha$ angle values and the corresponding scattering mechanisms.....	20
Figure 2.5: Segmentation of the polarimetric SAR data based on the entropy and alpha angle.....	21
Figure 2.6: Segmentation of the polarimetric SAR data based on the entropy, alpha angle and anisotropy.....	22
Figure 3.1: a) RGB of the ALOS polarimetric SAR data (red = $T_{22}$ , green = $T_{33}$ , blue = $T_{11}$ ), b) AVNIR-2 RGB optical image of the study area (the study area is 83km N-S and 12km W-E), c) A map of the study area.....	27
Figure 3.2: Full polarimetric RADARSAT-2 data of Churchill acquired in: a) October 31, 2009, b) December 18, 2009, c) January 24, 2010, d) April 3, 2010, e) May 21, 2010, and f) July 22, 2010.....	29
Figure 3.3: a) SPOT image of the Churchill area, b) Map of Churchill.....	31
Figure 3.4: a) The TerraSAR-X HH image before speckle filtering, b) The VV image in the same area, c) Optical image of the study area (Source: Google Earth aerial image 31 May 2006).....	33
Figure 4.1: Three-mode scheme divided into three intervals.....	36
Figure 4.2: Flowchart of the proposed multilevel segmentation methodology based on input data from Pauli or Freeman-Durden analysis.....	41
Figure 4.3: Image segmentation by speckle filtering using the refined Lee filter.....	42
Figure 4.4: a) Polarimetric SAR image: Red = HH, Green = HV, Blue = VV, b) Data after removing speckle noise using the refined Lee filter three times, c) Pauli analysis images in RGB (Red = double bounce, Green = $45^\circ$ tilted double bounce, Blue = surface), d) Freeman-Durden analysis images in RGB (Red = double bounce, Green = volume, Blue = surface).....	43
Figure 4.5: a) First segmentation level of Pauli data, b) First segmentation level of Freeman-Durden data, c) Second segmentation level of Pauli data, d) Second	

segmentation level of Freeman-Durden data, e) Third segmentation level of Pauli data, f) Third segmentation level of Freeman-Durden data. ....	46
Figure 4.6: Variations of the amplitude values of the Surface scattering mechanism (dominant) for the subarea $S_{SV}^{FD}$ of the Freeman-Durden images.....	47
Figure 4.7: Segmentation based on the k-mean clustering algorithm. a) Segments produced based on Wishart k-means H/ $\alpha$ clustering, b) Segments produced based on Wishart k-means SPAN/H/ $\alpha$ /A clustering. ....	51
Figure 4.8: Sample region selected from the Southern end of the study area. a) Pauli case, b) Freeman-Durden case, c) Wishart k-means H/ $\alpha$ , d) Wishart k-means span/H/ $\alpha$ /A. ....	52
Figure 4.9: Scheme shows the concept of the proposed segmentation methodology that creates subspaces based on the thresholded histograms. ....	54
Figure 4.10: a) The HH+VV after speckle filtering using a refined Lee filter, b) The HH-VV after speckle filtering using a refined Lee filter. ....	56
Figure 4.11: Flowchart of the segmentation approach for dual polarized SAR data.....	57
Figure 4.12: The HH+VV and HH-VV thresholded histograms and the sub-spaces produced by combing them in a two dimensional histogram-based space. ....	58
Figure 4.13: The extracted borders (red colour) of the resulting segments overlain on a composited image (Green = HH+VV, Blue = HH-VV) for a) First segmentation level, b) Second segmentation level, c) Third segmentation level, d) Fourth segmentation level, (e) Fourth segmentation level produced by the <i>eCognition</i> . ....	64
Figure 4.14: a), c) and e) Sample areas from the final (fourth) segmentation level produced by histogram thresholding. b), d) and f) Sample areas from the final (fourth) segmentation level produced by <i>eCognition</i> . ....	67
Figure 5.1: a) The graph of $f(\beta)$ for two statistically: identical distributions (solid line), similar distributions (dashed line), and dissimilar distributions (dot-dashed line), b) The graph of $g(\beta)$ for two statistically: identical distributions (solid line), similar distributions (dashed line), and dissimilar distributions (dot-dashed line). ....	77
Figure 5.2: a) Plot of the data log-likelihood calculated using the Wishart Chernoff distance to merge clusters, b) Plot of the data log-likelihood calculated using the Wishart test statistic distance to merge clusters. ....	81
Figure 5.3: a) POLSAR data classification based on the Wishart Chernoff distance, b) POLSAR data classification based on the Wishart test statistic distance. ....	84

Figure 5.4: a1) Urban blocks as shown in a map of the study area, a2) Urban areas captured based on Wishart Chernoff distance, a3) Urban areas captured based on Wishart test statistic distance. ....	85
Figure 5.5: b1) Forests as shown in the map of the study area, b2) Forests as appear in the AVNIR-2 optical image of the study area, b3) Forest areas captured based on the Wishart Chernoff distance, b4) Forest areas captured based on the Wishart test statistic distance.....	86
Figure 5.6: c1) Optical image of the study area for reference, c2) Classified agricultural fields and croplands using Wishart Chernoff distance, (c3) Classified agricultural fields and croplands using Wishart test statistic distance.....	87
Figure 5.7: d1) Streams as shown in the map of the study area, d2) Streams captured based on the Wishart Chernoff distance, d3) Streams captured based on the Wishart test statistic distance. ....	88
Figure 5.8: Plot of the number of classes as a function of the acquisition time for each SAR image. ....	91
Figure 5.9: Segmentation results on top the SRTM 90m DEM of the Churchill area for the RADARSAT-2 images of: a) October 31, 2009, b) December 81, 2009, c) January 24, 2010, d) April 3, 2010, e) May 21, 2010 and July 22, 2010. ....	94
Figure 5.10: Three selected regions (R1, R2 and R3) in the study area for further investigation. ....	95
Figure 5.11: Sea ice extent of the Arctic, including Hudson Bay for: a) December 2009, b) January 2010, c) March 2010, d) May 2010, e) July 2010, and October 2010. Source: National Snow and Ice Data Center (NSIDC). ....	97
Figure 5.12: Pictures of Churchill show: a) Churchill River weir, b) Muskeg covered lake, c) Partially overgrown lake. ....	99

## Symbols and Abbreviations

HH	Horizontal transmit, horizontal receive
HV	Horizontal transmit, vertical receive
VH	Vertical transmit, horizontal receive
VV	Vertical transmit, vertical receive
H	Entropy
$\alpha$	Alpha angle
A	Anisotropy
S	Scattering matrix
$S_{ij}$	Complex scattering amplitude
$\vec{k}$	Scattering vector
$\vec{k}_B$	Scattering vector in lexicological basis
$\vec{k}_P$	Scattering vector in Pauli basis
$\Psi$	Basis matrices
C	Covariance matrix
$\langle \dots \rangle$	Spatial ensemble averaging
*	Complex conjugate
T	Coherency matrix
$\Lambda$	Diagonal eigenvalue matrix
$\lambda$	eigenvalue
U	Unitary matrix
$R_h, R_v$	Reflection coefficients
$R_{gh}, R_{gv}$	Fresnel reflection coefficients
$\gamma$	Phase change
$B(n, k, p)$	Binomial tail
h	Histogram
L	Number of bins in a histogram
N	Number of samples
D	Grenander operator
$\sigma$	Standard deviation
n	Number of looks
$p(T)$	Probability density function for complex Wishart distribution
$\Gamma(\dots)$	Gamma function
$E[T]$	Expected value of T
V	Cluster center coherency matrix
P	A priori probability
$\beta$	Chernoff parameter
$f(\beta)$	Wishart Chernoff distance
v, u	Polarization bases
+	Complex conjugate transpose
$L_m$	Data log-likelihood
m	Number of clusters
$d(V_i, V_j)$	Wishart test statistic distance

SAR	Synthetic Aperture Radar
InSAR	Synthetic Aperture Radar Interferometer
POLSAR	Polarimetric Synthetic Aperture Radar
POLSEGANN	Polarimetric Segmentation Annealing
POL MUM	Polarimetric Merge Using Moments
ML	Maximum Likelihood
MIRGS	Multivariate Iterative Region Growing with Semantics
SPAN	Total backscattering power
JPL	Jet Propulsion Laboratory
ESA	European Space Agency
JAXA	Japanese space agency
DLR	German space agency
CSA	Canadian Space Agency
NASA	National Aeronautics and Space Administration
ALOS	Advanced Land Observation Satellite
PRISM	Panchromatic Remote-sensing Instrument for Stereo Mapping
AVNIR-2	Advanced Visible and Near Infrared Radiometer type 2
PALSAR	Phased Array type L-band Synthetic Aperture Radar
DEM	Digital Elevation Model
ENL	Equivalent Number of Looks
Tr	Trace of a matrix
DRA	Dual Receive Antenna
MRF	Markov Random Field
SSC	Single look Slant range Complex
SLC	Single Look Complex
SRTM	Shuttle Radar Topographic Mission



## Chapter One: Introduction

Segmentation is the subdivision of an image into homogeneous segments (Acton et al., 1994). A single segment can either correspond to a semantic object in the image or its union with the surrounding segments can lead to such an object. Thus, a segment-based classification approach pre-requires the appropriate segmentation of the image data. For each segment, classification rules based on physical or geometrical parameters are defined and applied in order to assign a segment to a specific thematic class. Consequently, segmentation is the first major step in any object-oriented feature extraction approach and plays an essential role for the accuracy of any segment-based classification process (Dabboor and Karathanassi, 2005).

One of the main applications of Polarimetric Synthetic Aperture Radar (POLSAR) is the segmentation of different land cover types. However, segmentation of SAR data was always a difficult task due to the presence of speckle noise (Lee and Pottier, 2009).

Polarimetric SAR segmentation approaches should be able to exploit the additional scattering information that this data contain, in comparison with conventional optical or single-channel SAR data. First segmentation methods failed to utilize complete polarimetric information (Lee et al., 2004). These methods used only the intensities of HH, HV, and VV, the phase difference between HH and VV, the ratio of |HH| and |VV| (Kwok et al., 1991; Du et al., 1992), or the coefficient of variation (van Zyl et al., 1987), where H and V stand for horizontally and vertically polarized radar pulses, respectively. One exception was the use of the multivariate complex Gaussian distribution for the three complex polarimetric components, HH, HV and VV, for Bayes classification by Kong et al. (1988) and Lim et al. (1989).

### 1.1 Literature review

Different approaches have been proposed in the international literature for dual and full polarimetric SAR data. These approaches can be grouped into two major

categories: 1) Approaches based on divisive clustering and 2) Approaches based on agglomerative clustering. Divisive segmentation can be defined as top-down segmentation which splits the image into homogeneous regions/segments while agglomerative segmentation can be defined as a bottom-up approach of merging small clusters/segments of an image into an appropriate number of large clusters/segments (Agarwal et al., 2010). In divisive clustering, the final segmentation results can be obtained by dividing the image hierarchically or directly into final segments. Different criteria, such as the number of pixels in a cluster (Savaresi et al., 2002), cluster variance with respect to its centroid (Liang et al., 2010), etc., are used in divisive clustering as a selection criteria for further segmentation of clusters. In agglomerative clustering, data are initially segmented into small clusters/segments. Small clusters are merged hierarchically into an appropriate number of large clusters. Merging is performed based on a similarity criterion. Different types of distances, such as the Manhattan distance (Kersten et al., 2005), the Mahalannobis distance (Du et al., 2002), the Wishart test statistic distance (Cao et al., 2007), etc., are used to measure similarity, where clusters with the shortest distance are merged.

### ***1.1.1 Approaches Based on Divisive Clustering***

Many studies have been presented for full polarimetric SAR segmentation using the divisive clustering scheme. Lombardo and Oliver (2002) and Pellizzeri et al. (2003) discussed a segmentation approach, called Polarimetric Segmentation Annealing or POLSEGANN, based on the maximum generalised likelihood approach and the Wishart distribution model. A joint logarithmic likelihood function for the whole image, assuming that it composites a predefined number of homogeneous regions, is derived and used as objective function in the simulated annealing maximization technique. The POLSEGANN was found to be appropriate for small region identification (Pellizzeri et al., 2003). A drawback of the discussed segmentation technique is that it requires the predefinition of the number of homogeneous regions in the image, which is not always a simple task. In addition, the previously mentioned studies assume the absence of texture

(assume that areas are homogeneous), which is not always valid. Based on this assumption, the complex Wishart distribution is used. However, in the case where texture exists, the k-distribution is a better fit (Beaulieu and Touzi, 2004). In addition, it is not guaranteed that the resulting segments are homogeneous with regard to the scattering information. Thus, pixels of a single segment might exhibit different scattering mechanisms.

De Grandi et al. (2001) proposed a segmentation and labelling method of polarimetric SAR data based on a wavelet frame that works as a differential operator and generates piece-wise smooth approximations of the covariance matrix power term images. Segmentation of polarimetric SAR data into eight classes based on the entropy and alpha angle ( $H/\alpha$ ) plane was proposed in Cloude and Pottier (1997) and extended to sixteen classes by involving the anisotropy parameter ( $A$ ) by Pottier and Lee (1999). Herein, the two-dimensional space of  $H$  and  $\alpha$ , which becomes three-dimensional by including the anisotropy  $A$ , is divided into eight and sixteen zones, respectively, based on arbitrary fixed zone boundaries. This sometimes leads to noisy segmentation results. In addition, the total backscattering power information is not considered in the segmentation process. An attempt to improve the segmentation results was presented in Lee et al. (1999) by applying the k-means complex Wishart classifier and Park and Moon (2007) by applying the fuzzy concept.

It is important to mention that the previously discussed studies lack the concept of selective segmentation in the divisive clustering. Thus, segmentation of the polarimetric data is not performed hierarchically in a multilevel scheme where the user can choose the desired segmentation scale and has the choice of selecting segments of interest for further segmentation.

Segmentation approaches using divisive clustering were also applied on dual polarized data. Scheuchl et al. (2004) proposed an unsupervised segmentation algorithm for dual polarized data and tested its ability to distinguish sea ice types. The proposed algorithm uses the k-means Wishart classifier and a distance measure for pixel assignment. Segmentation performance using the proposed algorithm was found to be limited in the separation of different sea ice types. Another study tested dual polarized

SAR data of different ice types with a multivariate Gaussian maximum likelihood classifier and two neural network classifiers (Orlando et al., 1990). The Gaussian assumption was not always reasonable, especially for the case of icebergs. Neural networks classifiers were found to have a similar performance as the Gaussian classifier. Again, the user does not have the advantage of a multi-scaling approach which can be achieved by the multilevel segmentation of the data. Users can not select specific segments, which can be of interest for the case study, for further segmentation.

### ***1.1.2 Approaches Based on Agglomerative Clustering***

Different approaches for polarimetric SAR segmentation using the agglomerative clustering technique were also presented. Pellizzeri et al. (2003) discussed a segmentation approach, named Polarimetric Merge Using Moments (POL MUM), based on a Maximum Likelihood (ML) Split-Merge test between adjacent regions and a region growing scheme. A likelihood ratio test is used as merging criterion for segments. The POL MUM was found to be appropriate for homogeneous large region identification (Pellizzeri et al., 2003).

A hierarchical optimization process using small sets of pixels as segments was implemented (Beaulieu and Touzi, 2002). Segment pairs that minimize a stepwise criterion are merged. The proposed criterion is based upon the testing of the equality of covariance matrices of adjacent regions, by calculating their difference of determinant logarithms. An agglomerative clustering scheme using the  $H/A/\alpha$  and the additional information of the total backscattering power (SPAN) was discussed in Cao et al. (2007). Herein, the Wishart test statistic distance is used in order to merge clusters into an appropriate number of classes. The drawback of the used merging criteria in the previously discussed studies is that the used similarity criteria depend on the number of pixels in the tested clusters/segments. Thus, these criteria are reasonable when the tested segments have comparable number of pixels. A merging criterion independent of the number of pixels in each segment was used in Lee et al. (2001). Herein, the used criterion is based on the dispersion of the classes and the between-class distance. A hierarchical

stepwise optimization process was developed for polarimetric SAR segmentation based on a likelihood approximation approach (Beaulieu and Touzi, 2004). A stepwise optimization algorithm merges hierarchically the two segments that produce the smallest decrease in a defined log-likelihood function.

An agglomerative segmentation approach for dual polarized data, using the Mahalanobis distance was presented in Du et al. (2002). This approach is based on the statistics of both the amplitude variations and the textural characteristics of the dual polarized SAR data. Yu (2009) used the Multivariate Iterative Region Growing with Semantics (MIRGS) algorithm for dual polarized SAR data segmentation of sea ice. This algorithm is based on the Markov Random Field (MRF). A watershed over-segmentation is applied on the data to initialize the agglomerative clustering. A drawback of the MIRGS algorithm is that it is highly sensitive to the initial conditions (Qin and Clausi, 2010).

## **1.2 Motivation and Problem Statement**

It is stated clearly in the previous section that new segmentation methodologies are required to fill some of the existing gaps in the field of polarimetric SAR segmentation and overcome part of the drawbacks of the existing segmentation approaches. In the case of polarimetric SAR segmentation using the divisive clustering technique, a nonparametric segmentation approach can overcome the need to assume a statistical distribution for the data. Furthermore, the produced segments in the case of full polarimetric SAR should not only be homogeneous with regard to the amplitude values, but also with regard to the scattering information of the segment pixels. Continually, this scattering information can be used as additional polarimetric information for the later classification approach of segments into semantic objects. Multi-leveling in the segmentation approach will help the user to select the desired segmentation scale and choose segments of interest for further segmentation. Criteria can be defined to control the additional segmentation.

In the case of polarimetric SAR segmentation using the agglomerative clustering technique, a place still exists for a new distance criterion for merging segments. This criterion should be independent of the number of pixels in segments. Furthermore, it should better address the similarity of two clusters/segments. This can be achieved by a distance criterion which is based on the statistical characteristics of the distributions of clusters under investigation.

### **1.3 Research Objectives**

This research study has two main objectives:

- 1) The development of new divisive segmentation methodologies, for full and dual polarimetric SAR data, that go beyond the traditional segmentation methods and overcome the pre-mentioned drawbacks.

The following secondary objectives are defined to reach the first main objective:

- Establish new divisive segmentation methodologies without a priori assumption about the underlying density function.
  - Establish new divisive segmentation methodologies that work hierarchically in a multilevel scheme.
  - For the case of full polarimetric SAR, develop a divisive segmentation approach which includes the analysis images produced by polarimetric decomposition methods in order to consider and maintain the information of the scattering mechanisms in the segmentation process.
- 2) The proposal of a new probabilistic distance for polarimetric SAR segmentation using agglomerative clustering, which can better quantify the similarity between clusters.

The following secondary objectives are defined to reach the second main objective:

- Derive a probabilistic distance criterion that measures statistically the similarity between two complex Wishart distributions.
- Derive a probabilistic distance criterion that is independent of the number of samples (pixels) in each distribution.

#### **1.4 Thesis Structure**

Besides to this introduction chapter, this thesis contains five additional chapters. Chapter 2 explores the basic polarimetric SAR concepts, including the polarimetric SAR decomposition methods which were involved in this research. Chapter 3 presents the full and dual polarimetric SAR data used. Also, the study areas are discussed. Chapter 4 deals with the development of two divisive segmentation methodologies for full and dual polarimetric SAR data. In Chapter 5, a new probabilistic distance, the Wishart Chernoff distance, is derived and included in an agglomerative clustering approach for the unsupervised segmentation of full polarimetric SAR data. A final chapter is dedicated to the presentation of the main findings and conclusions of this research, with an assessment of the aimed objectives and some recommendations for future work.

## Chapter Two: Basic Polarimetric SAR Concepts

In this chapter, a brief background about radar polarimetry is provided. Fundamental concepts related to polarimetric scattering matrix and vector are discussed. Moreover, the basic polarimetric decomposition methods are presented.

### 2.1 Radar Polarimetry Historical Background

The earliest studies on polarimetric radar firstly appeared at the end of the forties. The concept of radar polarimetry initiated by the important work of Sinclair (1950) who introduced the scattering matrix (also known Sinclair matrix). Later pioneering work was done by Kennaugh (1952), who defined the concept of optimal polarization for a target in the monostatic case and whose ideas were the basis of further advances throughout the fifties and sixties, and by Huynen (1970), who introduced the concept of target decomposition and generated the first decomposition techniques. Their work was taken up by Boerner (1981), who theoretically demonstrated the importance of polarization in various inverse problems at different frequency bands.

The availability of the first polarimetric SAR data acquired by the NASA/JPL AIRSAR imaging polarimetric system (van Zyl et al., 1992) was a fundamental turning point in radar polarimetry. Since the launch of the Seasat satellite in 1978, several SAR missions have been operating. Notable missions are summarized in Table 2.1.

When two or more coherent SAR images of the same scene are formed from slightly different look directions, the complex correlation between pairs of images can be evaluated and the system is said to operate as a SAR interferometer (InSAR) (Lavalle, 2009). Graham (1974) presented firstly the basic principles of InSAR. The first attempt of single-pass interferometry is attributed to Zebker and Goldstein (1986). The twin ESA satellites ERS-1/2 allowed the demonstration of repeat-pass interferometry.

Satellite	Band	Agency	Year launched
Seasat	L	Jet Propulsion Laboratory (JPL)	1978
SIR-C	C	National Aeronautics and Space Administration (NASA)	1994
ERS-1/2	C	European Space Agency (ESA)	1991 and 1995
J-ERS	L	Japanese Space Agency (JAXA)	1992
RADARSAT-1/2	C	Canadian Space Agency (CSA)	1995 and 2007
ENVISAT/ASAR	C	ESA	2002
ALOS/PALSAR	L	JAXA	2006
TerraSAR-X	X	German Aerospace Center (DLR)	2009
TanDEM-X	X	DLR	2010

**Table 2.1: Notable SAR missions**

## 2.2 Polarimetric Scattering Vector

A scattering matrix  $S$  is an array of four complex elements that describes the transformation of the polarization of a wave pulse incident upon a reflective medium to the polarization of the backscattered wave. The scattering matrix  $S$  contains information about the radar target (Hellmann, 1999).

$$S = \begin{bmatrix} S_{HH} & S_{HV} \\ S_{VH} & S_{VV} \end{bmatrix} \quad (2-1)$$

where  $S_{ij}$  are the complex scattering amplitude (the first subscript represents the polarization of the incident wave, and the second the polarization of the scattered wave). Its elements are, in general, complicated and sensitive function of frequency, target orientation and shape, relative orientation of the polarization planes in the bistatic case, etc. (Alberga, 2004). The diagonal elements  $S_{HH}$  and  $S_{VV}$  are called co-polarized elements, while the off-diagonal elements  $S_{HV}$  and  $S_{VH}$  are called cross-polarized elements.

Polarimetric scattering can be alternatively addressed in a vectorial formulation. Thus, instead of the matrix notation, one may use a four-element-complex vector  $\vec{k}$  which contains the complete information of the scattering matrix  $S$ , (Hellmann, 1999; Papathanassiou, 1999)

$$\vec{k} = \frac{1}{2} \text{Tr}([S]\Psi) \quad (2-2)$$

where  $\text{Tr}$  denotes the trace of a matrix (the sum of its diagonal elements), and  $\Psi$  is a complete set of  $2 \times 2$  complex basis matrices under a hermitian inner product. Two bases are widely used in the literature. The first one is the lexicographical basis which contains the following four basis matrices (Papathanassiou, 1999)

$$\Psi_B = \left\{ 2 \begin{bmatrix} 1 & 0 \\ 0 & 0 \end{bmatrix}, 2 \begin{bmatrix} 0 & 1 \\ 0 & 0 \end{bmatrix}, 2 \begin{bmatrix} 0 & 0 \\ 1 & 0 \end{bmatrix}, 2 \begin{bmatrix} 0 & 0 \\ 0 & 1 \end{bmatrix} \right\}. \quad (2-3)$$

The corresponding scattering vector  $\vec{k}_B$ , obtained using the lexicological basis is

$$\vec{k}_B = [S_{HH}, S_{HV}, S_{VH}, S_{VV}]^T \quad (2-4)$$

where  $^T$  denotes the transpose of the vector. This scattering vector contains the complex amplitudes of the scattering matrix. Thus, it is related directly to the system measurable (Hellmann, 1999).

The second important basis is the Pauli, which is formed by the Pauli spin matrices (Cloude and Pottier, 1996)

$$\Psi_P = \left\{ \sqrt{2} \begin{bmatrix} 1 & 0 \\ 0 & 1 \end{bmatrix}, \sqrt{2} \begin{bmatrix} 1 & 0 \\ 0 & -1 \end{bmatrix}, \sqrt{2} \begin{bmatrix} 0 & 1 \\ 1 & 0 \end{bmatrix}, \sqrt{2} \begin{bmatrix} 0 & -i \\ i & 0 \end{bmatrix} \right\}. \quad (2-5)$$

The corresponding scattering vector  $\vec{k}_P$ , obtained using the Pauli basis, is

$$\vec{k}_P = \frac{1}{\sqrt{2}} [S_{HH} + S_{VV}, S_{HH} - S_{VV}, S_{HV} + S_{VH}, i(S_{VH} - S_{HV})]^T. \quad (2-6)$$

The advantage of the Pauli basis is that the obtained scattering vector is closely related to the physics of the wave scattering.

In the case of backscattering in a reciprocal medium, the scattering matrix is symmetric, i.e.,  $S_{HV} = S_{VH}$ . Consequently, the four-dimensional scattering vector in its representation in lexicological basis can be reduced to a three-dimensional vector

$$\vec{k}_B = [S_{HH}, \sqrt{2}S_{HV}, S_{VV}]^T. \quad (2-7)$$

For the Pauli basis, the scattering vector takes the explicit form

$$\vec{k}_P = \frac{1}{\sqrt{2}} [S_{HH} + S_{VV}, S_{HH} - S_{VV}, 2S_{HV}]^T. \quad (2-8)$$

Both scattering vectors contain the same information only in different representations.

### 2.3 Deterministic and Non-deterministic Scatterers

Deterministic scatterers can be described completely by a single scattering matrix or vector. For remote sensing SAR applications, the assumption of pure deterministic scatterers is not valid. Thus, scatterers are non-deterministic and can not be described with a single scattering matrix or vector. This is because the resolution cell is bigger than the wavelength of the incident wave. Non-deterministic scatterers are spatially distributed. Therefore, each resolution cell is assumed to contain many deterministic scatterers, where each of these scatterers can be described by a single scattering matrix  $S_i$ . Therefore, the measured scattering matrix  $S$  for one resolution cell consists of the coherent superposition of the individual scattering matrices  $S_i$  of all the deterministic scatterers located within the resolution cell (Papathanassiou, 1999).

An ensemble average of the complex product between the lexicological scattering vector  $\vec{k}_B$  and  $\vec{k}_B^{*T}$  leads to the so-called polarimetric covariance matrix  $C$ , (Touzi et al., 2004).

$$C = \langle \vec{k}_B \cdot \vec{k}_B^{*T} \rangle = \begin{bmatrix} \langle |S_{HH}|^2 \rangle & \sqrt{2} \langle S_{HH} S_{HV}^* \rangle & \langle S_{HH} S_{VV}^* \rangle \\ \sqrt{2} \langle S_{HV} S_{HH}^* \rangle & 2 \langle |S_{HV}|^2 \rangle & \sqrt{2} \langle S_{HV} S_{VV}^* \rangle \\ \langle S_{VV} S_{HH}^* \rangle & \sqrt{2} \langle S_{VV} S_{HV}^* \rangle & \langle |S_{VV}|^2 \rangle \end{bmatrix} \quad (2-9)$$

where  $\langle \dots \rangle$  denotes a spatial ensemble averaging assuming homogeneity of the random scattering medium and  $*$  the complex conjugate. Analogously, the so-called polarimetric coherency matrix  $T$  is formed using the outer product of the Pauli scattering vector  $\vec{k}_P$

$$T = \langle \vec{k}_P \cdot \vec{k}_P^{*T} \rangle = \begin{bmatrix} \langle |S_{HH} + S_{VV}|^2 \rangle & \langle (S_{HH} + S_{VV})(S_{HH} - S_{VV})^* \rangle & 2 \langle ((S_{HH} + S_{VV})S_{HV}^*) \rangle \\ \langle (S_{HH} - S_{VV})(S_{HH} + S_{VV})^* \rangle & \langle |S_{HH} - S_{VV}|^2 \rangle & 2 \langle ((S_{HH} - S_{VV})S_{HV}^*) \rangle \\ 2 \langle (S_{HV}(S_{HH} + S_{VV})^*) \rangle & 2 \langle (S_{HV}(S_{HH} - S_{VV})^*) \rangle & 4 \langle |S_{HV}|^2 \rangle \end{bmatrix} \quad (2-10)$$

The relationship between the covariance matrix  $C$  and the coherency matrix  $T$  is linear. Both matrices are full rank, hermitian positive semidefinite and have the same real non-negative eigenvalues but different eigenvectors. Moreover, both matrices contain the complete information about variance and correlation for all the complex elements of the scattering matrix  $S$ , (Hellmann, 1999).

## 2.4 Polarimetric Scattering Mechanisms

In a radar image, each pixel represents an estimate of the radar backscattering from the corresponding area in the ground. Brighter areas in a radar image represent high backscattering due to the fact that larger fraction of the radar energy is reflected back to the radar while darker areas indicate that less energy is reflected. Backscattering recorded on the image is a function of the surface roughness. In the scale of most remote sensing

wavelengths, vegetation is treated as a rough surface and appears grey or light grey in a radar image. In urban areas, where the transmitted radar waves are able to bounce off the streets and then again bounce off the buildings (double bounce) and return back to the radar, they appear very bright in the radar image. Smooth surface, e.g., non wavy ocean, appears dark because of the reflection of the incident waves away from the radar. Four types of scattering mechanisms are discussed below, the smooth surface, rough surface, double bounce and volume scattering mechanisms; see Figure 2.1.

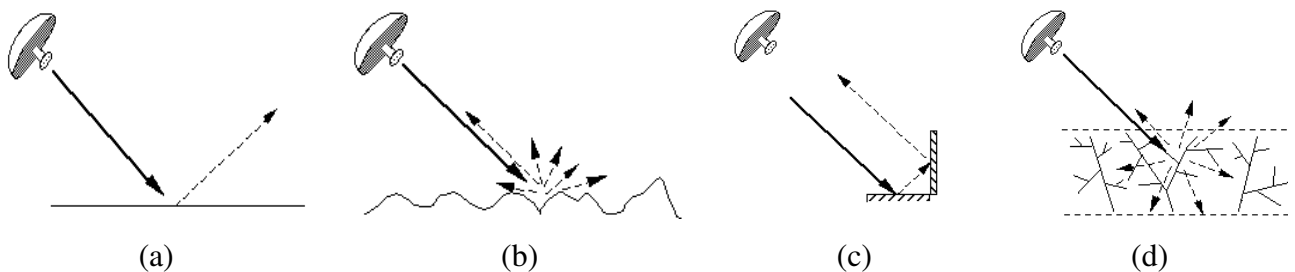


**Figure 2.1: a) Scattering from smooth surface, b) Scattering from rough surface, c) Double bounce scattering, d) Volume scattering.**

- Smooth Surface Scattering

The incident waves on a smooth surface are reflected in the forward direction away from the radar, Figure 2.1a. Only a small fraction of the radar energy is returned back to the radar antenna. Thus, smooth surfaces appear dark in the radar images. However, when a smooth surface is tilted towards the radar, almost all the energy is returned back to the radar and the backscattering will be very high. Smooth rocks, water and bare soil are the types of surfaces that would show smooth surface scattering.

- Rough Surface Scattering

As shown in Figure 2.1b, the incident waves on a rough surface are scattered in all directions. Part of the incident waves is reflected back to the radar antenna. The rougher the surface is, the higher the backscattered signals. Thus, rough surfaces appear

bright in a radar image. Surfaces, such as wavy ocean and soil with clumps, behave as rough surfaces.

- Double Bounce Scattering

In this case, the incident waves hit two surfaces, horizontal and adjacent vertical, and almost all of incident waves return back to the radar antenna, Figure 2.1c. Thus, the backscattering from areas with double bounce scattering is very high. Double bounce scattering occurs commonly in urban areas where roads and buildings, representing horizontal and adjacent vertical surfaces, are existed.

- Volume Scattering

Volume scattering is caused by randomly oriented scatterers, such as vegetations and forest canopy. As shown in Figure 2.1d, the incident waves penetrate the vegetation layer or forest canopy, where scatterers are randomly oriented in all directions, and get scattered partially back to the radar antenna. Volume scattering gives rise to the cross polarization (HV or VH).

In general, the penetration capabilities and the attenuation depth of a radar signal in a medium, such as soil or forest canopy, increase with the increasing of the signal wavelength (Grandjean et al., 2001). Figure 2.2 presents the penetration of radar signals for different bands. As shown in Figure 2.2, a forest area exhibits volume scattering in the case of C-band signals due to the fact that signal penetration is limited, and thus the scattering process takes place in the forest canopy. In the case of L-band signals, the penetration capabilities are high. Herein, the scattering process is from trunk-ground interaction (double bounce). Very rough surfaces exhibit volume scattering in the case of short wavelength signals, X-band.

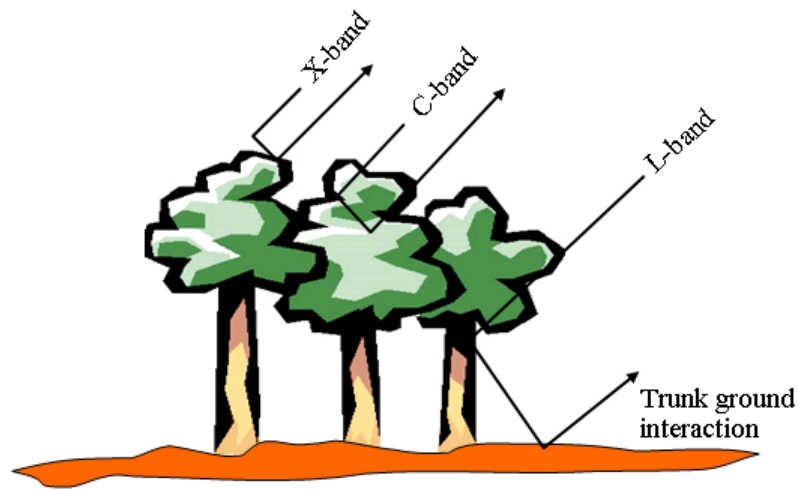


**Figure 2.2: Radar signal penetration for different bands.**

## 2.5 Polarimetric Decomposition Methods

The main characteristic of SAR polarimetry is that it allows the discrimination of different types of scattering mechanisms (Zhang et al., 2010). This becomes possible because the observed polarimetric signatures depend mainly on the actual scattering process. In comparison to conventional single-channel SAR, the inclusion of SAR polarimetry consequently can lead to a significant improvement in the quality of classification and segmentation results (Reigber, 2001). Certain polarimetric scattering models (Cloude and Pottier, 1996) even provide a direct physical interpretation of the scattering process, allowing an estimation of physical ground parameters like soil moisture and surface roughness (Cloude et al., 1999), as well as unsupervised classification methods with automatic identification of different scatterer characteristics and target types.

The objective of target decomposition theory is to express the average scattering mechanism as the sum of independent elements to associate a physical mechanism with each component (Touzi et al., 2004). Therefore, the polarimetric decomposition techniques split the backscattered signal into a sum of scattering contributions with orthogonal polarimetric signatures (Cloude and Pottier, 1996). This can be used for

extracting the corresponding target types in the SAR image. Thus, different decomposition approaches have been proposed in order to analyze and interpret SAR polarimetric images. They are based either on the complex voltage reflection matrix, like Pauli, or on power reflection matrix, like the covariance or coherency matrix. They produce polarimetric parameters which are appropriate to retrieve information on the scattering process of the target (Cloude and Pottier, 1996)

Target decomposition theories can be distinguished into coherent and incoherent (Lee and Pottier, 2009). Coherent target decomposition is applicable when the scattered wave is completely polarized. Consequently, coherent decomposition techniques, such as the Pauli (Cloude and Pottier, 1996), the sphere/deplane/helix (Krogager and Czyz, 1995) and the Cameron decomposition (Cameron et al., 1996), can be applied in the case where the radar target is deterministic. On the other hand, incoherent target decomposition is applicable when the scattered wave is partially polarized. Consequently, incoherent decomposition techniques, such as the Cloude-Pottier (Cloude and Pottier, 1997), the Freeman-Durden (Freeman and Durdan, 1998), the Moriyama decomposition (Moriyama et al., 2005), can be applied in the case where the radar target is non-deterministic.

The Cameron decomposition is applicable to bright discrete targets in a scene where speckle is not a problem (Cameron et al., 1996). In the case of sphere/deplane/helix decomposition, speckle filtering can not be applied. The Moriyama decomposition method is fit for urban areas and can be used for urban structure extraction (Moriyama et al., 2005). Thus, in this research, the Pauli, Freeman-Durden, and Cloude-Pottier decomposition methods are considered in the proposed segmentation methodologies. The analysis images of Pauli and Freeman-Durden are used as input in a multilevel segmentation approach (Chapter 4). The three polarimetric parameters of Cloude-Pottier decomposition are involved in an agglomerative clustering approach for unsupervised segmentation of polarimetric SAR data. Below, the three decomposition methods considered in this research are discussed.

### 2.5.1 The Pauli Decomposition method

The Pauli decomposition method is one of the basic SAR polarimetric data analysis methods. It is a coherent decomposition method where the target scattering matrix is expressed in terms of the Pauli matrices (Cloude and Pottier, 1996). These matrices correspond to elementary scattering mechanisms that lead to a physical interpretation of the scattering process. This method interprets the surface, double bounce and 45° tilted double bounce scattering mechanisms, Table 2.2.

Pauli matrix	Scattering mechanism	Interpretation
$\begin{bmatrix} 1 & 0 \\ 0 & 1 \end{bmatrix}$	surface	Surface, sphere, trihedral
$\begin{bmatrix} 1 & 0 \\ 0 & -1 \end{bmatrix}$	double bounce	dihedral
$\begin{bmatrix} 0 & 1 \\ 1 & 0 \end{bmatrix}$	45° tilted double bounce	45° tilted dihedral

**Table 2.2: Pauli matrices and their interpretation.**

The Pauli components are computed as follows:

$$\text{Pauli1 (double bounce)} = S_{HH} - S_{VV}$$

$$\text{Pauli2 (45° tilted double bounce)} = 2S_{HV}$$

$$\text{Pauli3 (surface)} = S_{HH} + S_{VV}$$

Thus, the backscattering from a general target can be seen as the sum of backscatter from a trihedral and two dihedrals with different tilt angles, Figure 2.3.

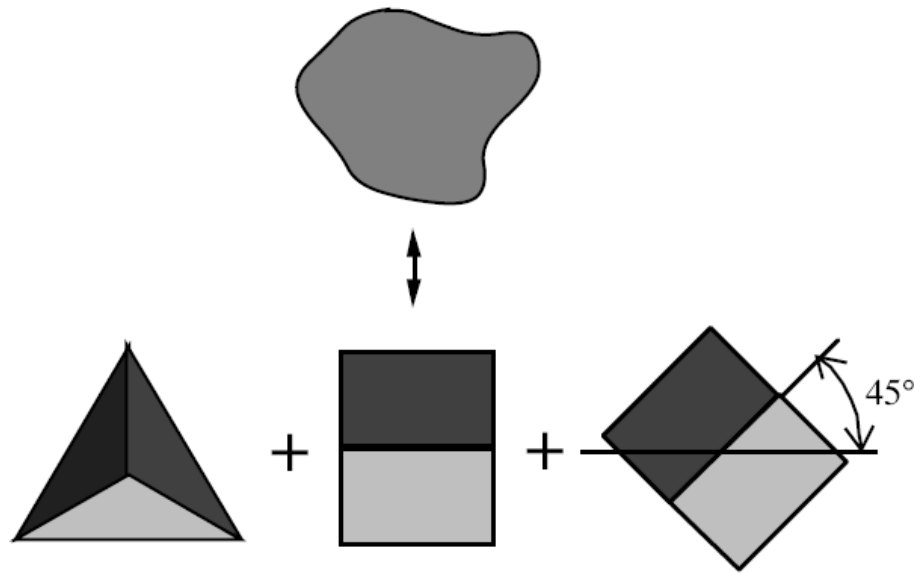


**Figure 2.3: Backscattering decomposition into trihedral and two dihedrals with different tilt angles.**

Although the Pauli decomposition method is coherent, it is used in the case of non-deterministic targets. Herein, the Pauli decomposition is called Pauli representation and the resulting analysis images can be used for polarimetric SAR segmentation (Karathanassi and Dabboor, 2004; Dabboor and Karathanassi, 2005; Lee et al., 2001; Dabboor et al., 2010a; Duquenoy et al., 2009; Kourgli et al., 2010). The advantage of the Pauli decomposition is that it is simple and yields a lot of information about the data (Hellmann, 1999). The practical disadvantage of the Pauli decomposition is that the double bounce scattering mechanism shows up in two different components, one that represents an unrotated dihedral and another represents a  $45^\circ$  tilted dihedral (Hellmann, 1999).

### ***2.5.2 The Cloude-Pottier Decomposition Method***

The Cloude-Pottier decomposition method is incoherent decomposition method based on the eigenvector/eigenvalue analysis of the coherency matrix  $T$  and was presented by Cloude and Pottier (1997). Due to the fact that the coherency matrix  $T$  is

hermitian positive semidefinite matrix, it can always be diagonalized using unitary similarity transformations. That is, the coherency matrix can be given as

$$T = U\Lambda U^*T = U \begin{bmatrix} \lambda_1 & 0 & 0 \\ 0 & \lambda_2 & 0 \\ 0 & 0 & \lambda_3 \end{bmatrix} U^*T \quad (2-11)$$

where  $\Lambda$  is the diagonal eigenvalue matrix of  $T$ ,  $\lambda_1 \geq \lambda_2 \geq \lambda_3 \geq 0$  are the real eigenvalues and  $U$  is a unitary matrix whose columns correspond to the orthogonal eigenvectors of  $T$ .

$$U = \begin{bmatrix} \cos \alpha_1 & \cos \alpha_2 & \cos \alpha_3 \\ \sin \alpha_1 \cos \beta_1 e^{j\delta_1} & \sin \alpha_2 \cos \beta_2 e^{j\delta_2} & \sin \alpha_3 \cos \beta_3 e^{j\delta_3} \\ \sin \alpha_1 \sin \beta_1 e^{j\gamma_1} & \sin \alpha_2 \sin \beta_2 e^{j\gamma_2} & \sin \alpha_3 \sin \beta_3 e^{j\gamma_3} \end{bmatrix} \quad (2-12)$$

where  $\beta$  and  $\alpha$  represents the orientation of the radar target about the radar line of sight and the alpha angle, respectively.

Important parameters can be derived based on the Cloude-Pottier decomposition. The entropy (H) is defined by the logarithmic sum of the eigenvalues (Cloude and Pottier, 1997):

$$H = -P_1 \log_3 P_1 - P_2 \log_3 P_2 - P_3 \log_3 P_3 \quad \text{where } P_i = \frac{\lambda_i}{\sum_{j=1}^3 \lambda_j} \quad (2-13)$$

This parameter is an indicator of the number of effective scattering mechanisms that take place in the scattering process, whereby  $H = 0$  belongs to deterministic scattering and  $H = 1$  to totally random scattering (Lee and Pottier, 2009).

The anisotropy (A), the second physical feature, describes the proportions between the secondary scattering mechanisms (Pottier and Pottier, 1999):

$$A = \frac{\lambda_2 - \lambda_3}{\lambda_2 + \lambda_3}. \quad (2-14)$$

The anisotropy  $A$  yields additional information only for medium values of  $H$ . A high anisotropy signifies that besides the first scattering mechanism only one secondary process contributes to the radar signal. A low anisotropy signifies that both secondary scattering processes play an important role.

Another polarimetric parameter is the alpha angle ( $\alpha$ ), which represents the type of the scattering mechanism and ranges between  $0$  and  $90^\circ$ . It is evaluated as (Cloude and Pottier, 1997):

$$\alpha = P_1\alpha_1 + P_2\alpha_2 + P_3\alpha_3. \quad (2-15)$$

$\alpha = 0$  indicates surface scattering, Figure 2.4. As the  $\alpha$  angle increases, the surface becomes anisotropic. An  $\alpha$ -value of  $45^\circ$  represents a dipole scattering. If  $\alpha$  reaches  $90^\circ$ , the scattering process is characterized by double bounce interactions.

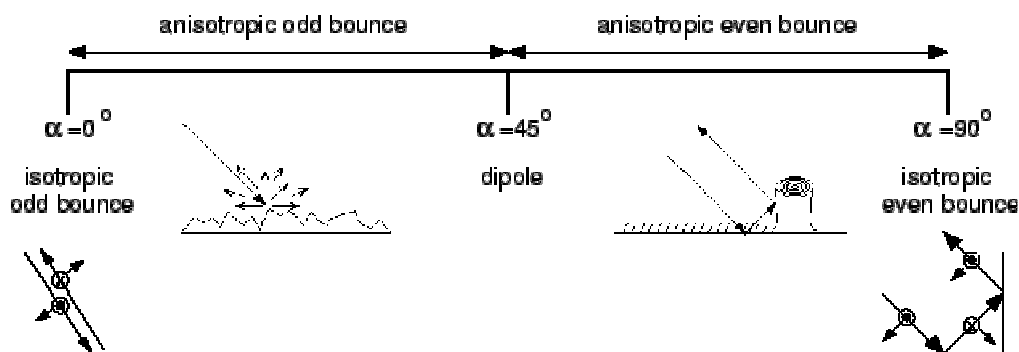


**Figure 2.4: The  $\alpha$  angle values and the corresponding scattering mechanisms.**

The three parameters of the Cloude-Pottier decomposition are widely used in the unsupervised segmentation of polarimetric SAR data (Hellmann, 1999; Cloude and Pottier, 1997; Dabboor and Karathanassi, 2005; Park and Moon, 2007; Lee et al., 1999a; Cao et al., 2007; Pottier and Lee, 1999).

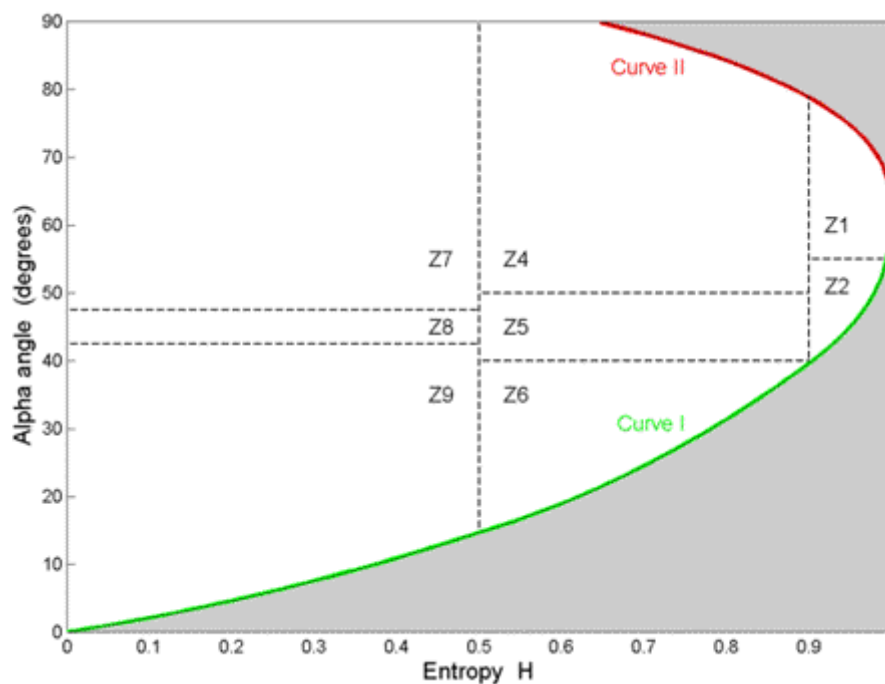


**Figure 2.5: Segmentation of the polarimetric SAR data based on the entropy and alpha angle.**

The entropy and alpha parameter can be combined together in a two-dimensional space. The two-dimensional space can be divided into eight zones (Cloude and Pottier, 1997) providing an unsupervised classification of the polarimetric SAR data into eight classes, Figure 2.5. The eight zones become sixteen by involving the anisotropy parameter and producing a three-dimensional space of the entropy, alpha angle and anisotropy (Pottier and Pottier, 1999). In this case, the polarimetric SAR data can be segmented into sixteen classes, Figure 2.6. Zone boundaries in the two/three-dimensional space are arbitrary fixed, resulting in noisy segmentation results (Lee et al., 1999a). However, the resulting segmentation is usually used as initial segmentation in different Polarimetric SAR segmentation algorithms (Lee et al., 1999a; Park and Moon, 2007; Cao et al., 2007; Dabboor et al., 2010c).

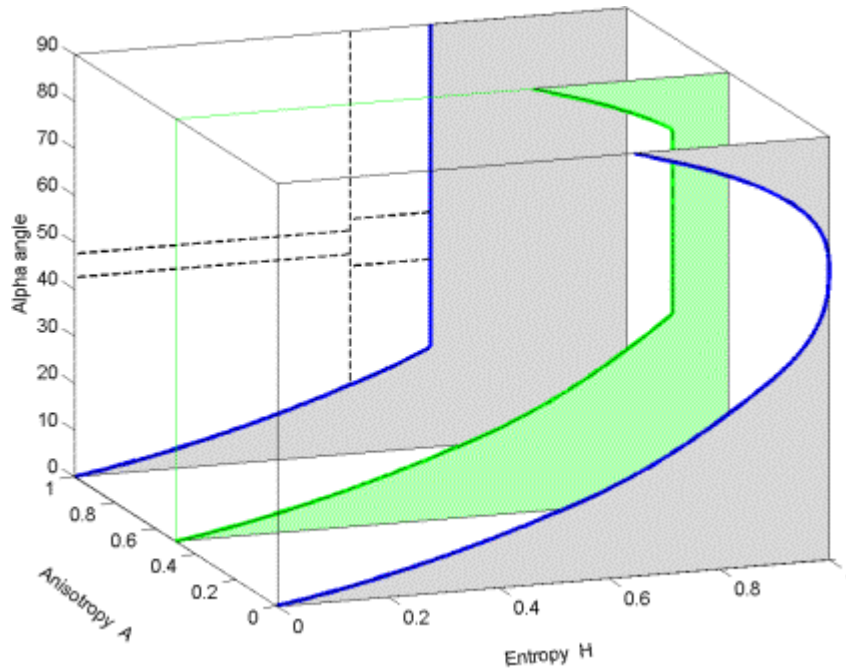


**Figure 2.6: Segmentation of the polarimetric SAR data based on the entropy, alpha angle and anisotropy.**

### 2.5.3 The Freeman-Durden Decomposition Method

This decomposition method is particularly well adapted to the study of vegetated areas and relies on the conversion of a covariance matrix to a three-component model. The results of this decomposition are three coefficients corresponding to the weights of different model components. A 3x3 covariance matrix  $C$  can be decomposed to a sum of three components, corresponding to volume scattering, surface scattering and double bounce scattering, (Freeman and Durdan, 1998)

$$C = f_v[C]_v + f_s[C]_s + f_d[C]_d. \quad (2-16)$$

The volume scattering component is obtained by averaging an oriented dipole canonical covariance matrix  $U(\phi)$  over a constant distribution of the azimuthal orientation angle between  $-180^\circ$  and  $180^\circ$ .

$$[C]_v = U(\phi) \begin{bmatrix} 1 & 0 & 0 \\ 0 & 0 & 0 \\ 0 & 0 & 0 \end{bmatrix} U(\phi)^{-1} = \begin{bmatrix} 1 & 0 & 1/3 \\ 0 & 1/3 & 0 \\ 1/3 & 0 & 1 \end{bmatrix} \quad (2-17)$$

The surface scattering term is directly parameterized using the first order Sinclair matrix of a horizontal rough surface (Freeman and Durdan, 1998)

$$S = \begin{bmatrix} R_h & 0 \\ 0 & R_v \end{bmatrix} \Rightarrow [C]_s = \begin{bmatrix} |\beta|^2 & 0 & \beta \\ 0 & 0 & 0 \\ \beta & 0 & 1 \end{bmatrix} \text{ where } \beta = \frac{R_h}{R_v} \in \mathfrak{R}. \quad (2-18)$$

$R_h$  and  $R_v$  are the reflection coefficients for horizontal and vertical polarization, respectively.  $\mathfrak{R}$  denotes the set of all real numbers. The double bounce scattering term is built from the Sinclair matrix of a Fresnel double bounce reflection (Freeman and Durdan, 1998)

$$S = \begin{bmatrix} e^{i2\gamma_v} R_{gv} R_{tv} & 0 \\ 0 & e^{i2\gamma_h} R_{gh} R_{th} \end{bmatrix} \Rightarrow [C]_d = \begin{bmatrix} |\alpha|^2 & 0 & \alpha \\ 0 & 0 & 0 \\ \alpha & 0 & 1 \end{bmatrix} \quad (2-19)$$

where  $\alpha = e^{i2(\gamma_h - \gamma_v)} (R_{gh} R_{th} / R_{gv} R_{tv})$ .

$R_{th}$  and  $R_{tv}$  are the reflection coefficients of the vertical surface (e.g., the trunk) for horizontal and vertical polarization, respectively;  $R_{gh}$  and  $R_{gv}$  are the Fresnel reflection coefficients of the horizontal surface (the ground) and  $\gamma$  are complex numbers, which represent any attenuation and phase change of the vertically and horizontally polarized waves as they propagate from the radar to the ground and back again.

The advantage of the Freeman-Durden decomposition method is that it is a model-fitting approach based on the physics of radar scattering, not a purely mathematical construct (Pottier and Ferro-Famil, 2009). However, this decomposition method was developed under the assumption of reflection symmetry that makes its results

not roll invariant. Variations of targets' orientations with respect to the radar look direction may cause misclassification (Lee et al., 2004). For example, buildings not aligned facing the radar look direction do not induce double bounce scattering, and they are categorized as volume scattering because of the higher cross-polarization returns.

### Chapter Three: Polarimetric SAR Data and Study areas

In this chapter, the polarimetric SAR data used in this research are presented. In addition, the study areas considered in this thesis are introduced. Three polarimetric data sets are used herein. Two sets of full polarimetric SAR data acquired by the Japanese Advanced Land Observation Satellite (ALOS) and the Canadian RADARSAT-2 satellite and a third set of dual polarized SAR data acquired by the German satellite TerraSAR-X. The TerraSAR-X satellite includes a full polarimetric SAR mode. However, this mode is still in an experimental stage.

#### 3.1 ALOS Full Polarimetric SAR Data

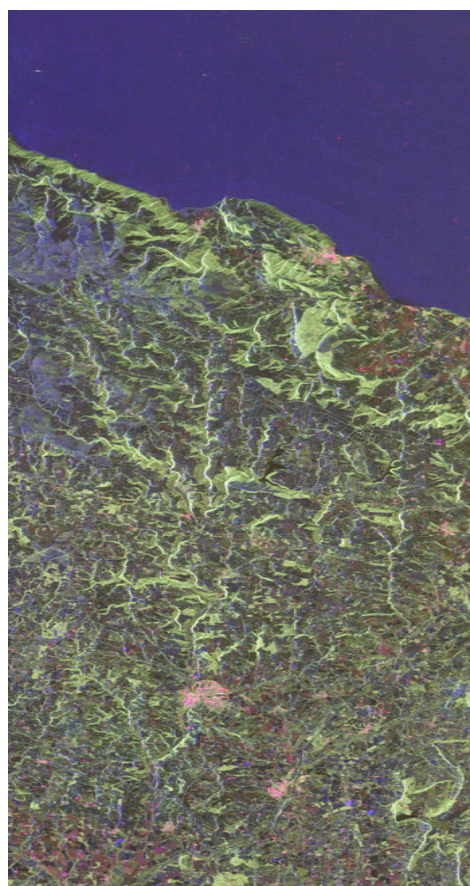
The ALOS satellite carries a spaceborne polarimetric SAR sensor and was successfully launched in January 2006. It has three remote-sensing instruments: the Panchromatic Remote-sensing Instrument for Stereo Mapping (PRISM) for Digital Elevation Models (DEMs), the Advanced Visible and Near Infrared Radiometer type 2 (AVNIR-2) for precise land coverage observation, and the Phased Array type L-band (wavelength: 15-30 cm, frequency: 2.000-1.000 MHz) Synthetic Aperture Radar (PALSAR) for day-and-night and all-weather Earth surface observation. Since the ALOS full polarimetric SAR data will be used in this thesis, the polarimetric mode of the satellite is reviewed here. Table 3.1 summarizes the system parameters of the polarimetric mode (Shimada et al., 2005).



System Parameters	Values
Off nadir angles	7.9° – 30.1°
Swath Width	30.6 km at off nadir 21.5
Range Resolution	30.2 m (ground range)
Azimuth Resolution	20 m (4 look)
Noise Equivalent Sigma-Zero (NESZ)	better than -30 dB

**Table 3.1: System parameters of ALOS polarimetric mode.**

In this research, ALOS full polarimetric SAR data (Level 1.1 Quad Polarimetric Mode), acquired in May 2007 with slant range resolution 9.5m and azimuth resolution 4.5m, are used (Sato et al., 2007). The original data have dimensions of 1248x18432 pixels, Figure 3.1a. The study area center coordinates are:  $3^{\circ} 49' 34''$  W,  $51^{\circ} 22' 56''$  N, which is located in the southern United Kingdom as shown in Figure 3.1c. In Figure 3.1b, an AVNIR-2 RGB optical image (acquired in June 2006 with 10m resolution) of the study area is presented. Based on an investigation of both the available map of the study area and the optical image, the selected study area is characterized by different land cover types, such as agricultural fields and croplands, two forest types (continuous and deciduous forests), urban areas, natural grassland and ocean. Unfortunately, a legend for the map of the study area is not available. However, the main land cover types of the area can be easily understood by comparing the map with the optical image.



(a)



(b)



(c)

**Figure 3.1:** a) RGB of the ALOS polarimetric SAR data (red =  $T_{22}$ , green =  $T_{33}$ , blue =  $T_{11}$ ), b) AVNIR-2 RGB optical image of the study area (the study area is 83km N-S and 12km W-E), c) A map of the study area.

### 3.2 RADARSAT-2 Full Polarimetric SAR Data

RADARSAT-2 is an Earth observation satellite that was launched in December 2007. It is a Synthetic Aperture Radar (SAR) that acquires data at horizontal (HH), Vertical (VV) and cross (HV and VH) polarizations over a range of resolutions from 100 to 3 meters and operates at C-band (wavelength: 3.8-7.5 cm, frequency: 8.000-4.000 MHz). Thus, three polarimetric modes are offered by this satellite: selectable linear polarization, selectable dual polarization and quad polarimetric. One of the particular characteristics of RADARSAT-2 is the capability of right- and left-looking. Table 3.2 summarizes the system parameters of the quad-polarized mode (MDA, 2006).



System Parameters	Values
Incident Angle	20 – 49 degree
Swath Width	25 km
Range Resolution	11 m
Azimuth Resolution	9 m
Noise Equivalent Sigma-Zero (NESZ)	better than -30 dB

**Table 3.2: System parameters of the quad-polarized mode of RADARSAT-2.**

RADARSAT-2 full polarimetric SAR data (Fine Quad Polarization) are also included in our research. Specifically, six images of the Churchill area in Manitoba are available. The town of Churchill is located on the shore of Hudson Bay. The climate of Hudson Bay is anomalously cold in comparison with other regions at similar latitudes because of the presence of a seasonally varying ice cover. However, the melting season became longer in the last few years and led to significant changes in the sea ice dynamics with associated changes in the ecosystem, including polar bear migration and permafrost. The RADARSAT-2 data were acquired between October 2009 and July 2010, see Figure 3.2. A SPOT image (Figure 3.3a), acquired in the 3<sup>rd</sup> of September 2006 with a ground resolution of 20 meters, is also available. Additional map of the area, indicating the different land cover types, can be seen in Figure 3.3b.

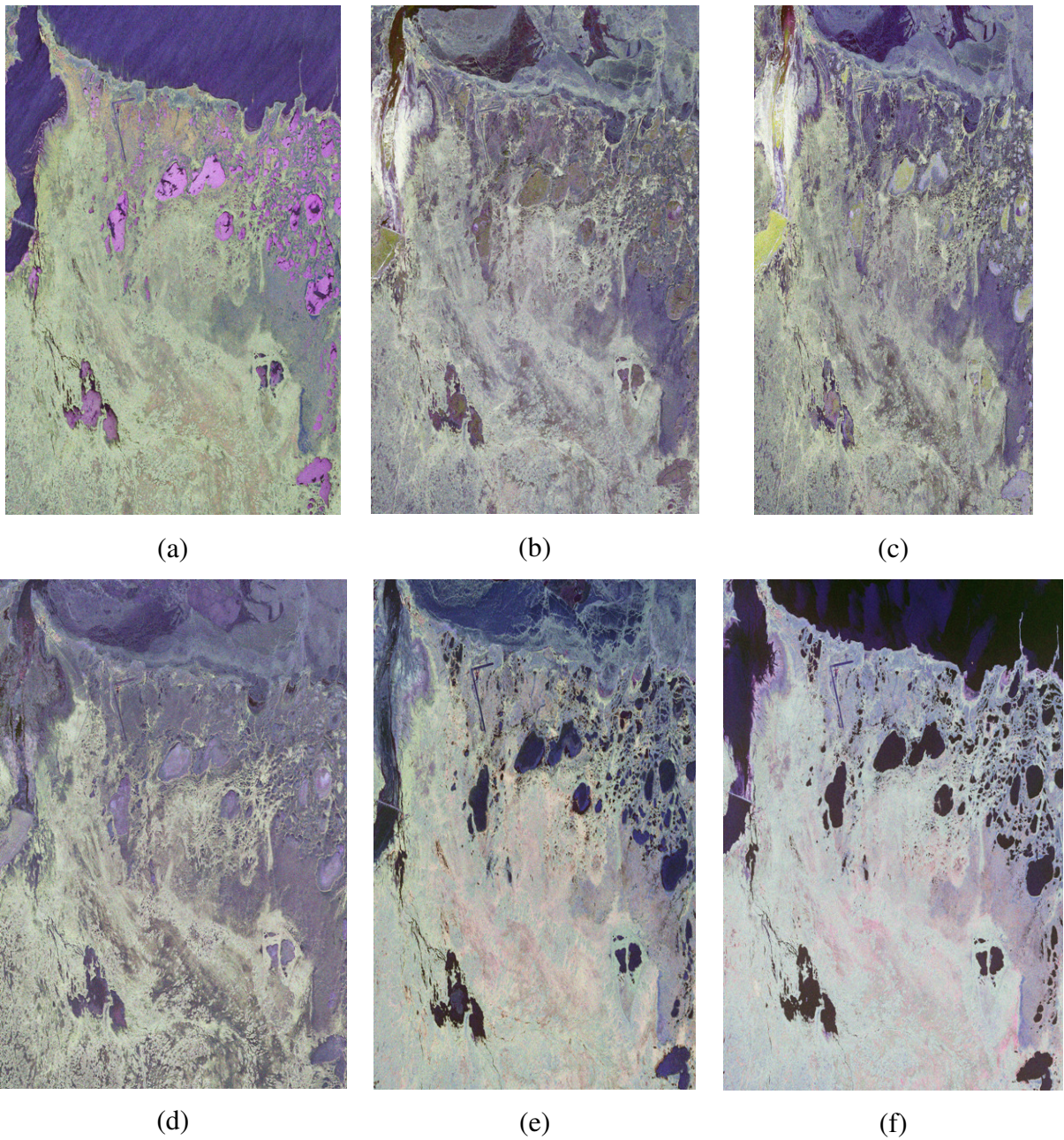
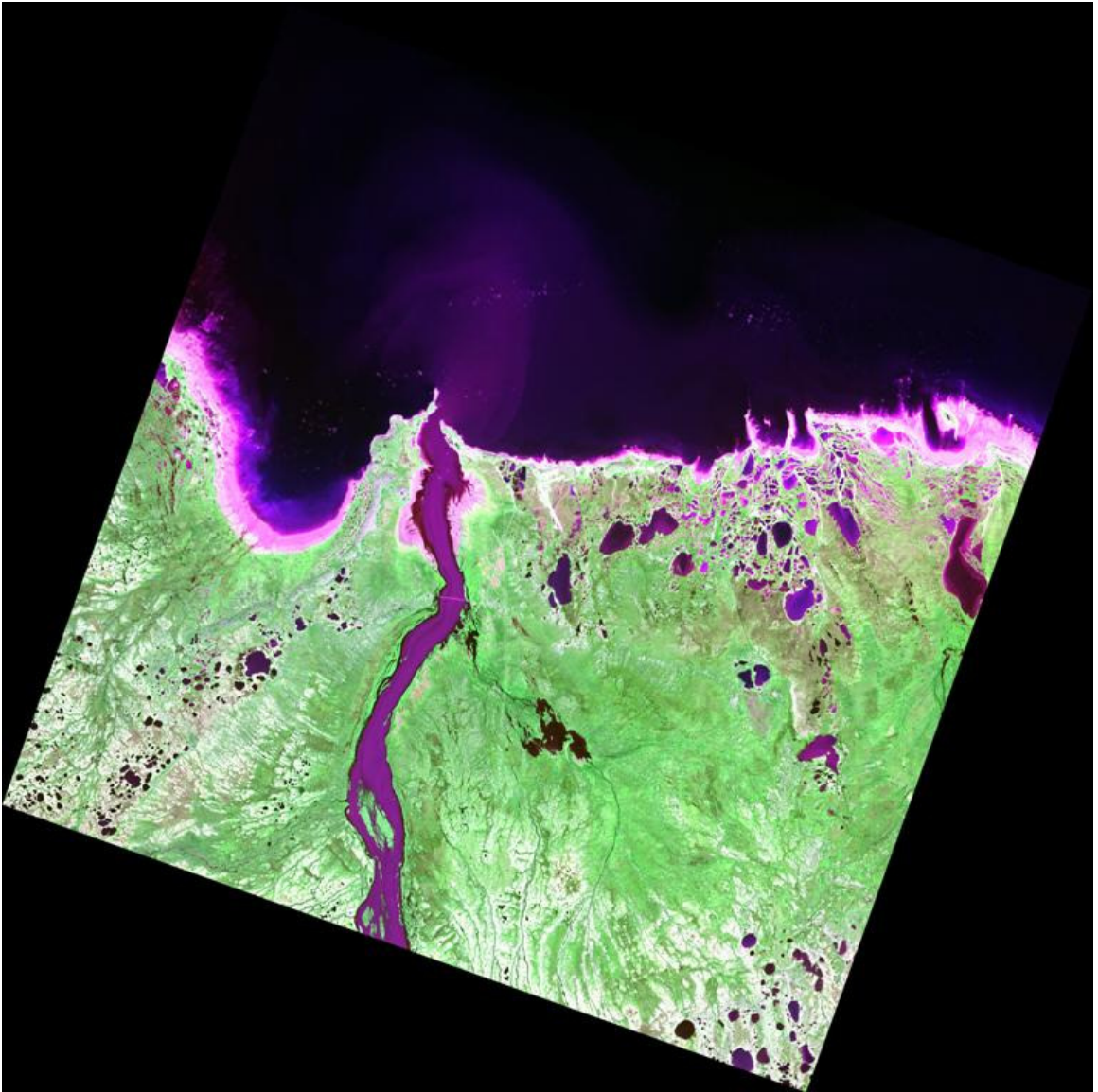
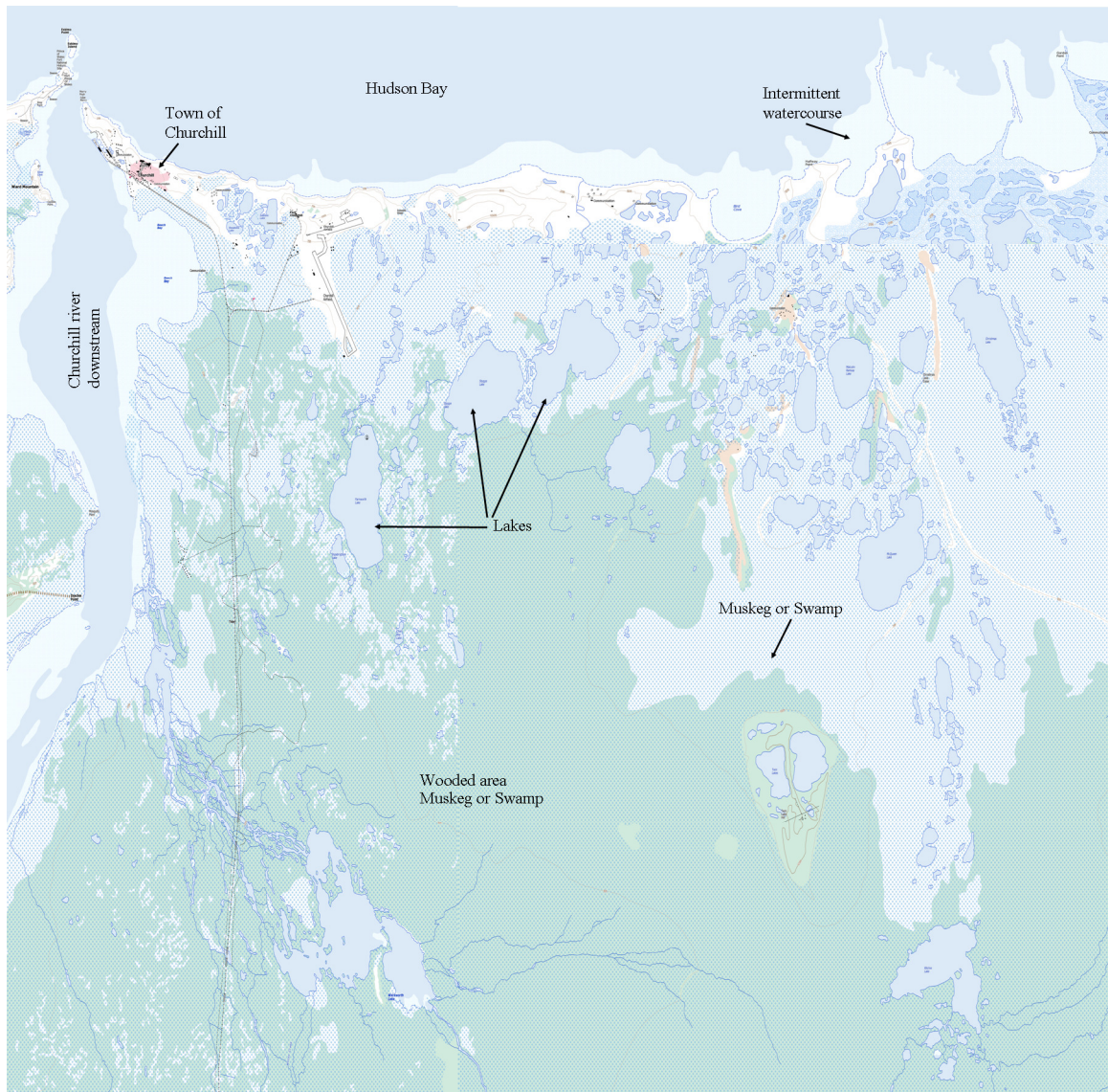


**Figure 3.2: Full polarimetric RADARSAT-2 data of Churchill acquired in: a) October 31, 2009, b) December 18, 2009, c) January 24, 2010, d) April 3, 2010, e) May 21, 2010, and f) July 22, 2010.**



(a)



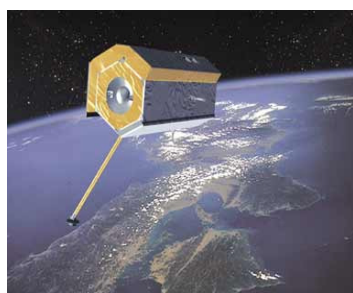
(b)

**Figure 3.3: a) SPOT image of the Churchill area, b) Map of Churchill.**

Investigating the available SPOT image and map of the area, different land cover types can be identified. The area is characterized by a large number of lakes of various sizes. These lakes freeze during winter. Muskeg or swamps also exist in forested (boreal forest) and non-forested (tundra) areas. The Churchill River downstream, which empties into Hudson Bay, can be seen as well. Furthermore, the area contains urban blocks, Churchill town, and an airport.

### 3.3 TerraSAR-X Dual Polarized SAR Data

The TerraSAR-X satellite was launched successfully in June 2007. It is a new generation of high resolution satellite operating with an X-band (wavelength: 2.4-3.8 cm, frequency: 12.500-8.000 MHz) and is an advanced and operational SAR satellite system for both scientific and commercial applications. TerraSAR-X uses a dual receive antenna mode (DRA) to measure the full scattering matrix. This is done by the alternating transmission H and V polarization pulses and receiving simultaneously H and V by the two receiving antennas. The small wavelength and the slant range resolution of one meter and better for stripmap and spotlight mode allows the monitoring of small man-made structures. Right now, only dual polarized SAR data are available. The full polarimetric mode is still in an experimental stage. Table 3.3 summarizes the system parameters of the polarimetric mode (Hajnsek and Eineder, 2005).



System Parameters	Values
Incident Angle	20° – 45°
Swath Width	15 km
Slant Range Resolution	1.9 m
Ground Range Resolution	1 look 7 m and 6 look 15 m
Noise Equivalent Sigma-Zero (NESZ)	better than -16 dB

**Table 3.3: System parameters of TerraSAR-X polarimetric mode.**

In our research, dual co-polarized SAR data (HH and VV) are also included, Figure 3.4a and b. The data consist of single look slant range complex (SSC) with a ground range resolution of 2.2m and an azimuth resolution of 6m (strip-map mode), acquired in November 2007. The study area (701x701 pixels) is located in the southwest of the United Kingdom (centre coordinates: 50° 46' 23.8" N and 3° 48' 0.4" W), very close to the area where the ALOS data were acquired. This study area mostly exhibits various agricultural fields. Trees are used as fences, surrounding the agricultural fields. Man-made objects, such as roads and buildings, exist as well. Figure 3.4c shows an optical image of the study area.

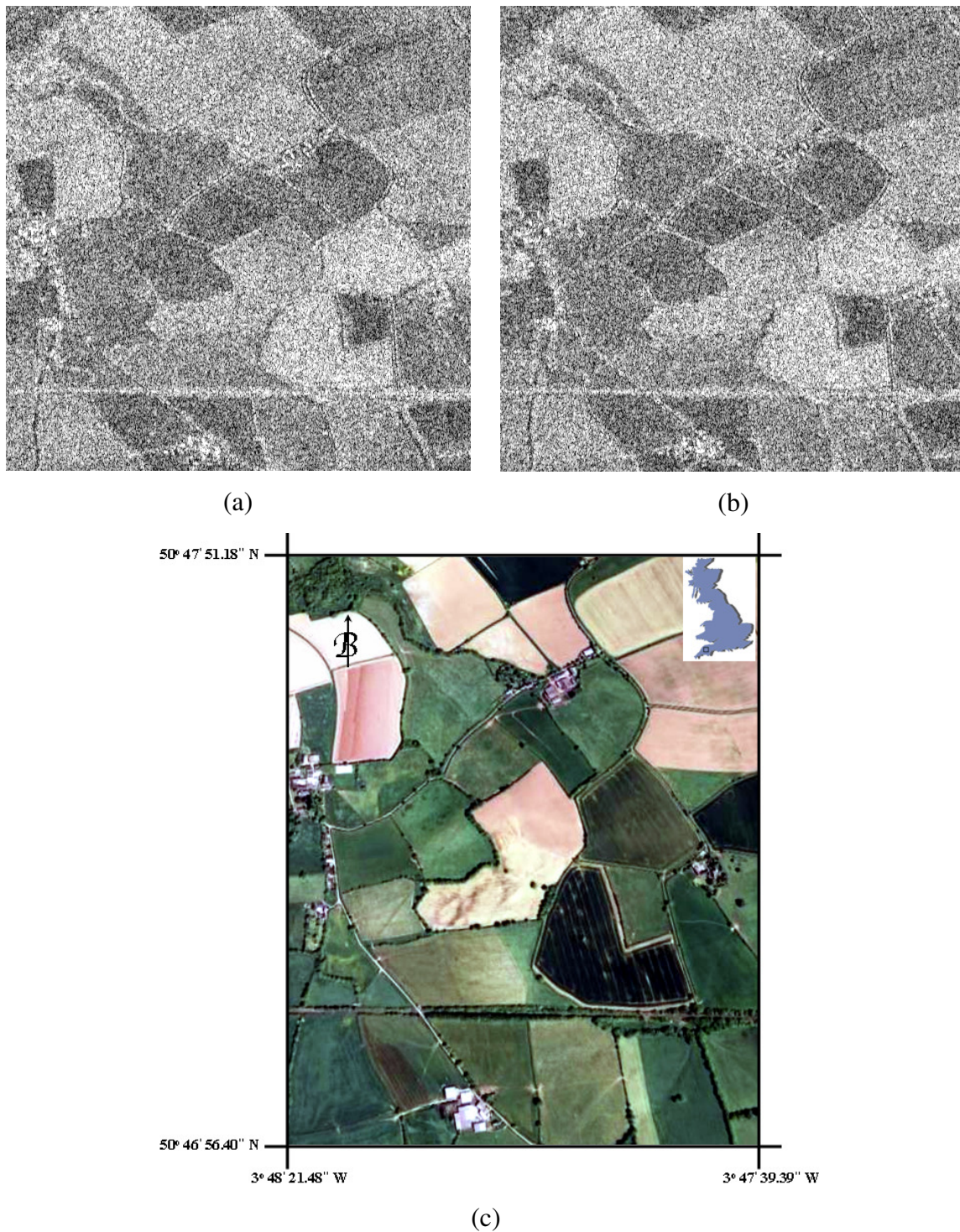


**Figure 3.4:** a) The TerraSAR-X HH image before speckle filtering, b) The VV image in the same area, c) Optical image of the study area (Source: Google Earth aerial image 31 May 2006).

## Chapter Four: Polarimetric SAR Divisive Clustering

In this chapter, two segmentation methodologies for polarimetric SAR data using the divisive clustering technique are discussed. The first one is for full polarimetric SAR data while the second is for dual polarized SAR data. Segmentation results of the full polarimetric SAR data are compared with the results obtained based on the k-means complex Wishart algorithm. For the dual polarized SAR data, segmentation results are compared with the resulting segments by the segmentation algorithm of the eCognition software package.

### 4.1 Introduction

The purpose of this chapter is to present two multilevel divisive segmentation methodologies for full and dual polarized SAR data. Both methodologies are nonparametric in the sense of overcoming the need for the a priori assumption about the underlying density function of the data, which is not always valid (Beaulieu and Touzi, 2004).

In the case of full polarimetric SAR data, segmentation is performed using the analysis images of polarimetric decomposition methods, such as Pauli (Cloude and Pottier, 1996) and Freeman-Durden (Freeman and Durdan, 1998), as input data. The proposed methodology (Dabboor et al., 2010a) goes beyond the previously discussed studies by segmenting the input data based on: 1) the hierarchicalization of the scattering mechanisms and 2) the thresholding of the amplitude histograms of the dominant scattering mechanisms using a nonparametric histogram thresholding algorithm. Thus, homogeneous segments with regard to the amplitude of the dominant scattering mechanism, in which the scattering information is preserved, are produced. Consequently, the proposed methodology is adaptable to the cases where the assumption of a single statistical distribution, complex Wishart distribution when spatial texture is absent and k-distribution when spatial texture exists (Beaulieu and Touzi, 2004), is not enough. In other words, the proposed segmentation methodology is applicable when both

textured and/or non-textured regions are contained in a study area. Furthermore, the pixels which constitute the resulting segments, in contrast to the resulting segments of the traditional segmentation methodologies, have the same dominant and second most significant scattering mechanisms.

In the case of dual polarized SAR data, the proposed methodology (Dabboor et al., 2010b) entails the thresholding of the histograms of the two SAR channels using the nonparametric histogram thresholding algorithm. Consequently, assumptions about the underlying statistical distribution are not needed in this methodology. This methodology combines the thresholded histograms of the two SAR channels in a two dimensional histogram-based space, and produces subspaces responsible for the data segmentation.

The two developed methodologies have in common:

- The use of a nonparametric histogram thresholding algorithm.
- Both involve the multi-levelling/multi-scaling concept. The user has the advantage of choosing the desired segmentation scale and selecting specific segments for further segmentation as opposed to continue segmentation on a global scale.

Before discussing the two segmentation methodologies, the used nonparametric histogram thresholding algorithm is presented in the following section.

#### **4.2 Delon's Histogram Thresholding Algorithm**

Histograms have been extensively used in image analysis, and more generally in data analysis, mainly for two reasons (Delon et al., 2007): 1) they provide a compact representation of large amounts of data, and 2) it is often possible to infer global properties of the data from the behaviour of their histogram. In image processing, many approaches have been proposed for image segmentation (e.g., Haralick and Shapiro, 1985; Pal and Pal, 1993). Among the proposed approaches are those based on histogram thresholding. A proper segmentation of the image can be achieved by finding the

appropriate thresholds or intervals that separate the modes in the histogram (Figure 4.1), which is not a simple task. This is because a miscalculation of the appropriate thresholds or intervals leads to an over- or under-segmentation of the image.

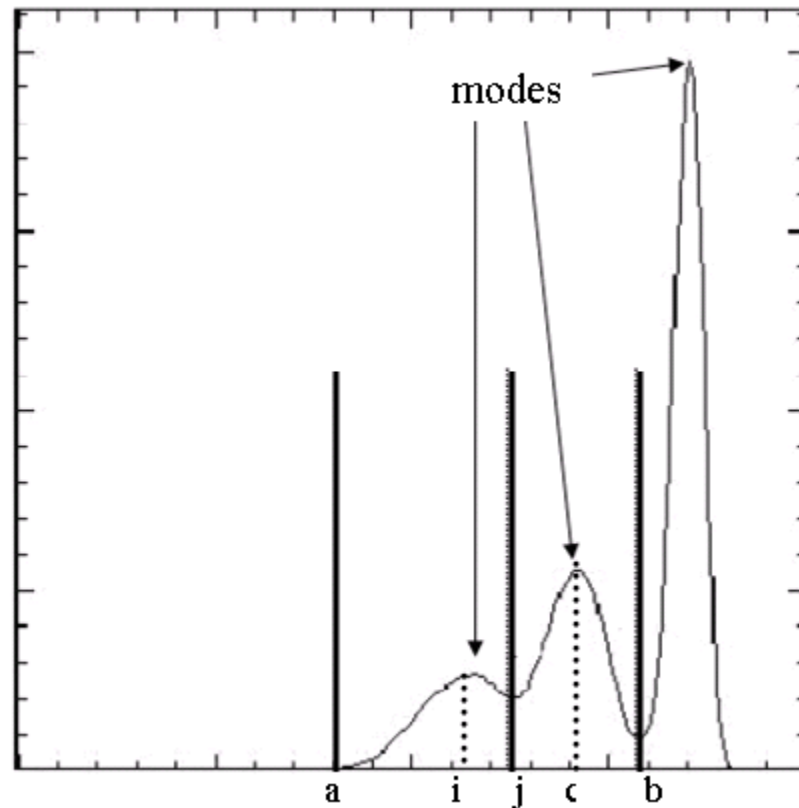


**Figure 4.1: Three-mode scheme divided into three intervals.**

Image segmentation algorithms based on histogram thresholding are distinguished into parametric and nonparametric. Among the algorithms proposed for 1D histograms are the parametric algorithms, which assume the set of data as samples of mixtures of  $k$  random variables of a given distribution, as in the Gaussian mixture models; see Duda et al. (2000). In the parametric algorithms, a statistical distribution should be assumed for the data. However, a statistical distribution might not be enough to accurately describe the data content. For example, an image that contains textured and non-textured areas cannot be described by a single statistical distribution (Beaulieu and Touzi, 2004).

Nonparametric algorithms which give up any assumption on the underlying data density, such as bi-level and multilevel thresholding methods, are presented in Cheng and Sun (2000). The nonparametric algorithms usually require the number of modes to be predefined for histogram thresholding. The selection of this parameter is crucial since an incorrect choice leads to an over- or under-segmentation of the data. In case that this parameter is not required, too many modes in the histograms are detected. Delon et al. (2007) developed a nonparametric histogram thresholding algorithm which overcomes all of the above mentioned disadvantages. This algorithm can automatically determine the number of modes in a histogram to be thresholded.

A histogram  $h$  is considered to be unimodal on an interval  $[a, b]$  if there is a point  $c \in [a, b]$  such that  $h$  follows the increasing hypothesis on  $[a, c]$  (histogram has positive slope from  $a$  to  $c$ ) and the decreasing hypothesis on  $[c, b]$  (histogram has negative slope from  $c$  to  $b$ ). The algorithm starts by finding all local minima of the histogram plus the endpoints, producing the finest possible thresholding  $S = [s_1, \dots, s_n]$  where  $s_1 = 1$  and  $s_n = L$  (the number of bins). The pair of intervals on both sides of  $s_i$  can be merged into a single interval  $[s_{i-1}, s_{i+1}]$  if the histogram in this interval follows the unimodal hypothesis. A discrete histogram  $h = (h_i)_{i=1 \dots L}$ , with  $N$  samples in  $L$  bins, follows the increasing (or decreasing) hypothesis in an interval  $[a, c]$  (or  $[c, b]$  for the decreasing hypothesis) if:

$$\frac{L(L+1)}{2} B(N, Nr(a, c), p(a, c)) \geq 0.5, \text{ for } r(a, c) \geq p(a, c) \quad (4-1)$$

or

$$\frac{L(L+1)}{2} B(N, N(1-r(a, c)), 1-p(a, c)) \geq 0.5, \text{ for } r(a, c) < p(a, c)$$

Herein,  $r(a, c)$  is the proportion of points in  $[a, c]$  and  $p(a, c)$  is the probability for a point to fall into the interval  $[a, c]$ .  $B(N, Nr(a, c), p(a, c))$  is a binomial tail:

$$B(n, k, p) = \sum_{j=k}^n \binom{n}{j} p^j (1-p)^{n-j}. \quad (4-2)$$

The probability  $p$  can be estimated from  $r$  based on the Pool Adjacent Violators algorithm, using the Grenander estimator (Grenander, 1981). Assuming an interval  $[a, c]$  in which the increasing hypothesis is to be tested (Figure 4.1), and considering a sub-interval  $[i, j]$  in  $[a, c]$ , in which  $r_i \geq r_{i+1} \geq \dots \geq r_j$ , the Grenander increasing hypothesis of  $[a, c]$  is calculated as follows:

$$D(r)_k = p = \begin{cases} \frac{r_i + \dots + r_j}{j - i + 1}, & \text{for } k \in [i, j] \\ r_k, & \text{for } k \in [a, b] \text{ and } k \notin [i, j] \end{cases} \quad (4-3)$$

where  $r_k = h_k / N$  and  $h_k$  is the number of samples that fall in the bin  $k$ . The Grenander operator  $D$  replaces each decreasing part of the interval  $[a, c]$  by a constant value equal to the mean value of the interval  $[i, j]$ . The same approach is applied to test the decreasing hypothesis of the interval  $[c, b]$ .

### 4.3 Divisive Hierarchical Full Polarimetric SAR Segmentation

#### 4.3.1 Methodology

A new divisive segmentation methodology for polarimetric SAR data is presented in this section. As mentioned previously, the proposed methodology goes beyond the traditional segmentation methods by exploiting: 1) the scattering information obtained from the polarimetric SAR decomposition methods, and 2) the inherent variations within the dominant scattering mechanism. Input data for segmentation are the analysis images produced by the polarimetric decomposition methods, such as the Pauli and the Freeman-Durden methods.

The first and the second segmentation levels in the proposed methodology exploit object preferences to specific scattering mechanisms, while the following additional levels are based on histogram thresholding. In the first level, the scattering mechanism space produced by the input data, i.e., the Pauli or Freeman-Durden images, is segmented

based on the dominant scattering mechanism that objects present. Three not obligatory coherent areas  $S_i$  ( $i=3$ ) are initially produced, where  $S_1$ ,  $S_2$ , and  $S_3$  are assigned to the three scattering mechanisms provided by the analysis images. In the second level, accepting that objects due to their shape complexity can show preference to more than one scattering mechanism, areas are further segmented based on the second scattering mechanism that objects present. For example, areas where the scattering mechanism  $S_1$  is dominant are further segmented into subareas where: 1) the scattering mechanism  $S_1$  is the only significant mechanism and the other two mechanisms  $S_2$  and  $S_3$  are insignificant ( $S_1S_1$ ), 2) the scattering mechanism  $S_1$  is dominant and the scattering mechanism  $S_2$  is significant ( $S_1S_2$ ), and 3) the scattering mechanism  $S_1$  is dominant and the scattering mechanism  $S_3$  is significant ( $S_1S_3$ ). A formula is experimentally established to define the significance of a scattering mechanism. An area labeled as  $S_1$  is further segmented into three subareas  $S_1S_1$ ,  $S_1S_2$  and  $S_1S_3$ , based on the following relations:

$$k \in \begin{cases} S_1S_1 & \text{if } \frac{P_1}{P_1 + P_2 + P_3} \geq C \\ S_1S_2 & \text{if } \frac{P_1}{P_1 + P_2 + P_3} < C, \text{ and } P_2 \geq P_3 \\ S_1S_3 & \text{if } \frac{P_1}{P_1 + P_2 + P_3} < C, \text{ and } P_2 < P_3, \end{cases} \quad (4-4)$$

$k$  represents a pixel which belong to the area  $S_1$ ,  $P_1$  is the normalized amplitude of the dominant scattering mechanism,  $P_2$  and  $P_3$  are the normalized amplitudes of the remaining two mechanisms.  $C$  is a threshold parameter calculated from the contribution percentage of the dominant scattering with regard to the total scattering for each area and defined as follows:

$$\frac{1}{3}(P_1^m + P_2^m + P_3^m) = C, \quad (4-5)$$

where  $P_i^m = \frac{1}{n_i} \sum_{k=1}^{n_i} \frac{P_{ik}}{P_1 + P_2 + P_3}$ ,  $i = 1, 2, 3$ .

$n_i$  is the number of pixels in the area  $S_i$  with dominant scattering mechanism  $P_i$ . The dominant scattering mechanism, as well as the second most significant scattering mechanism is considered due to the fact that they possess the major portion of the value of the total amplitude. For example, for the data set used in this research they possess approximately 82% of the total amplitude in the Pauli case and 92% of the total amplitude in the Freeman-Durden case. Thus, the third scattering mechanism can be neglected in the segmentation scheme.

Once the segmentation based on the hierarchicalization of the scattering mechanisms is accomplished, further segmentation levels are produced in order to exploit inherent variations within the dominant scattering mechanism. Thus, in the third segmentation level, each subarea of the second level is further segmented based on the histogram of the dominant scattering component. Herein, the dominant scattering mechanism is used only because it represents the largest portion of the total backscattering. For example, for the data set used in this research, the dominant scattering mechanism possesses approximately 52% of the total backscattering amplitude for the Pauli case and 62% for the Freeman-Durden case. The user can define the subareas to be further segmented or allow the execution of the algorithm for the entire image. For each subarea the procedure entails the calculation of the histogram of the dominant scattering mechanism only and its thresholding into homogeneous regions using the nonparametric histogram thresholding algorithm proposed by Delon et al. (2007). Segments provided by the third segmentation level serve as input for a following level which exploits more inherent variations within the dominant scattering mechanism. The segmentation procedure terminates when the desired segmentation scale is achieved. A flowchart of the proposed segmentation methodology limited to three segmentation levels is shown in Figure 4.2.

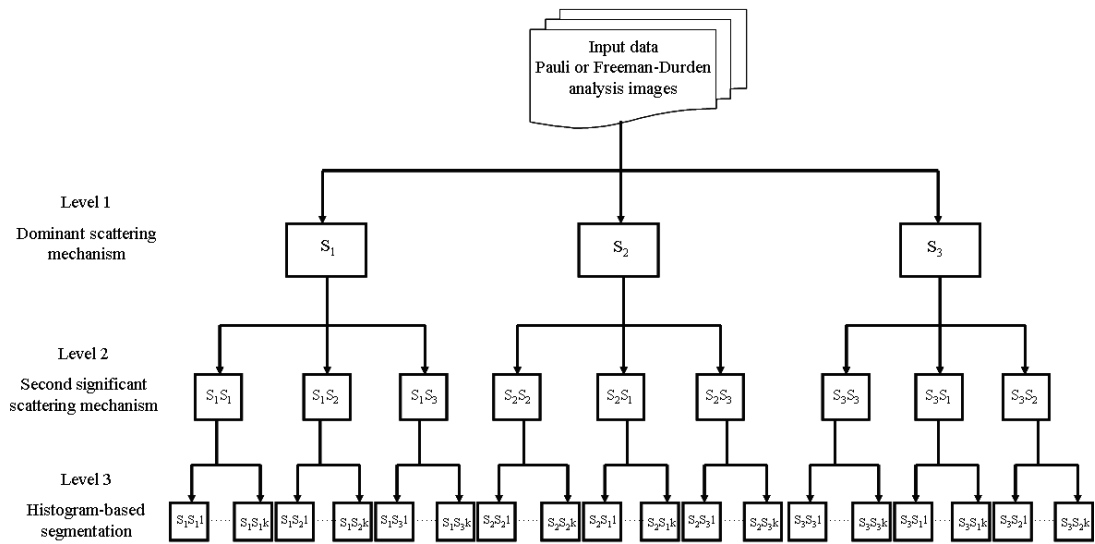


**Figure 4.2: Flowchart of the proposed multilevel segmentation methodology based on input data from Pauli or Freeman-Durden analysis.**

The proposed methodology can produce many levels depending on the desired segmentation scale. Hence it can be adapted to user needs and existing knowledge about the targets. Only three segmentation levels are presented and discussed herein, however, the method is not limited to three levels. Criteria, such as the number of pixels within a segment or the standard deviation of the amplitude value of dominant scattering mechanism of pixels in the segment, can be used to select segments for further segmentation. The amplitude histograms of the selected segments can be calculated and thresholded using the nonparametric histogram thresholding algorithm.

### 4.3.2 Implementation

#### 4.3.2.1 Pre-processing

The proposed segmentation methodology is applied to the available ALOS PALSAR polarimetric SAR data. An area of 333x329 pixels is selected with centre coordinates: 51° 12' 17.77" N and 3° 28' 39.81" W. Various land cover categories exist in

the selected area, e.g., forest, cropland, urban area (town of Minehead), and sea (Bristol Channel), each one including subcategories, e.g., the settlements include urban and suburban areas. Categories and subcategory presents a different microwave scattering behavior, resulting in a specific color in the RGB polarimetric images, Figure 4.4a.

Before segmentation, speckle reduction is a required step for the elimination of noise and smoothing of the SAR images. Lee's speckle filter which uses a multiplicative noise model, refined Lee filter (Lee et al., 1999b), and additive noise model (normal distribution with mean zero and standard deviation  $\sigma$ ) was applied (Lee et al., 1991), and the Equivalent Number of Looks (ENL) (Anfinsen et al., 2008) were calculated in order to find the most appropriate filter and performance. Better noise despeckling was obtained using the multiplicative-noise-model Lee filter (mean ENL is 8, instead of 4 for the additive noise model). Thus, the Lee speckle filter with the multiplicative noise model is used in this study. Lee et al. (2001) has shown that the application of the refined Lee filter three times on simulated SAR data can better distinguish the different surface types (Figure 4.3).

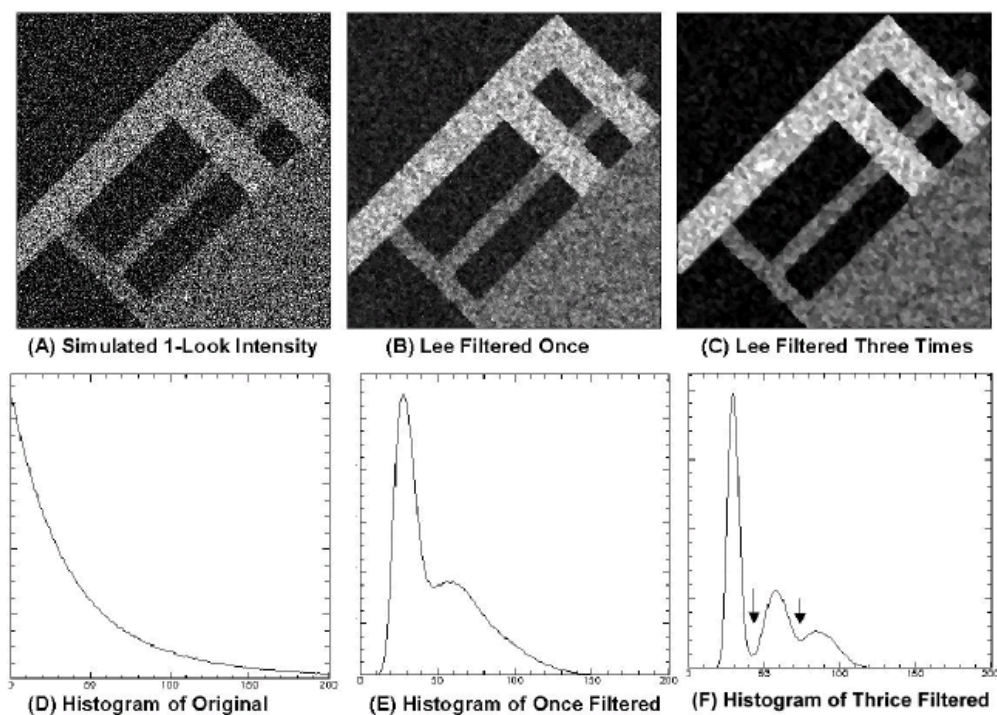


**Figure 4.3: Image segmentation by speckle filtering using the refined Lee filter.**

As a better discrimination between different surface types can be achieved by applying a Lee filter three times (Lee et al. (2001); Du et al. (2002)), the filter was applied three times. Figure 4.4b shows the results of applying a Lee filter with a window size of 7x7 pixels to the polarimetric SAR data. This window size favors speckle reduction without producing over-smoothing, (Du et al., 2002; Park and Moon, 2007; Gao and Ban, 2008). Experiments with larger and smaller window sizes did not give the desired results.

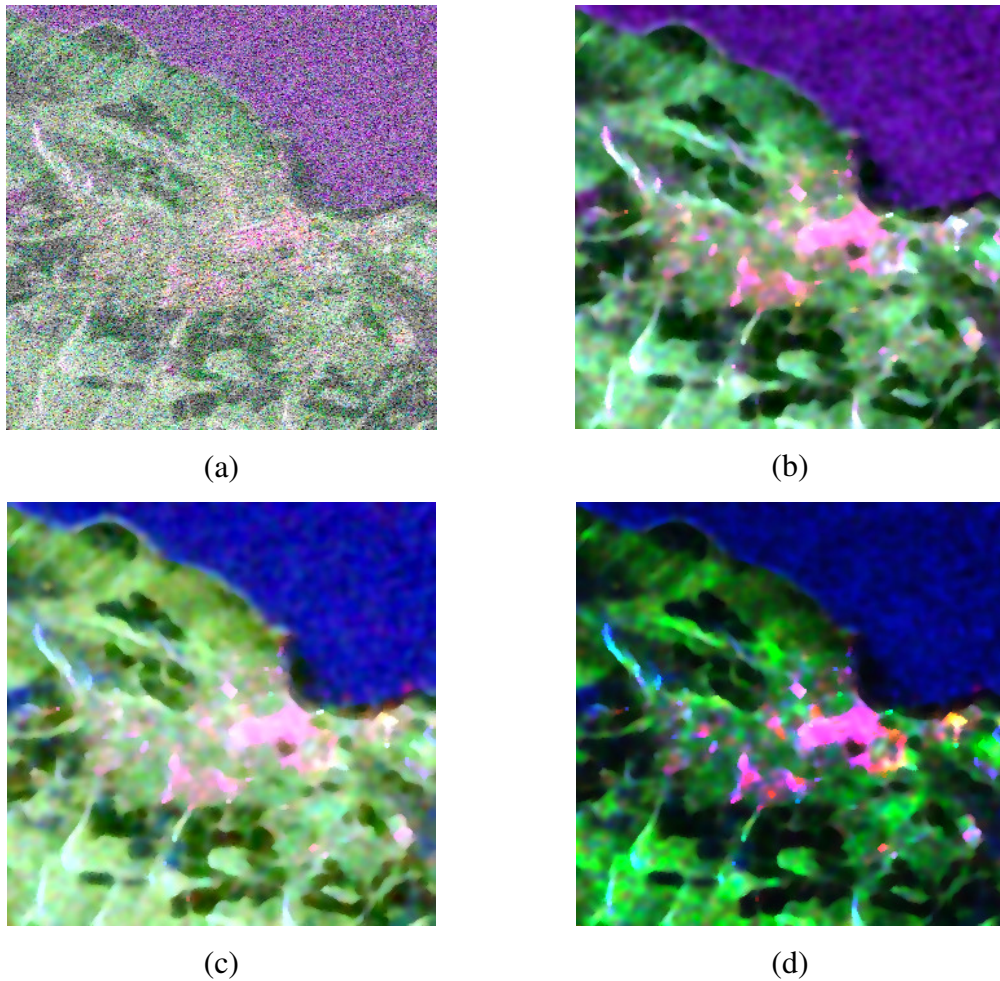
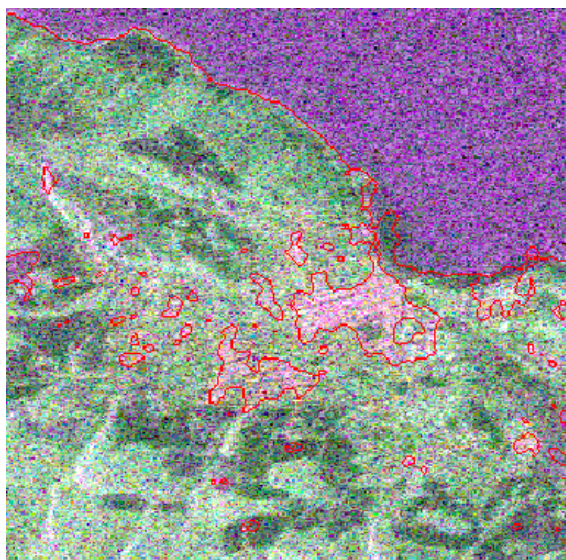


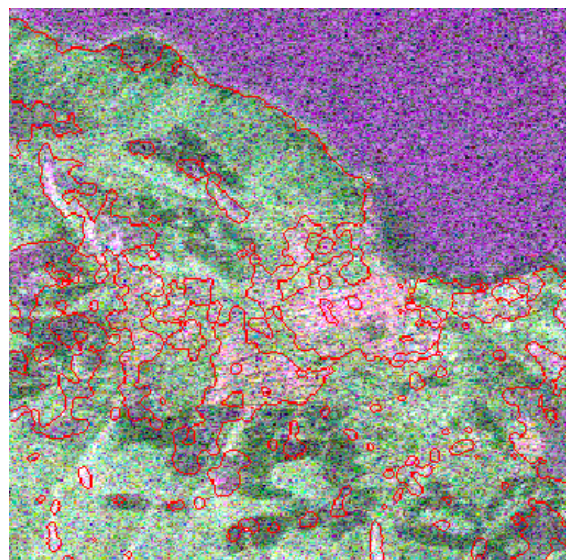
**Figure 4.4:** a) Polarimetric SAR image: Red = HH, Green = HV, Blue = VV, b) Data after removing speckle noise using the refined Lee filter three times, c) Pauli analysis images in RGB (Red = double bounce, Green = 45° tilted double bounce, Blue = surface), d) Freeman-Durden analysis images in RGB (Red = double bounce, Green = volume, Blue = surface).

#### 4.3.2.2 First Segmentation Level

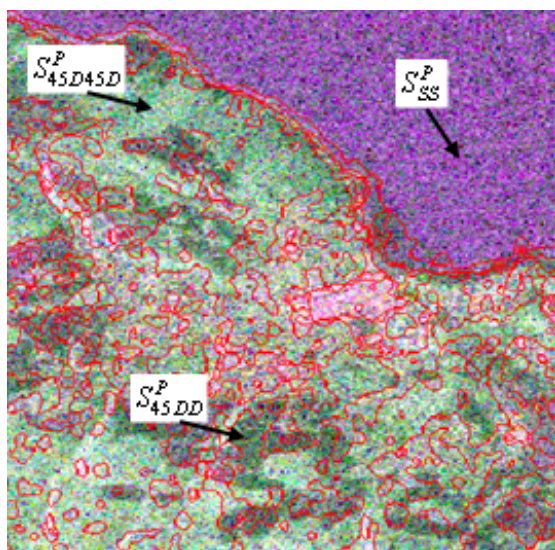
The Pauli analysis images and the Freeman-Durden analysis images are calculated from the polarimetric SAR image (Figures 4.4c and d). Each decomposition set of images is separately used as input data in the segmentation process. Using the Pauli analysis images, data are segmented based on the dominant scattering mechanism into: a) areas where the surface scattering mechanism is dominant ( $S_S^P$ ), b) areas where the double bounce scattering mechanism is dominant ( $S_D^P$ ), and c) areas where the 45° tilted double bounce scattering mechanism is dominant ( $S_{45D}^P$ ). On the other hand, using the Freeman-Durden analysis images, data are segmented based on the dominant scattering mechanism into: a) areas where the surface scattering mechanism is dominant ( $S_S^{FD}$ ), b) areas where the double bounce scattering mechanism is dominant ( $S_D^{FD}$ ), c) areas where the volume scattering mechanism is dominant ( $S_V^{FD}$ ). The first segmentation level results for the Pauli analysis images and the Freeman-Durden analysis images are shown in Figures 4.5a and b, respectively. Comparing the produced segments with the available optical image of the study area (Figure 3.1b) allows for the identification of correlations between land cover type and scattering mechanism: 1) For the case of Pauli analysis image (Figure 4.5a), urban areas (pink color) appear to exhibit double bounce scattering mechanism, sea (blue) appears to exhibit surface scattering mechanism, and forest and cropland (green and black areas) show 45° tilted double bounce scattering. 2) For the case of Freeman-Durden image (Figure 4.5b), sea, urban and suburban areas exhibit the surface scattering mechanism as the dominant one. Only a few segments in the urban area show double bounce scattering. Cropland and forest (dark areas surrounded by green areas) exhibit the volume scattering mechanism.



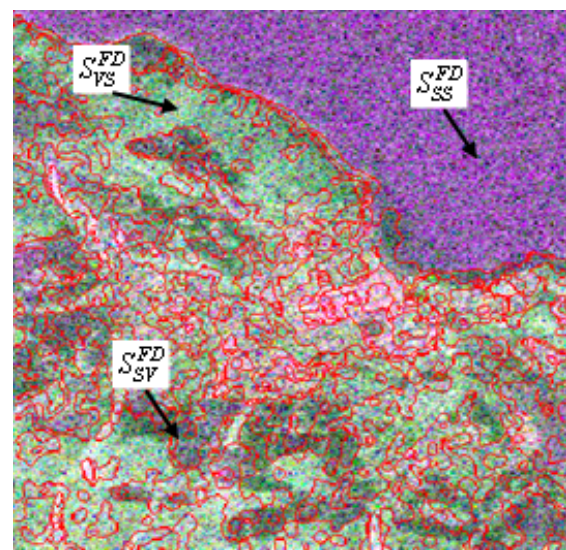
(a)



(b)



(c)



(d)

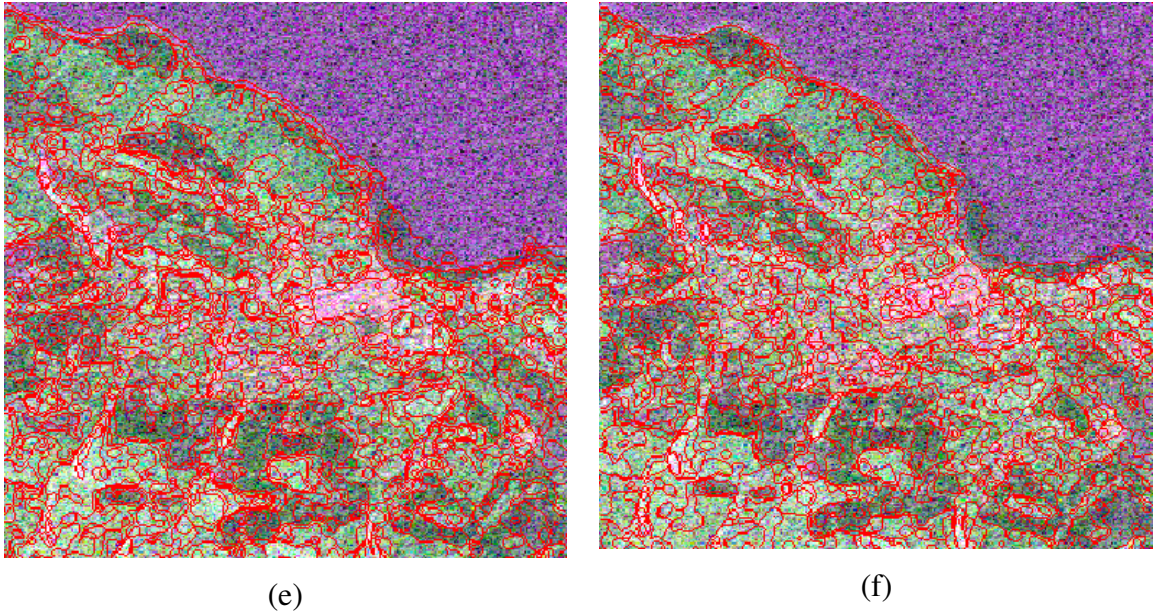


**Figure 4.5: a) First segmentation level of Pauli data, b) First segmentation level of Freeman-Durden data, c) Second segmentation level of Pauli data, d) Second segmentation level of Freeman-Durden data, e) Third segmentation level of Pauli data, f) Third segmentation level of Freeman-Durden data.**

#### 4.3.2.3 Second Segmentation Level

Further segmentation can be obtained through a second segmentation level. In this level, except for the dominant scattering mechanism that appears in each area, the scattering mechanism with the second most significant value is taken into consideration. In this study, the value of the thresholding parameter  $C$  in (4-4) was found to be equal to 0.51 and 0.61 for the case of Pauli and Freeman-Durden images, respectively. Thus, in the case of Pauli data, areas which are labeled as surface scattering are further segmented into: a) subareas where surface scattering is dominant and the remaining scattering mechanisms (double bounce and  $45^\circ$  tilted double bounce) are insignificant ( $S_{SS}^P$ ), b) subareas where the surface mechanism is dominant and the double bounce mechanism is significant ( $S_{SD}^P$ ), and c) subareas where the surface mechanism is dominant and the  $45^\circ$  tilted double bounce mechanism is significant ( $S_{S45D}^P$ ). Areas in which double bounce scattering or  $45^\circ$  tilted double bounce scattering is dominant are divided in an analog

fashion. In the case of Freeman-Durden data, areas which are labeled as surface scattering are further segmented into: a) subareas where surface scattering is dominant and the remaining scattering mechanisms (double bounce and volume) are insignificant ( $S_{SS}^{FD}$ ), b) subareas where surface scattering is dominant and the double bounce mechanism is significant ( $S_{SD}^{FD}$ ), and c) subareas where surface scattering is dominant and the volume mechanism is significant ( $S_{SV}^{FD}$ ). Areas in which double bounce scattering or volume scattering is dominant are divided in an analog way.

The results of the second segmentation level are shown in Figures 4.5c and d. It is obvious that more detailed segmentation was obtained for both Pauli and Freeman-Durden images. Significant improvements can be seen in the Freeman-Durden decomposition image. Sea, urban and sub-urban areas (blue and pink areas) are clearly separated. However, since the second segmentation level is based on the scattering hierarchicalization only, variations of the amplitude values of scattering mechanisms even if these are considerably high are not considered yet. Thus, some segments do not fit to the RGB composite color variations. This issue will be faced in a third segmentation level.

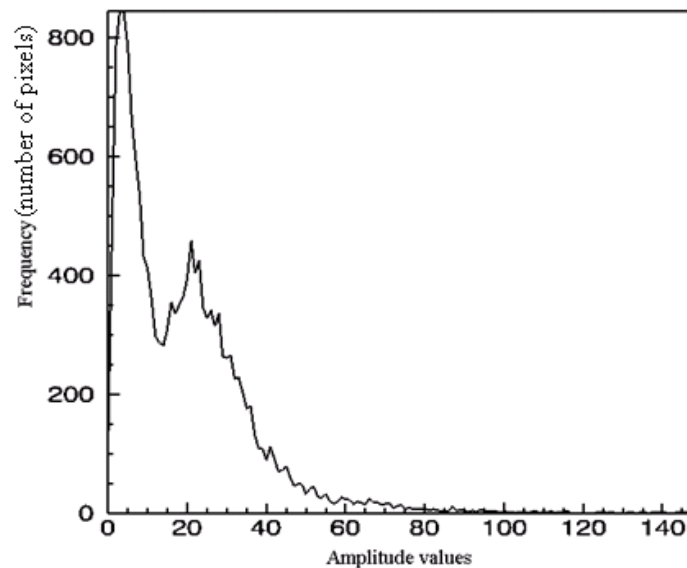


**Figure 4.6: Variations of the amplitude values of the Surface scattering mechanism (dominant) for the subarea  $S_{SV}^{FD}$  of the Freeman-Durden images.**

Figure 4.6 presents an example of the variation in amplitudes of the scattering mechanisms. Herein, the variations of the amplitude values of the surface scattering mechanism (dominant) in the subarea  $S_{SV}^{FD}$  of the Freeman-Durden are plotted.

#### 4.3.2.4 Third Segmentation Level

Further segmentation of the subareas is performed by computing and thresholding the amplitude histogram of the dominant scattering mechanism ( $P_1$ ) using the nonparametric histogram thresholding algorithm. Each histogram is divided into homogeneous regions. Thus, the histogram of each subarea, i.e.,  $S_1S_2$ , where  $S_1$  is the dominant scattering mechanism and  $S_2$  is the second most significant mechanism, is thresholded into homogeneous regions  $S_1S_21 \dots S_1S_2k$ , where  $k$  is the number of regions which result from the division of the histogram of the dominant scattering mechanism (Figure 4.2).

The histogram thresholding algorithm can be applied on all resulting subareas or selected ones. A simple criterion, such as the number of pixels in a subarea, can be used in order to select subareas for further segmentation. In our case study, subareas with a number of pixels higher than 10% of the total number of pixels in the image were selected for further segmentation. In the Pauli case, the nonparametric histogram thresholding algorithm was implemented for the subareas  $S_{SS}^P$ ,  $S_{45D45D}^P$  and  $S_{45DD}^P$ , which are characterized as large subareas in the second segmentation level. In the Freeman-Durden case, the histogram segmentation algorithm was implemented for the subareas  $S_{SS}^{FD}$ ,  $S_{SV}^{FD}$  and  $S_{VS}^{FD}$ , which are characterized as large subareas in the second segmentation level. Figures 4.5e and f show the results of the third segmentation level for Pauli and Freeman-Durden, respectively. The segments of the third level for the Pauli case correspond to a total of 17 classes; a total of 3 classes in the first level, 9 in the second and 17 in the third level, respectively. For the Freeman-Durden case, the produced segments correspond to a total of 16 classes; a total of 3 classes of the first level, 9 in the

second, and 16 in the third level, respectively. It is clear that a much more detailed segmentation has been obtained in this level, although only large subareas were selected (> 10% of total number of pixels).

In the third level (Figures 4.5e and f), segments fit effectively to the RGB colour variations. Superfluous boundaries might be noted between some regions of the study area in this level. This is not entirely true because the study area is mainly an agricultural area where trees are located along the roads and in some cases used as barriers between agricultural fields (Figure 3.1b). Thus, very thin linear segments for these areas are produced giving the impression of superfluous boundaries. In principle, all the resulting segments from the third level or part of them can be segmented even further by using a fourth segmentation level based on histograms. However, as in the study area used herein, the third segmentation level already achieves the segmentation scale which nicely fits the semantic objects in the image as shown by the coherent fit between contour lines and homogeneous colored areas, no further segmentation level was applied.

### ***4.3.3 Comparison with the k-means Algorithm***

From the first and the second segmentation levels, it is obvious that the information of the dominant and the second most significant scattering mechanisms alone is not enough for obtaining the desired segmentation results. It is possible to separate objects which correspond to the main surface types, such as ocean, urban areas, vegetation, etc. However, information related to the scattering mechanisms is preserved in the first and second segmentation levels and in the lower levels. Thus, in contrary with classical segmentation techniques, pixels of a single segment have similar scattering mechanisms. For more detailed segmentation results, the information related to the inherent variations within the dominant scattering mechanism is necessary and used in lower levels. The preserved information of the scattering mechanisms of the segments down to the lowest level can be exploited in a classification approach.

The segmentation levels of the proposed segmentation method are compared with the results produced by approaches based on the k-mean clustering algorithm. Herein, the

segmentation approach proposed in Lee et al. (1999a) is applied to the data. Initial segmentation based on the entropy (H) and alpha ( $\alpha$ ) plane is implemented and the Wishart k-means clustering algorithm is applied in order to extract the final segments, which correspond to eight initial classes. Only one refined 7x7 Lee filter is applied on the data for despeckling, as it was done in the Lee et al. (1999a) study. Figure 4.7a shows the boundaries of the produced segments superimposed over the initial data. Furthermore, the segmentation approach proposed in Cao et al. (2007) is applied on the initial data. Herein the initial data are segmented into 48 initial classes based on the span, entropy (H), alpha ( $\alpha$ ) and anisotropy (A) parameters. One refined 7x7 Lee filter was applied to the data for despeckling, as it was done in the Cao et al. (2007) study. Figure 4.7b shows the boundaries of the produced segments superimposed over the initial data.

A more detailed segmentation is produced by the Wishart k-means H/ $\alpha$  approach in comparison with the first and second segmentation levels for Pauli and Freeman-Durden. In comparison to the third-level segments, segments produced by the Wishart k-means H/ $\alpha$  and the Wishart k-means span/H/ $\alpha$ /A approaches are characterized by irregular boundaries. In our proposed method, although the segments in the third level correspond to 17 and 16 classes for Pauli and Freeman-Durden, respectively, data are not over-segmented. Over-segmentation is observed in the case of the Wishart k-means span/H/ $\alpha$ /A segmentation approach (arrows in Figure 4.7b). Table 4.1 presents the number of the produced segments for Pauli (third level), Freeman-Durden (third level), Wishart k-means H/ $\alpha$  and Wishart k-means span/H/ $\alpha$ /A.

<b>Segmentation</b>	<b>Number of segments</b>
Pauli (this study)	2641
Freeman-Durden (this study)	2336
Wishart k-means H/ $\alpha$	3164
Wishart k-means span/H/ $\alpha$ /A	8988

**Table 4.1: Number of segments for each segmentation case.**

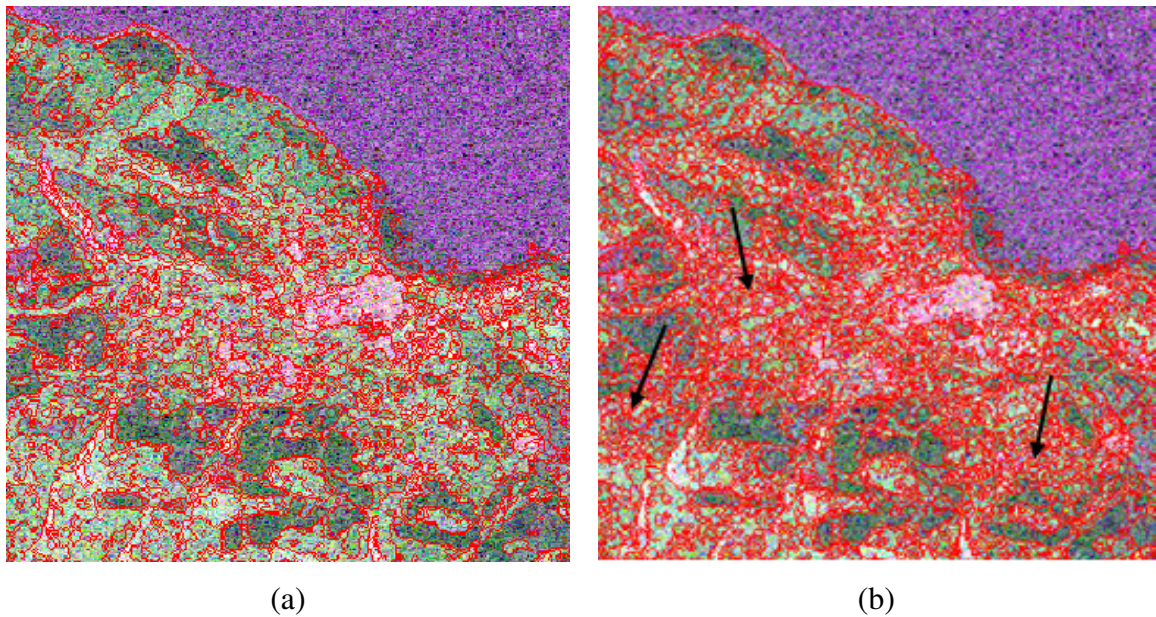


**Figure 4.7: Segmentation based on the k-mean clustering algorithm. a) Segments produced based on Wishart k-means  $H/\alpha$  clustering, b) Segments produced based on Wishart k-means SPAN/ $H/\alpha/A$  clustering.**

A zoom into a selected region at the Southern end of the study area is shown in Figure 4.8 for cases of Pauli (Figure 4.8a), Freeman-Durden case (Figure 4.8b), Wishart k-means  $H/\alpha$  (Figure 4.8c), and Wishart k-means span/ $H/\alpha/A$  (Figure 4.8d). It is clear in Figure 4.8 that segments produced by the proposed methods (Figures 4.8a and b) have smooth boundaries. Agricultural fields (dark regions) are well divided in all four cases. However, in the Pauli and Freeman-Durden cases, these dark regions present a more detailed segmentation than that produced by the Wishart k-means  $H/\alpha$  and Wishart k-means span/ $H/\alpha/A$  approaches. For the forest (green regions), regular-shape polygons satisfactorily segment the area in the Pauli and Freeman-Durden cases in contrast to the Wishart k-means  $H/\alpha$  case that creates insufficient segments and Wishart k-means span/ $H/\alpha/A$  case that over-segments the forest areas.

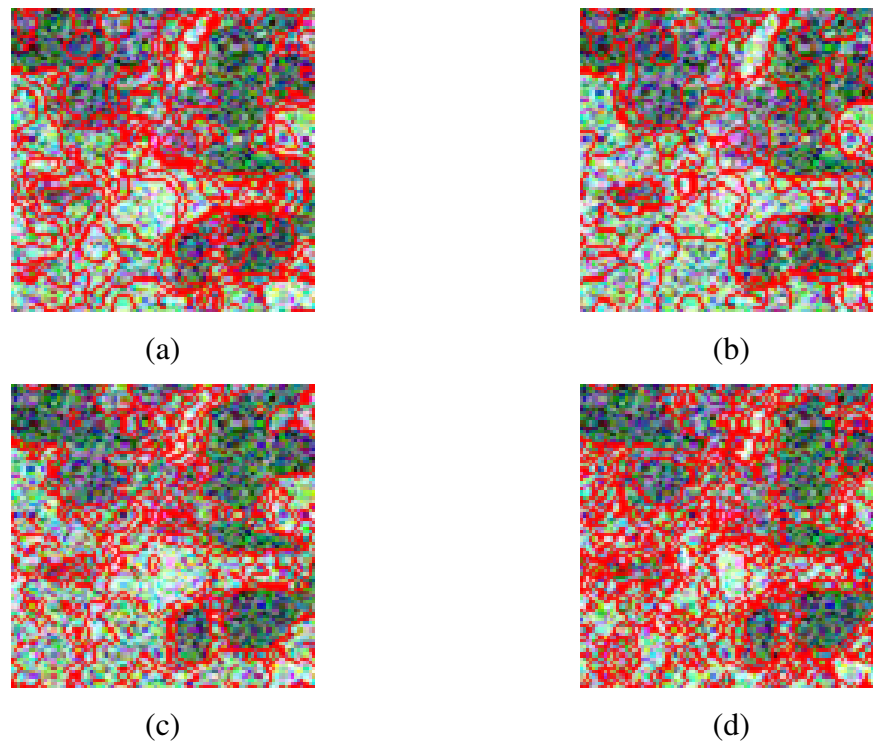


**Figure 4.8:** Sample region selected from the Southern end of the study area. a) Pauli case, b) Freeman-Durden case, c) Wishart k-means  $H/\alpha$ , d) Wishart k-means  $\text{span}/H/\alpha/A$ .

#### 4.4 Divisive Hierarchical Dual Polarimetric Segmentation

##### 4.4.1 Methodology

Dual polarized SAR data provide more information about the radar target, in comparison to the SAR data from a single channel SAR system. However, a lack of the target information still exists due to the fact that only two channels of the four are available. In this section, a new segmentation methodology is presented for dual polarized SAR data. The proposed methodology is based on: 1) the thresholding of the histograms of two SAR channels (images) using the nonparametric histogram thresholding algorithm discussed previously, 2) the combination of thresholded histograms in a two dimensional histogram-based space, where subspaces responsible for the resulting image segments are produced. The proposed methodology is multilevel where data are segmented hierarchically. Two derived criteria are established to control

the sequence to following segmentation levels. Below, the proposed methodology is discussed in detail.

An image with two channels  $c_1$  and  $c_2$  has histograms  $h_1$  and  $h_2$ , respectively. Each histogram can be thresholded into regions  $R = [r_1, \dots, r_m]$  by identifying histogram intervals, where  $m$  is the number of the resulting regions of the thresholded histogram  $h$ . The two thresholded 1D histograms can be combined in order to form a two dimensional histogram-based space, as shown in Figure 4.9. Final segmentation of the image can be obtained by dividing the two dimensional histogram-based space into subspaces, based on the resulting regions by histogram thresholding. The number of the produced subspaces is equal to  $m_1 \times m_2$ , where  $m_1$  and  $m_2$  are the numbers of resulting regions from the first and second histograms, respectively. Thus, homogeneous segments of the image can be calculated by assigning each pixel to one of the defined subspaces based of the following relation:

$$p \in s_{ij} \text{ if } \begin{cases} x_p^1 \in r_i \\ \text{and} \\ x_p^2 \in r_j \end{cases} \text{ where } i = 1, 2, \dots, m_1 \text{ and } j = 1, 2, \dots, m_2 \quad (4-6)$$

$p$  is an image pixel,  $x_p^1$  and  $x_p^2$  are the amplitude values of the pixel  $p$  in the channels  $c_1$  and  $c_2$ , respectively, and  $s_{ij}$  is a subspace of the two dimensional histogram-based space. Figure 4.9 shows the concept of the proposed segmentation methodology. The calculated histograms in the first segmentation level are for the whole channels  $c_1$  and  $c_2$ . In the next segmentation levels, the calculated histograms are for image subsets, which correspond to the subspaces that are selected to be further divided.

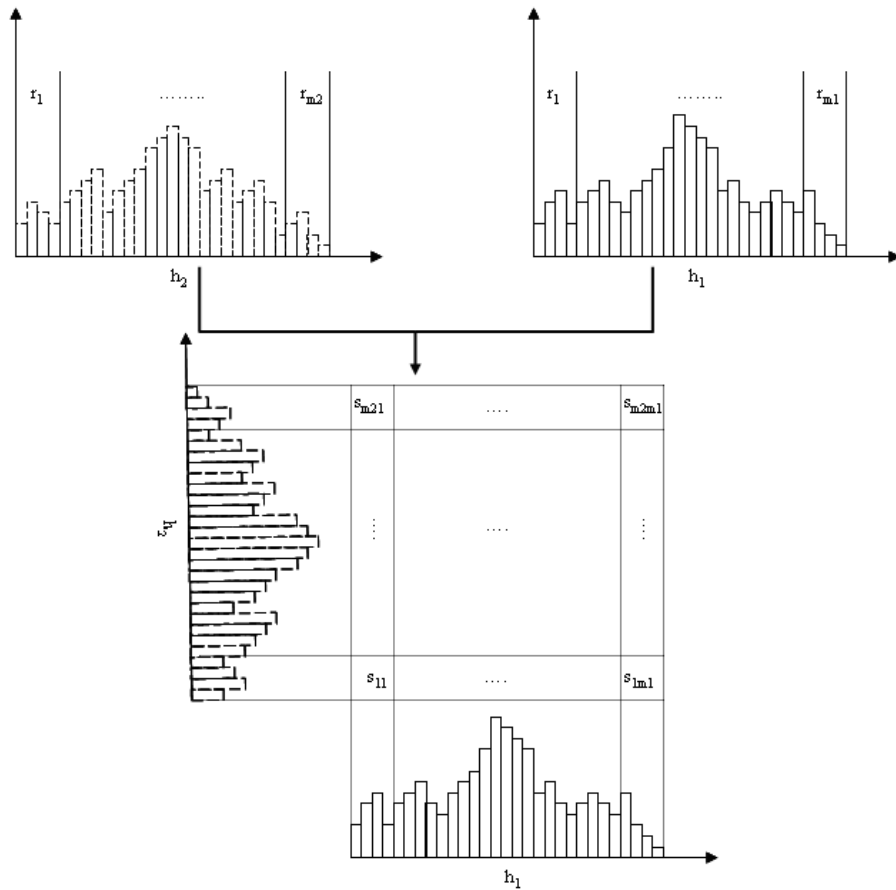


**Figure 4.9:** Scheme shows the concept of the proposed segmentation methodology that creates subspaces based on the thresholded histograms.

In order to proceed to the next level, each  $s_{ij}$  should satisfy the following criteria:

$$s_{ij} \text{ is further divided if } \begin{cases} N_{ij} > aN \\ \text{and} \\ \sigma_{ij}^1 \geq \frac{\sigma_{\mu}^1}{2} \text{ or } \sigma_{ij}^2 \geq \frac{\sigma_{\mu}^2}{2} \end{cases} \quad (4-7)$$

where  $N_{ij}$  is the number of pixels that belong to subspace  $s_{ij}$  and  $N$  is the total number of the pixels.  $\sigma_{ij}^1$  is the standard deviation of the subspace  $s_{ij}$  and  $\sigma_{\mu}^1$  is the standard deviation of the mother subspace in channel  $c_1$  while  $\sigma_{ij}^2$  and  $\sigma_{\mu}^2$  are the standard deviation of the subspace  $s_{ij}$  and the mother subspace in channel  $c_2$ . In the first criterion,  $a$

is a parameter ( $1 > a > 0$ ) that controls the number of subspaces to be tested for further division by using the second criterion. Thus, the lower the value of the parameter  $a$  the higher the number of subspaces to be tested and vice versa. In this case study, the value of  $a = 0.03$  is selected. This value of  $a$  was selected after testing different values. The second criterion tests if a subspace should be further divided or not. A subspace should be further divided if the standard deviation of the values for the pixels that fall in the subspace is greater or equal to half of the standard deviation of pixel values in the mother subspace. The mother subspace is defined as the subspace of the previous segmentation level which generates the  $s_{ij}$  subspace. The mother subspace of the first level of subspaces is channels  $c_1$  and  $c_2$ . A subspace that satisfies the second criterion in at least one of the two channels should be further divided. This is because pixels which belong to a subspace can be homogenous with low standard deviation in one channel but inhomogeneous with high standard deviation in the other channel. Such pixels were presented in some cropland regions in our study area (e.g., bright regions in the following section).

For each subspace which satisfies the criteria defined in (4-7), the procedure entails the recalculation of histograms of the subspace in the two channels and a new thresholding of these histograms using the nonparametric histogram thresholding algorithm. Consequently, subspaces of each segmentation level serve as input for the following level in which the inherent histogram variations are further exploited. The segmentation procedure terminates when no subspace satisfies (4-7). The topology between segmentation levels is preserved, leading to the hierarchicalization of the produced subspaces. The latter is very important when segmentation results are introduced in a classification procedure (Dabboor and Karathanassi, 2005).

## **4.4.2 Implementation**

### 4.4.2.1 Preprocessing

TerraSAR-X dual co-polarized data (HH and VV), acquired in the southwest of the United Kingdom, are used in this test case (see Chapter 3). The Lee filter (Lee, 1981)

and the refined Lee filter (Lee et al., 1991) were applied to the available data and the Equivalent Number of Looks (ENL) was calculated (Anfinsen et al., 2008). The Lee filter gave a mean ENL = 7 while the refined Lee filter gave a mean ENL = 30. Thus, the refined Lee filter is used for the purpose of this study, since it gives higher ENL. As mentioned before, experiments showed that better segmentation results are produced when a refined 7x7 Lee is applied three times (Lee et al., 2001; De Grandi et al., 2004). This 7x7 size is the commonly used size in the different segmentation and classification approaches of SAR data that favours speckle reduction without leading to over-smoothing (De Grandi et al., 2004; Park and Moon, 2007; Gao and Ban, 2008).

#### 4.4.2.2 Segmentation Results

The segmentation methodology was applied on the first two components of the Pauli scattering vector, HH+VV and HH-VV images (Figures 4.10a and b, respectively), instead of the initial image channels HH and VV.

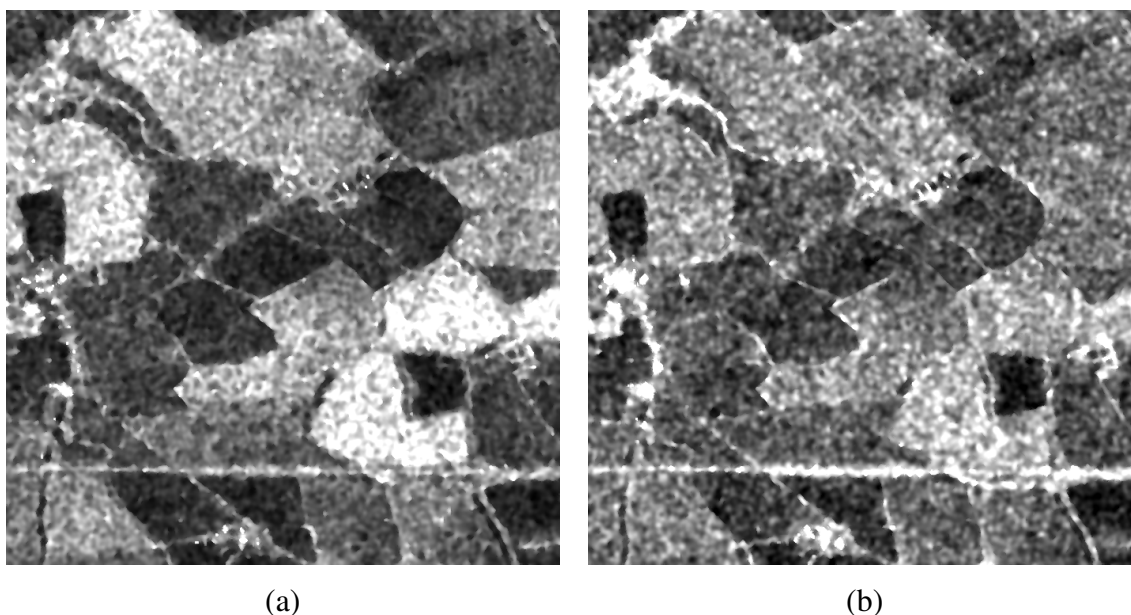


**Figure 4.10: a) The HH+VV after speckle filtering using a refined Lee filter, b) The HH-VV after speckle filtering using a refined Lee filter.**

This is because a better representation of the different land cover types is achieved with these images (Lee et al. (2001); Dabboor et al. (2008); Trouve et al. (2008)). A flowchart of the segmentation approach is shown in Figure 4.11.

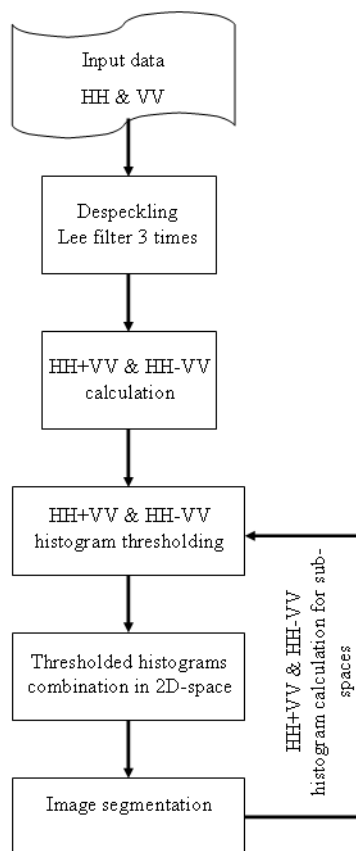


**Figure 4.11: Flowchart of the segmentation approach for dual polarized SAR data.**

Four segmentation levels are calculated in this study. In the first level, the histograms of the HH+VV and HH-VV images are calculated and the histogram thresholding algorithm is applied. The first segmentation level is produced after the histogram of the HH+VV image is automatically thresholded into three regions while the histogram of the HH-VV image is automatically thresholded into two regions, i.e., the two dimensional histogram-based space produced by combining two thresholded histograms is divided into six subspaces. Figure 4.12 shows the thresholded histograms of the HH+VV and HH-VV images and the six subspaces produced by the combination of the two thresholded histograms. Each subspace corresponds to a number of segments in

the first segmentation level. The borders (red colour) of the segments are extracted and overlain on a composite image (Green = HH+VV, Blue = HH-VV) for improved visualization, Figure 4.13a.

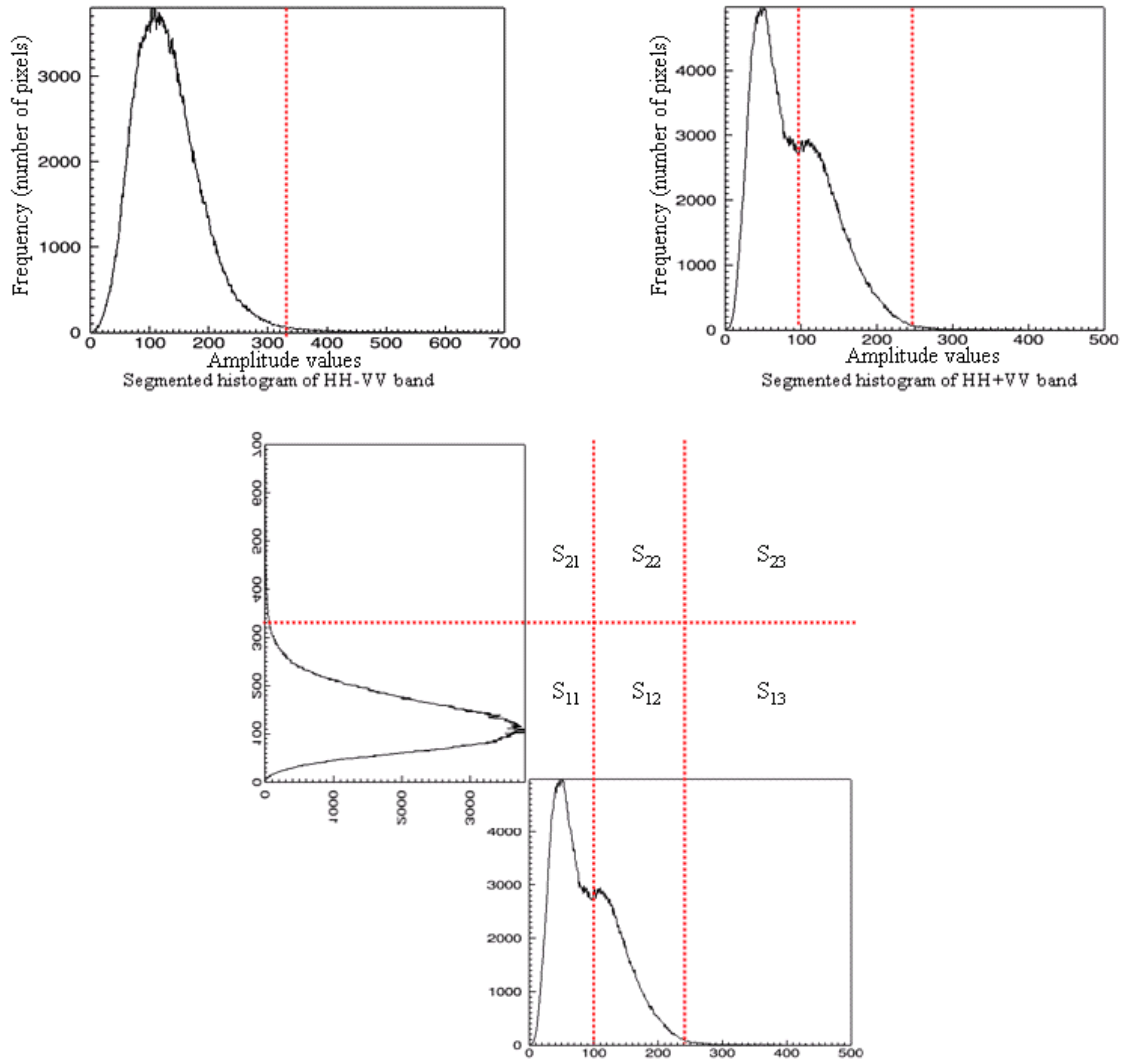


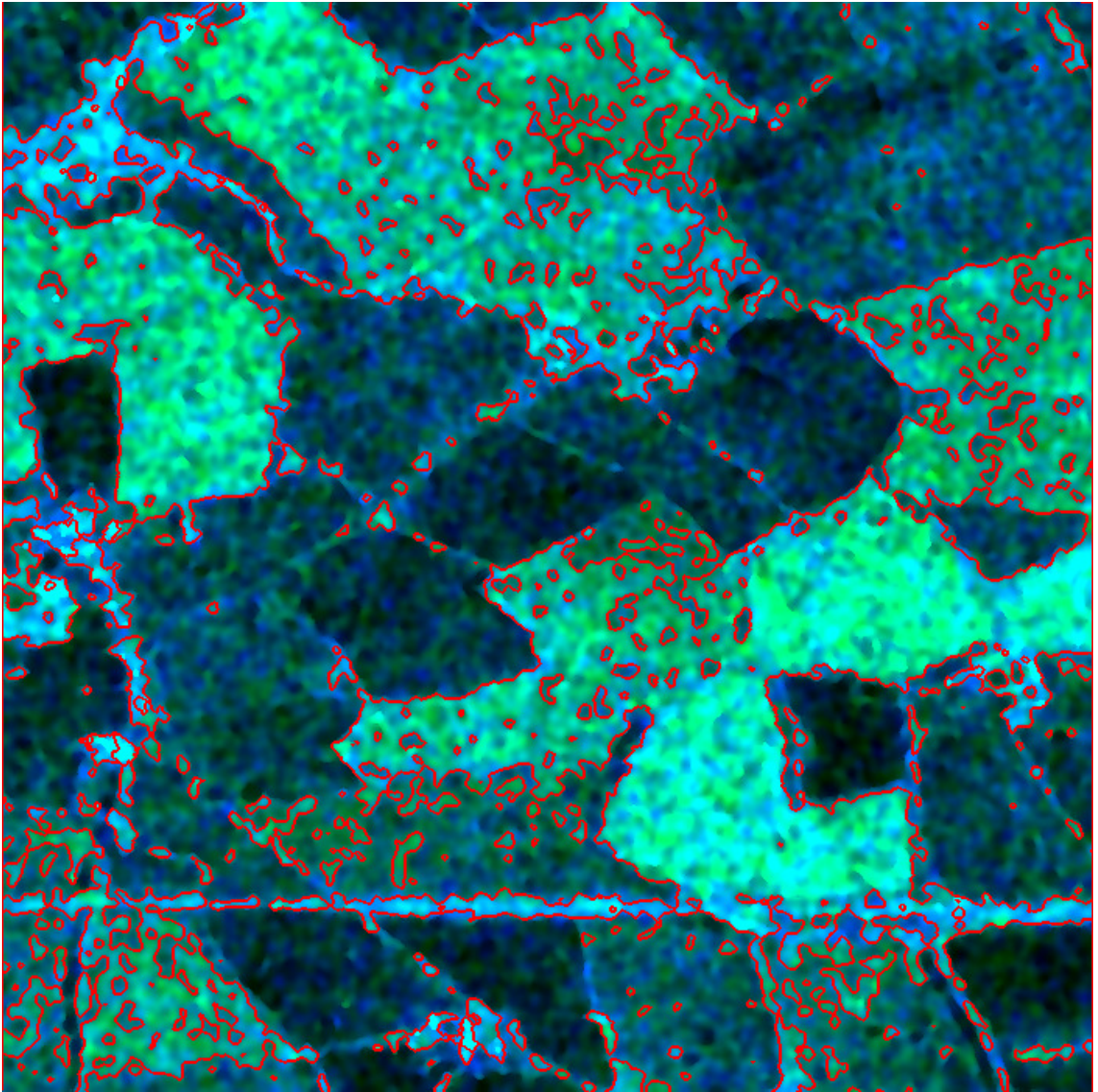
**Figure 4.12: The HH+VV and HH-VV thresholded histograms and the sub-spaces produced by combing them in a two dimensional histogram-based space.**

The output of the first segmentation level serves as input for the next segmentation level. According to equation (4-7), only the subspaces  $s_{11}^1$  and  $s_{12}^1$  served as input for the next segmentation level. Herein, the mother subspace for the  $s_{11}^1$  and  $s_{12}^1$  child subspaces are the whole HH+VV and HH-VV images. For the  $s_{11}^1$  subspace, the

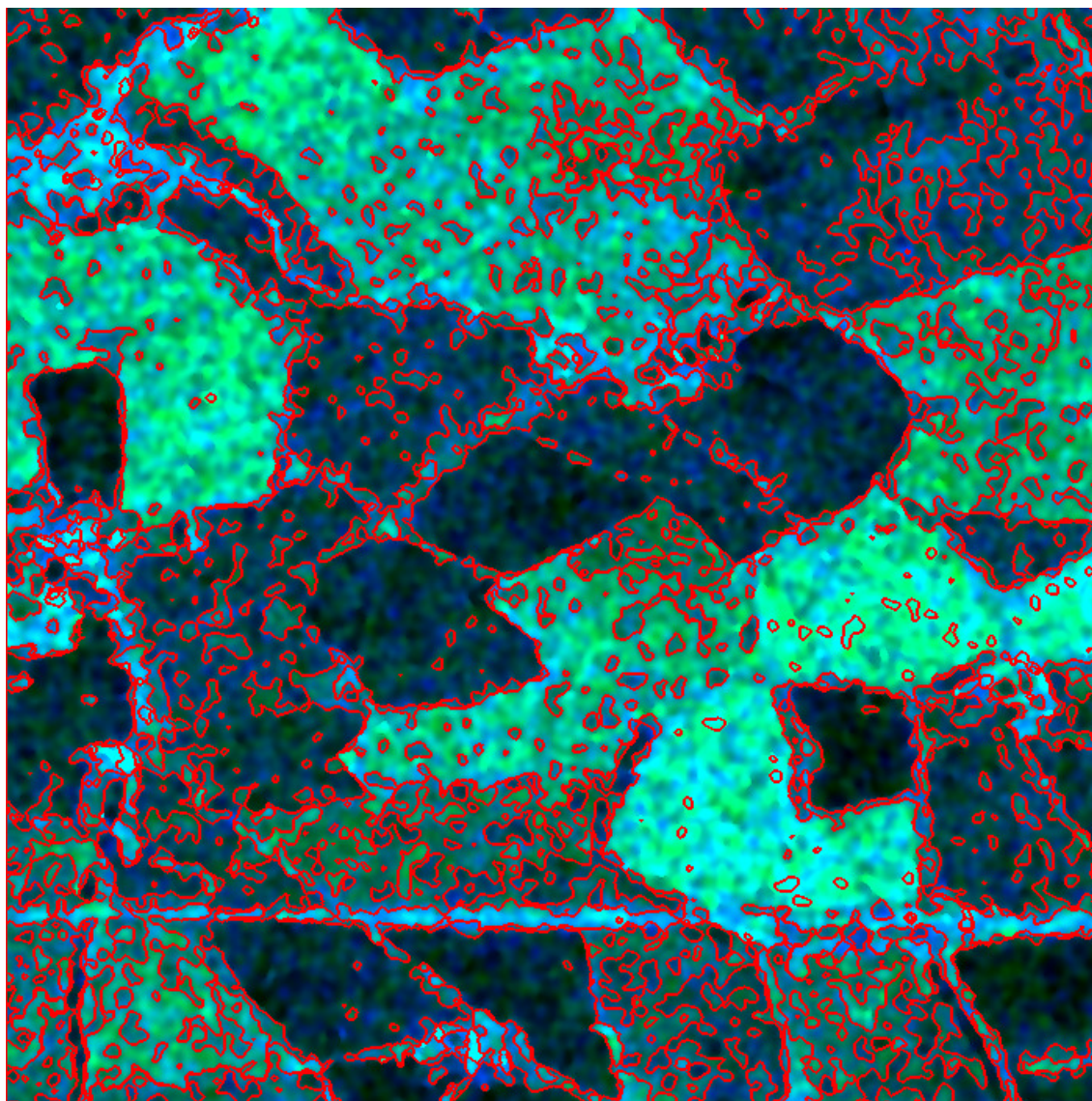
HH+VV histogram is automatically thresholded by the histogram thresholding algorithm into three regions while the HH-VV histogram is thresholded into two regions. Thus, the combination of the two histograms divides the two dimensional histogram-based space of the  $s_{11}^1$  subspace into six new subspaces. For the  $s_{12}^1$  subspace, the HH+VV and HH-VV histograms are automatically thresholded into three and two regions, respectively. Consequently, six new subspaces are produced. The borders of the resulting segments are extracted and shown in, Figure 4.13b.

In the third segmentation level, the child subspace  $s_{12}^2$  produced from the mother subspace  $s_{12}^1$  and the child subspace  $s_{11}^2$  produced from the mother subspace  $s_{11}^1$  are further divided. The HH+VV and HH-VV histograms of the  $s_{12}^2$  subspace are divided into three and two regions, respectively. The two dimensional space is divided into six subspaces. For the subspace  $s_{11}^2$ , the HH+VV and HH-VV histograms are thresholded into three and four regions, respectively. Consequently, the two dimensional histogram-based space is divided into twelve subspaces. The results of the third segmentation level are shown in Figure 4.13c.

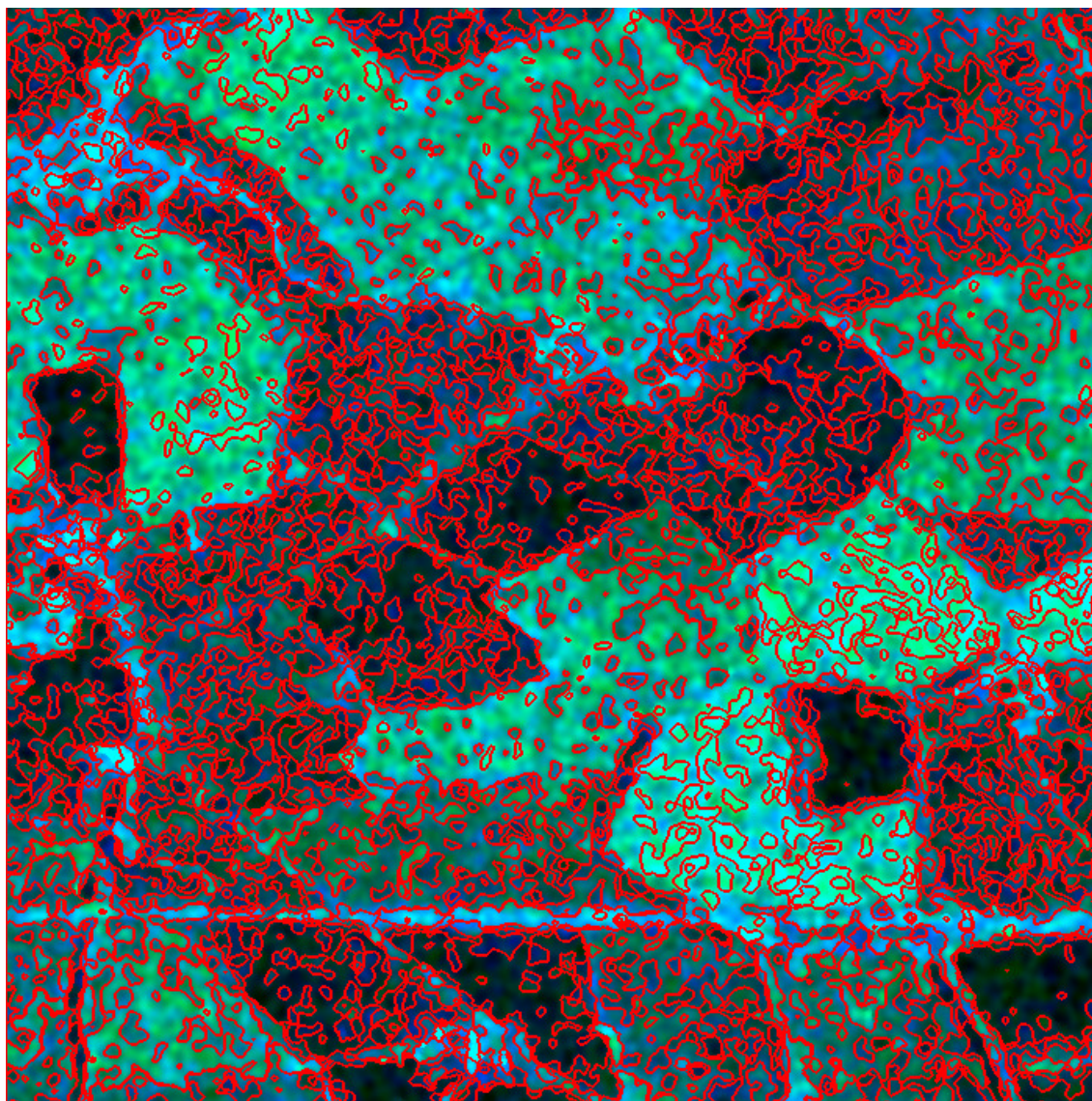
More detailed segmentation is obtained through a fourth segmentation level. Based on relations defined in equation (4-7), the subspace  $s_{11}^3$  of the third segmentation level should be further divided. The child subspace  $s_{11}^3$  has  $s_{12}^2$  as a mother subspace from the second segmentation level. Thus, the HH+VV and HH-VV histograms of the subspace  $s_{11}^3$  are thresholded into four and two regions, respectively. Thus, the two dimensional histogram-based space is divided into eight subspaces. The output of the fourth segmentation level is shown in Figure 4.13d.



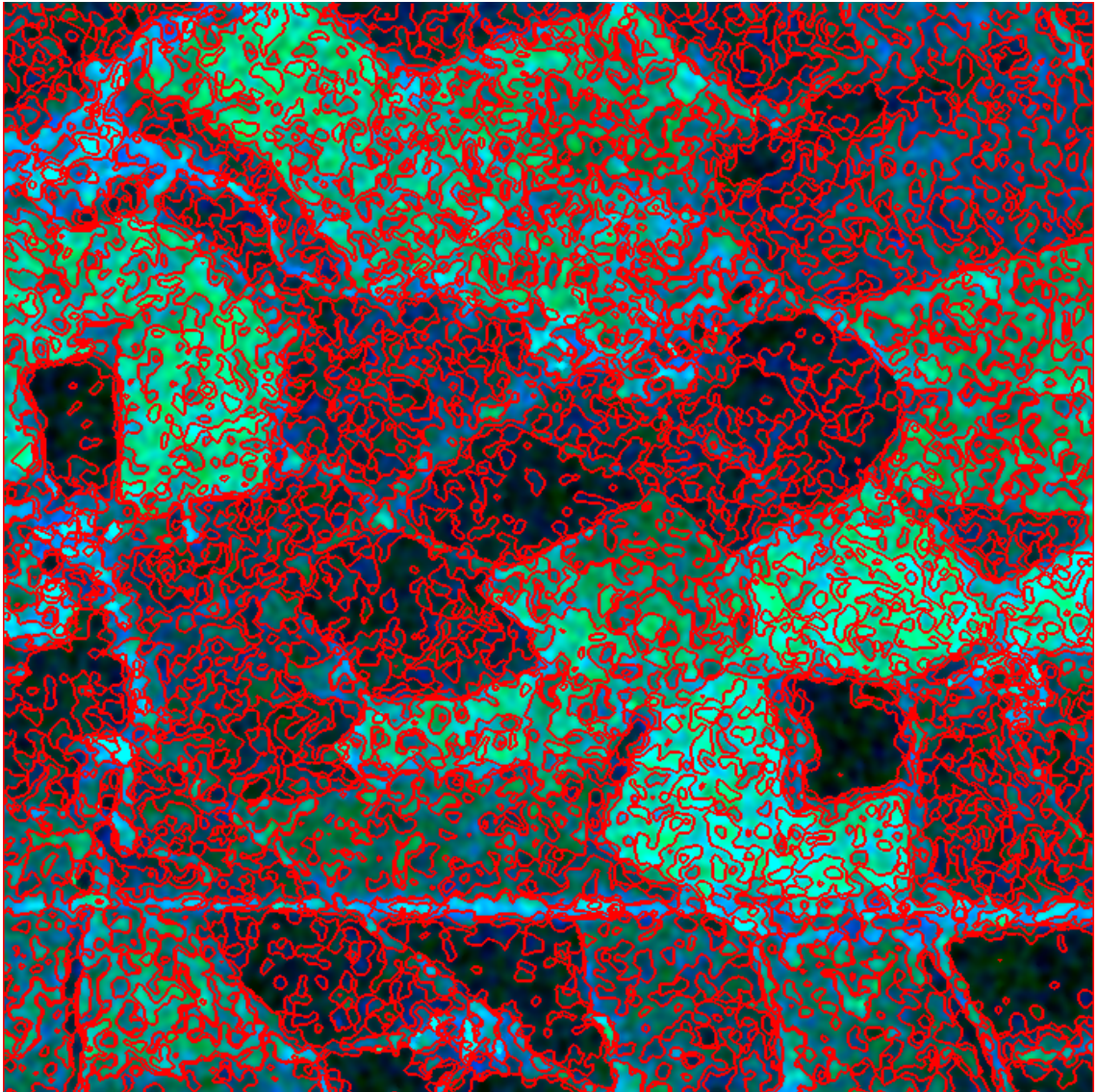
(a)



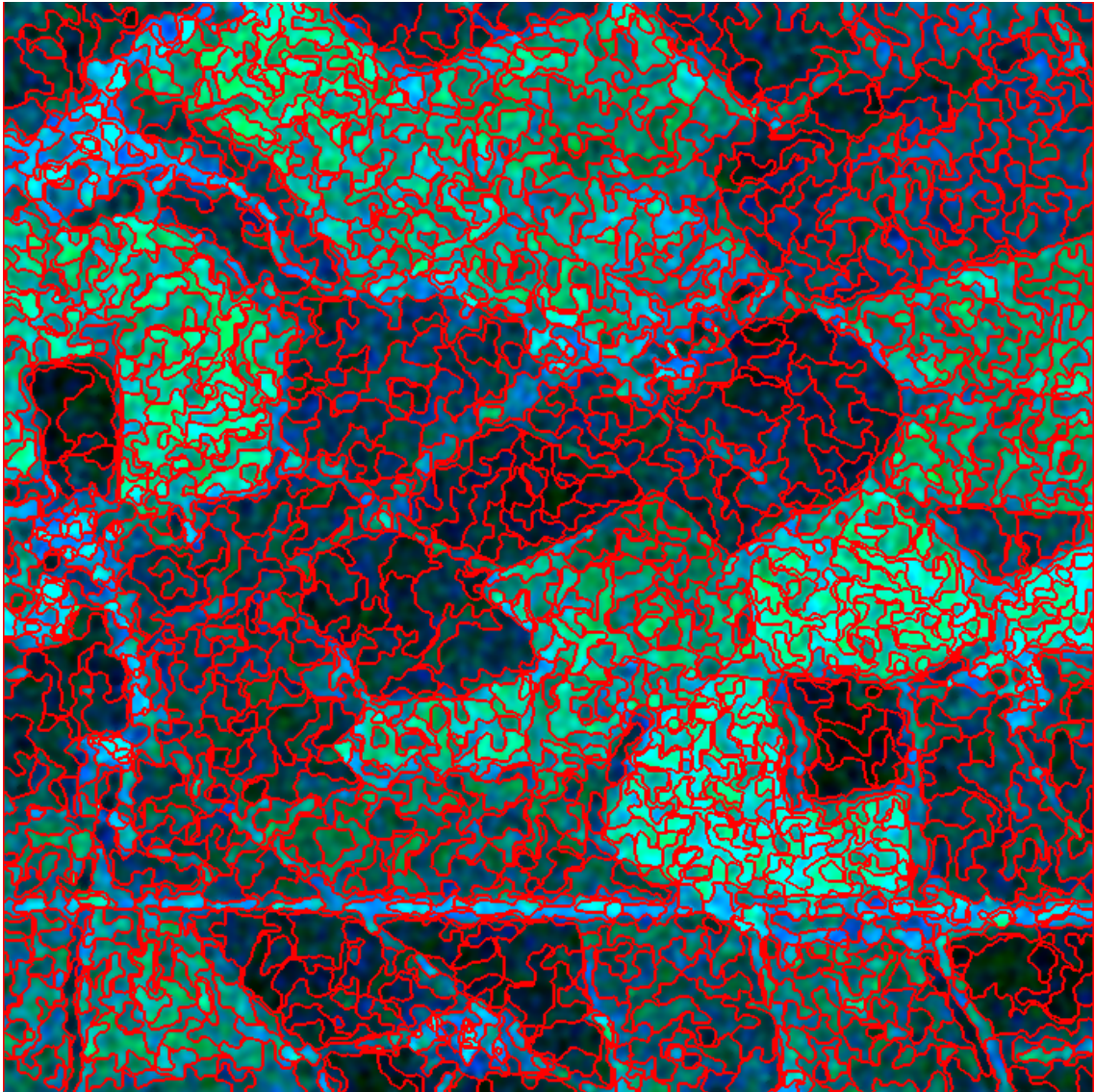
(b)



(c)



(d)



(e)

**Figure 4.13: The extracted borders (red colour) of the resulting segments overlain on a composited image (Green =  $HH+VV$ , Blue =  $HH-VV$ ) for a) First segmentation level, b) Second segmentation level, c) Third segmentation level, d) Fourth segmentation level, (e) Fourth segmentation level produced by the *eCognition*.**

For comparison purposes, the segmentation task is implemented using the segmentation algorithm of the *eCognition* software package (Baatz and Schäpe, 2000). The latter performs multilevel segmentation based on the split-merge concept. The algorithm is based on both homogeneity and shape criteria. Furthermore, a scale parameter that controls the average size of the resulting segments in each segmentation

level is defined (Tzotsos and Argialas, 2006). The same input data set is used by the *e*Cognition segmentation algorithm. Four segmentation levels (top-down) are produced. Giving emphasis on the colour criteria, the following parameter values have been introduced: first level: scale = 300, colour = 0.9, shape = 0.1, second level: scale = 150, colour = 0.9, shape = 0.1, third level: scale = 70, color = 0.8, shape = 0.2, fourth level: scale = 32, colour = 0.9, shape = 0.1. Figure 4.13e shows the final segmentation results (fourth segmentation level) produced based on the *e*Cognition segmentation algorithm.

#### 4.4.2.3 Discussion

In the first segmentation level an adequate separation between image objects that appear dark and those which appear bright in the composite image is obtained (Figure 4.13a). Segments present various sizes without any limitation in size. Small size segments are contained within big contiguous ones. This is because the histogram based segmentation approach acts globally. Segments are obtained from subspaces that are produced by the division of the two dimensional histogram-based space. The small segments correspond to strong "anomalies" that exist in homogeneous land covers. Example of "anomalies" could be areas of a field that has better drainage due to the local micro-relief, variable soil type or geological faults/fractures.

In the second segmentation level (Figure 4.13b), a more detailed segmentation is achieved for the segments which are associated with the subspaces that satisfy the two criteria established in equation (4-7). According to the first criterion, small segments which would be produced by the filtered subspaces are avoided. Moreover, colour heterogeneity in the produced segments is adjusted by the second criterion.

In the third and fourth segmentation levels (Figures 4.13c and d, respectively) an even more detailed segmentation is achieved. The image is completely segmented into almost homogeneous segments with regard to the colours apparent in the composite image. Many segments are observed within others. However, due to their density, many of the segments are contiguous. The level of heterogeneity within segments is always controlled by the second criterion (Figure 4.14e, yellow arrows).

The concept of the proposed segmentation is different from the segmentation concept implemented in the *eCognition* software package. The proposed segmentation algorithm is histogram-based and acts globally, whereas the *eCognition* algorithm is image-based, acts locally, and produces only contiguous segments. Thus, the two approaches perform the segmentation process from different points of view. The scale parameter used by the *eCognition* algorithm controls the average size of the segments, leading to a relation between segment size and segmentation level. Thus, this parameter prohibits the production of various size segments within a segmentation level. Anomalies inside homogeneous land covers are not observed in the first segmentation levels. These "anomalies" can be separated into individual segments only in the detailed segmentation levels, i.e. in the third and fourth level.

The fourth segmentation level of the two approaches is shown in Figures 4.13d and e, respectively. The different segmentation concepts are obvious in the results. Extremely small segments corresponding to high changes in colour values give the impression of over-segmentation in case of the proposed algorithm (yellow arrows in Figure 4.14a). These segments are not produced by the *eCognition* algorithm which is controlled by the scale parameter (Figure 4.14b). However, this parameter affects the quality of the results (Figures 4.14b, d, and f). Details of the fourth segmentation level in Figures 4.14a-d show that the histogram based methodology produces more reliable results in terms of homogeneity within the produced segments. Black and white arrows indicate such areas.

Both segmentation approaches preserve the topology information, which is important for building rules in a knowledge-based classification approach. However, because of the different concepts the two segmentation approaches follow, the topology information of the segments is produced in different spaces. In the proposed segmentation approach, the topological relationship mother-child of the segments is in the two dimensional histogram-based space. This leads to a strong relationship between subspaces and scattering behaviour of land covers. Each subspace, as well as its place in the mother-child tree fits to a specific scattering behaviour. This may be used for classifying the generated segments by this subspace. Other attributes of the segments,

such as spatial, can also be used. In *eCognition*, the topological relationship mother-child of the segments is in the two-dimensional space of the image.

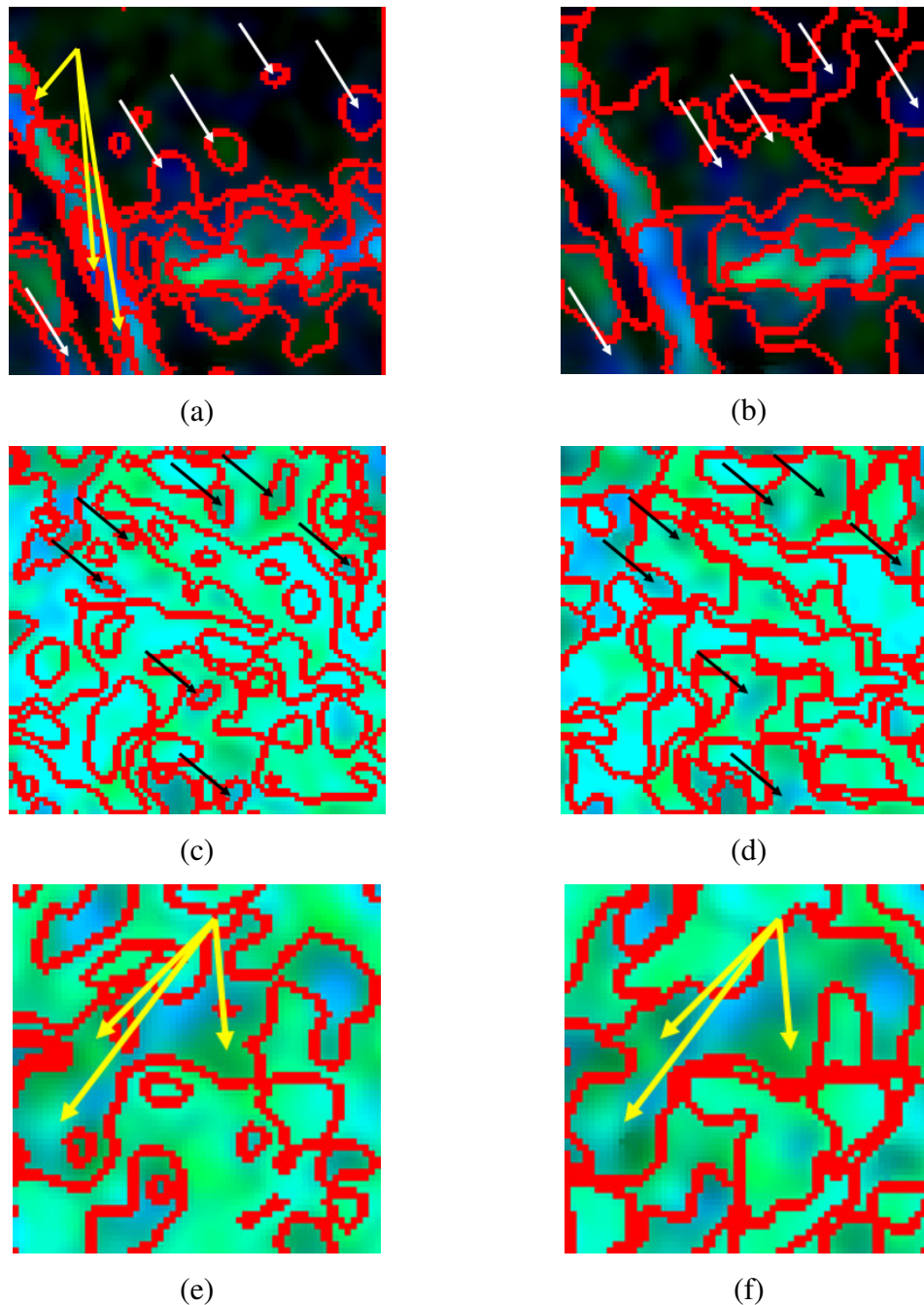


**Figure 4.14:** a), c) and e) Sample areas from the final (fourth) segmentation level produced by histogram thresholding. b), d) and f) Sample areas from the final (fourth) segmentation level produced by *eCognition*.

## 4.5 Summary

This research presents two multilevel divisive segmentation methodologies for full and dual polarimetric SAR data. Both methodologies have in common the use of a nonparametric histogram thresholding algorithm.

The first methodology proposes a hierarchical segmentation approach for full polarimetric SAR data which exploits the scattering information obtained from the polarimetric SAR analysis methods and goes beyond the traditional segmentation methods. The first two segmentation levels are based on the hierarchicalization of scattering mechanisms. Having accomplished the information of the scattering behavior, further segmentation levels were obtained by dividing the histogram of the dominant scattering mechanism for the subareas defined by the second segmentation level into homogeneous regions. Thus, the inherent variations within the dominant scattering mechanism are exploited in order to get a more detailed segmentation. The proposed methodology accepts the complexity of real objects by evaluating the two most important scattering mechanisms that characterize their scattering behavior. The methodology produces comparable segmentation results for both Pauli and Freeman-Durden decomposition images. Different RGB colours are well outlined and attributed to different segments and edges are quite smooth. The user can select segments of interest and further segment them through additional segmentation levels according to the study requirements. In any case, further segmentation creates smaller independent segments. Selective segmentation avoids over splitting for segments adequately delimited and well associated to a classification class. In comparison to the k-means clustering algorithm, better segmentation results can be achieved by the proposed method as it prohibits the over-segmentation of the SAR data, preserving at the same time the polarimetric scattering information.

The second methodology proposes a hierarchical segmentation approach for dual polarized SAR data that acts globally, by exploiting the scattering information of the two channels through the combination of their thresholded histograms in a two dimensional histogram-based space. Two criteria, the first based on the number of pixels in each

subspace and the second based on the standard deviation of the pixel values included in the subspaces, are established, which control the generation of the segmentation levels. In each segmentation level, segments present various sizes without any limitation in size. Thus, large segments can include smaller ones which denote "anomalies" inside the large homogeneous segments, helping in recognition of small radar targets. Segmentation results were compared with those obtained using the *eCognition* segmentation algorithm. It was clear based on the segmentation results of both approaches that the differences in segmentation concept, in which the proposed methodology acts globally and produces segments based on subspaces of a two dimensional histogram-based space, and in which the *eCognition* segmentation algorithm acts locally in the two dimensional space of the image, are conceptual differences. However, the range of applications which need to consider different segment sizes likely exceeds the ones which focus on one scale only.

## Chapter Five: Polarimetric SAR Agglomerative Clustering

In this chapter, a new probabilistic distance, called Wishart Chernoff distance, is discussed (Dabboor et al., 2010c). The proposed distance is used in an agglomerative clustering approach for polarimetric SAR data segmentation. Results are compared with those obtained based on the Wishart test statistic distance.

### 5.1 Introduction

Agglomerative clustering can be used as a technique for unsupervised polarimetric SAR data segmentation. Data are initially segmented into small clusters. Later, initial clusters are merged hierarchically into an appropriate number of larger clusters (classes). Similarity criteria are used for merging of clusters. In this chapter, a new probabilistic distance is proposed as a similarity criterion. The Chernoff distance which measures the distance between two distributions is derived for the Complex Wishart distribution. The proposed criterion overcomes the drawbacks of the existing criteria by: 1) measuring the similarity of two clusters independently of the number of samples (pixels) in each cluster, 2) measuring the similarity of two clusters by statistically measuring the similarity of their distributions. The following section discusses analytically the derivation of the new criterion, called Wishart Chernoff distance.

### 5.2 Wishart Chernoff Probabilistic Distance

#### 5.2.1 The Complex Wishart Distribution

Assuming that the target scattering vector  $\bar{k}_p$  is a complex normal vector follows a complex Gaussian (or Normal) distribution, the probability density function of the  $n$ -look sample coherency matrix  $T$  is given by Lee et al. (1994) as

$$p(T) = \frac{n^{qn}}{k(n,q)|V|^n} |T|^{(n-q)} e^{-n\text{Tr}(V^{-1}T)}, \quad (5-1)$$

where  $q=3$  for the reciprocal case and  $q=4$  for the bistatic case, and  $k(n,q) = \pi^{q(q-1)/2} \Gamma(n) \dots \Gamma(n-q+1)$  ( $\Gamma$  is the Gamma function).  $V = E[T]$  (the expected value of  $T$ ) is the cluster center coherency matrix and can be calculated by

$$V_i = \frac{1}{N_i} \sum_{i=1}^{N_i} T_i, \quad (5-2)$$

where  $N_i$  is the number of samples within the  $i$ th cluster.

### 5.2.2 Chernoff Error Bound

Assume that a data vector  $x$  belongs to one of two possible classes  $\omega_1$  or  $\omega_2$ . It is required to determine which one of the following two hypotheses is more likely to occur (El Ayadi et al., 2008):

$H_1$  :  $x$  comes from the class  $\omega_1$

$H_2$  :  $x$  comes from the class  $\omega_2$

It is usually assumed that data vectors belonging to each class  $\omega_i$ ,  $i=1,2$ , follow a certain distribution  $p(x/\omega_i)$ . According to the Bayesian decision theory (Duda et al., 2000), the optimal decision rule is given by

$$P(\omega_1)p(x/\omega_1) \underset{H_1}{\overset{H_2}{>}} P(\omega_2)p(x/\omega_2), \quad (5-3)$$

where  $P(\omega_i)$  is the a priori probability. A classification error occurs if a data vector  $x$  belongs to one class but falls in the decision region of the other class. The calculation of the error probability is quite difficult, especially for higher dimensions (Duda et al., 2000). However, in the two-category case, the Chernoff bound gives an upper bound of the error. For the complex Wishart distribution, the Chernoff bound is given by

$$P(\text{error}) \leq P^{\beta}(V_1)P^{1-\beta}(V_2) \int p^{\beta}(T/V_1) p^{1-\beta}(T/V_2) dT \quad (5-4)$$

where  $\beta$  is a parameter,  $0 \leq \beta \leq 1$ , and  $T$  is the sample coherency matrix. The integral in (5-4) can be evaluated analytically, yielding

$$\int p^{\beta}(T/V_1) p^{1-\beta}(T/V_2) dT = e^{-f(\beta)}, \quad (5-5)$$

where  $f(\beta)$  is a function of the parameter  $\beta$ , called the Wishart Chernoff distance. The Wishart Chernoff distance  $f(\beta)$  measures the similarity between two Wishart complex distributions. It can be calculated by assuming  $L$  so that

$$L = p_1^{\beta}(T) p_2^{(1-\beta)}(T). \quad (5-6)$$

Taking into account (5-1), (5-6) can be rewritten as follows:

$$\begin{aligned}
L &= \frac{n^{\beta q n}}{k^\beta(n, q) |V_1|^{\beta n}} |T|^{\beta(n-q)} e^{-\beta n \text{Tr}(V_1^{-1} T)} \\
&\cdot \frac{n^{(1-\beta) q n}}{k^{(1-\beta)}(n, q) |V_2|^{(1-\beta)n}} |T|^{(1-\beta)(n-q)} e^{-(1-\beta)n \text{Tr}(V_2^{-1} T)} \\
&= \frac{n^{qn}}{k(n, q) |V_1|^{\beta n} |V_2|^{(1-\beta)n}} |T|^{(n-q)} e^{-\beta n \text{Tr}(V_1^{-1} T) - n \text{Tr}(V_2^{-1} T) + \beta n \text{Tr}(V_2^{-1} T)} \\
&= \frac{n^{qn}}{k(n, q) |V_1|^{\beta n} |V_2|^{(1-\beta)n}} |T|^{(n-q)} e^{\text{Tr}(-\beta n V_1^{-1} T - n V_2^{-1} T + \beta n V_2^{-1} T)}.
\end{aligned} \tag{5-7}$$

Letting  $V = \beta n V_1^{-1} + n V_2^{-1} - \beta n V_2^{-1}$ , (5-7) can be rewritten as

$$L = \frac{n^{qn}}{k(n, q) |V_1|^{\beta n} |V_2|^{(1-\beta)n}} |T|^{(n-q)} e^{-\text{Tr}(VT)}. \tag{5-8}$$

So, the integral in (5-5) according to Khatri (1966), is equal to

$$\begin{aligned}
&\int p^\beta(T/\omega_1) p^{1-\beta}(T/\omega_2) dT \\
&= \frac{n^{qn}}{k(n, q) |V_1|^{\beta n} |V_2|^{(1-\beta)n}} \int |T|^{(n-q)} e^{-\text{Tr}(VT)} dT \\
&= \frac{n^{qn}}{k(n, q) |V_1|^{\beta n} |V_2|^{(1-\beta)n}} \cdot n^{n(1-q)} k(n, q) |V|^{-n} \\
&= \frac{n^n |V|^{-n}}{|V_1|^{\beta n} |V_2|^{(1-\beta)n}} = \left[ \frac{n |V|^{-1}}{|V_1|^\beta |V_2|^{(1-\beta)}} \right]^n = e^{-f(\beta)}.
\end{aligned} \tag{5-9}$$

Thus, the Wishart Chernoff distance can be defined as

$$\begin{aligned}
f(\beta) &= -n \ln \left[ \frac{n|V|^{-1}}{|V_1|^\beta |V_2|^{(1-\beta)}} \right] \\
&= -n \ln \left[ \frac{n|\beta n V_1^{-1} + n V_2^{-1} - \beta n V_2^{-1}|^{-1}}{|V_1|^\beta |V_2|^{(1-\beta)}} \right] \\
&= -n \ln \left[ \frac{|\beta V_1^{-1} + (1-\beta)V_2^{-1}|^{-1}}{|V_1|^\beta |V_2|^{(1-\beta)}} \right].
\end{aligned} \tag{5-10}$$

In (5-10),  $n$  (number of looks) is a scale parameter which does not affect the distance between two clusters and can be omitted for simplification. Hence, the Wishart Chernoff distance becomes

$$f(\beta) = -\ln \left[ \frac{|\beta V_1^{-1} + (1-\beta)V_2^{-1}|^{-1}}{|V_1|^\beta |V_2|^{(1-\beta)}} \right] \tag{5-11}$$

The Chernoff distance is a probabilistic distance between two distributions and can be used as a criterion for estimating the similarity between the respective probability densities. Since the Wishart Chernoff distance in (5-11) is independent of the number of looks, it can be applied to multilook processed or speckle filtered POLSAR data. In addition, the Wishart Chernoff distance is symmetric: the distance between two complex Wishart distributions  $V_1$  and  $V_2$  respectively for  $\beta = \beta_1$  is equal to the distance between  $V_2$  and  $V_1$  for  $\beta = \beta_2$ , where  $\beta_2 = 1 - \beta_1$ . Moreover, the Wishart Chernoff distance is independent of the polarization basis, e.g. linear or circular polarization basis. The data in covariance matrices, coherency matrices, circular polarization matrices, would produce identical classification result.

*Proof:* Assume an alternative polarization base  $\nu$  which is related to the current base  $u$  by (Dabboor et al., 2010c)

$$\nu = Pu, \tag{5-12}$$

where  $P$  is a constant matrix. Then, a multilook coherency matrix can be formed as,

$$Z = \frac{1}{n} \sum_{k=1}^n v(k) \cdot v(k)^+ = PTP^+ \quad (5-13)$$

where  $^+$  denotes the complex conjugate transpose. So, the  $i$ th cluster center coherency matrix can be calculated by

$$M_i = \frac{1}{N_i} \sum_{i=1}^{N_i} Z_i = PV_iP^+ . \quad (5-14)$$

Thus, the Wishart Chernoff distance between two clusters  $M_1 = PV_1P^+$  and  $M_2 = PV_2P^+$  is

$$\begin{aligned} f(\beta) &= -\ln \left[ \frac{|\beta(PV_1P^+)^{-1} + (1-\beta)(PV_2P^+)^{-1}|^{-1}}{|PV_1P^+|^\beta |PV_2P^+|^{(1-\beta)}} \right] \quad (5-15) \\ &= -\ln \left[ \frac{|\beta P^{+1}V_1^{-1}P^{-1} + (1-\beta)P^{+1}V_2^{-1}P^{-1}|^{-1}}{|PV_1P^+|^\beta |PV_2P^+|^{(1-\beta)}} \right] \\ &= -\ln \left[ \frac{P^{+1}[\beta V_1^{-1} + (1-\beta)V_2^{-1}]P^{-1}|^{-1}}{|PV_1P^+|^\beta |PV_2P^+|^{(1-\beta)}} \right]. \end{aligned}$$

Since  $|AB| = |A||B|$ , the Wishart Chernoff distance becomes

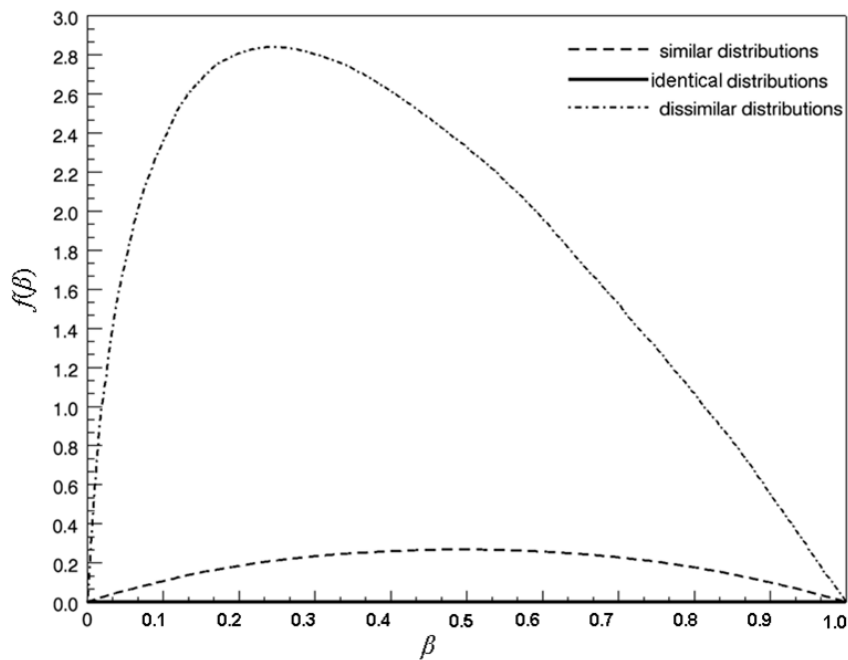
$$\begin{aligned}
f(\beta) &= -\ln \left[ \frac{|P^{+1}|^{-1} |\beta V_1^{-1} + (1-\beta)V_2^{-1}|^{-1} |P^{-1}|^{-1}}{|P|^\beta |V_1|^\beta |P^+|^\beta |P|^{(1-\beta)} |V_2|^{(1-\beta)} |P^+|^{(1-\beta)}} \right] \\
&= -\ln \left[ \frac{|P^{+1}|^{-1} |\beta V_1^{-1} + (1-\beta)V_2^{-1}|^{-1} |P^{-1}|^{-1}}{|P^+| |V_1|^\beta |V_2|^{(1-\beta)} |P|} \right] \\
&= -\ln \left[ \frac{|\beta V_1^{-1} + (1-\beta)V_2^{-1}|^{-1}}{|V_1|^\beta |V_2|^{(1-\beta)}} \right].
\end{aligned} \tag{5-16}$$

However, there is an apparent limitation in the matrix  $P$ . The matrix  $Z$  is a function of  $P$  and it has to be Hermitian and positive semidefinite to obey the complex Wishart distribution (Duda et al., 2000).

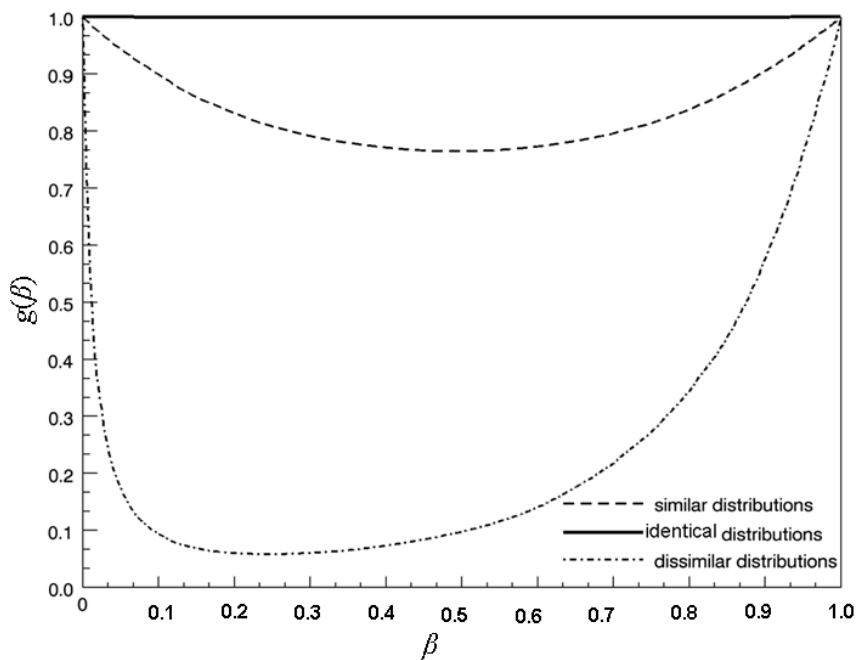
The optimum Wishart Chernoff distance  $f(\beta)$  which best describes the similarity between two distributions is calculated by finding the value  $\beta_{opt}$  that minimizes

$$g(\beta) = \frac{|\beta V_1^{-1} + (1-\beta)V_2^{-1}|^{-1}}{|V_1|^\beta |V_2|^{(1-\beta)}} = e^{-f(\beta)}. \tag{5-17}$$

The key benefit here is that this optimization is in the one-dimensional  $\beta$  space (Duda et al., 2000). The value  $\beta_{opt}$  corresponds to the value of  $\beta$  that minimizes the classification error probability. Simulated data can be used to empirically study the behavior of the  $g(\beta)$  function. The parameter  $\beta$  is calculated randomly using a Monte Carlo simulation technique. Given that two distributions are identical, the Wishart Chernoff distance  $f(\beta)$  is expected to be zero, Figure 5.1a (solid line). In this case,  $g(\beta)$  is a constant, independent of  $\beta$  with  $g(\beta) = 1$ , Figure 5.1b (solid line).



(a)



(b)

**Figure 5.1:** a) The graph of  $f(\beta)$  for two statistically identical distributions (solid line), similar distributions (dashed line), and dissimilar distributions (dot-dashed line), b) The graph of  $g(\beta)$  for two statistically identical distributions (solid line), similar distributions (dashed line), and dissimilar distributions (dot-dashed line).

Two distributions are assumed similar if they have same scale parameter (have identical scale) but different mean locations. In this case, the  $\beta_{opt}$  is expected to be 0.5. In this case, the Wishart Chernoff distance depends on the difference of the distribution mean locations. For the two distributions in Figure 5.1a (dashed line), for example, the Wishart Chernoff distance is small, thus the graph of  $g(\beta)$  has a slight curvature, with  $g(\beta_{opt})$  close to one for  $\beta_{opt}$  equal to 0.5, Figure 5.1b (dashed line). Higher difference between the mean locations of the two distributions will result in higher curvature of the graph of  $g(\beta)$ . The higher the curvature of  $g(\beta)$  the lower the value of  $g(\beta_{opt})$ , which results in higher Wishart Chernoff distance values.

Two dissimilar distributions are assumed if they have different scale parameter and different or equal mean locations. In this case, the  $\beta_{opt}$  is expected to differ from 0.5. The more different the scale parameter of the two distributions, the closer the values of  $\beta_{opt}$  are to the bounds of the interval  $[0, 1]$ . In Figure 5.1b (dot-dashed line),  $\beta_{opt}$  is 0.25 and  $g(\beta_{opt})$  is close to zero, i.e., the Wishart Chernoff distance between the two distributions is larger, Figure 5.1a (dot-dashed line).

In the next section, the derived Wishart Chernoff distance is used in an agglomerative clustering approach for the unsupervised segmentation of full polarimetric SAR data. The robustness of the Wishart Chernoff distance to measure similarity between clusters will be shown, leading to better information captured from full polarimetric SAR data.

## **5.3 Agglomerative Clustering**

### **5.3.1 Methodology**

The initialization for the agglomerative hierarchical clustering can be obtained by dividing the polarimetric SAR data into clusters based on the SPAN/H/A/ $\alpha$  space (Cao et al., 2007). The SPAN can be defined as the total backscattering power and is equal to the trace of the coherency matrix  $T$

$$\text{SPAN} = T_{11} + T_{22} + T_{33}, \quad (5-18)$$

where  $T_{11}$ ,  $T_{22}$  and  $T_{33}$  are the diagonal elements of the coherency matrix. As suggested in Cao et al. (2007), a maximum of 48 optimal initial clusters can be obtained by performing the following three steps: 1) dividing the SPAN histogram into three clusters: low density, medium density, and high density, 2) further division into 24 clusters based on the  $H/\alpha$  plane, and 3) using the anisotropy  $A$  to divide the 24 clusters into 48. After each step, the complex Wishart clustering is performed to optimize the initialization.

Optimized initial clusters are merged hierarchically into an appropriate number of classes. Clusters are merged iteratively based on a probabilistic distance, such as the derived Wishart Chernoff distance. For each iteration, the distances of all possible pairs of clusters are calculated, and the two clusters with the minimum distance are merged to decrease the number of clusters by one. Merging continues until the appropriate number of classes is obtained.

The appropriate number of classes is estimated based on the data log-likelihood algorithm (Cao et al., 2007). The  $m$ th data log-likelihood is defined as

$$L_m(X) = \sum_{l=1}^N \ln \left( \sum_{i=1}^m \left( \frac{N_i}{N} \right) \cdot \exp(-n \cdot d_m(T_l, V_i)) \right), \quad (5-19)$$

where  $m$  is the number of clusters,  $N_i$  is the number of samples within the  $i$ th cluster,  $N$  is the number of samples within the whole data set and  $d_m(T_l, V_i)$  measures the distance between the  $l$ th sample coherency matrix  $T_l$  and the  $i$ th cluster center coherency matrix  $V_i$

$$d_m(T_l, V_i) = \ln|V_i| + \text{Tr}(V_i^{-1}T_l). \quad (5-20)$$

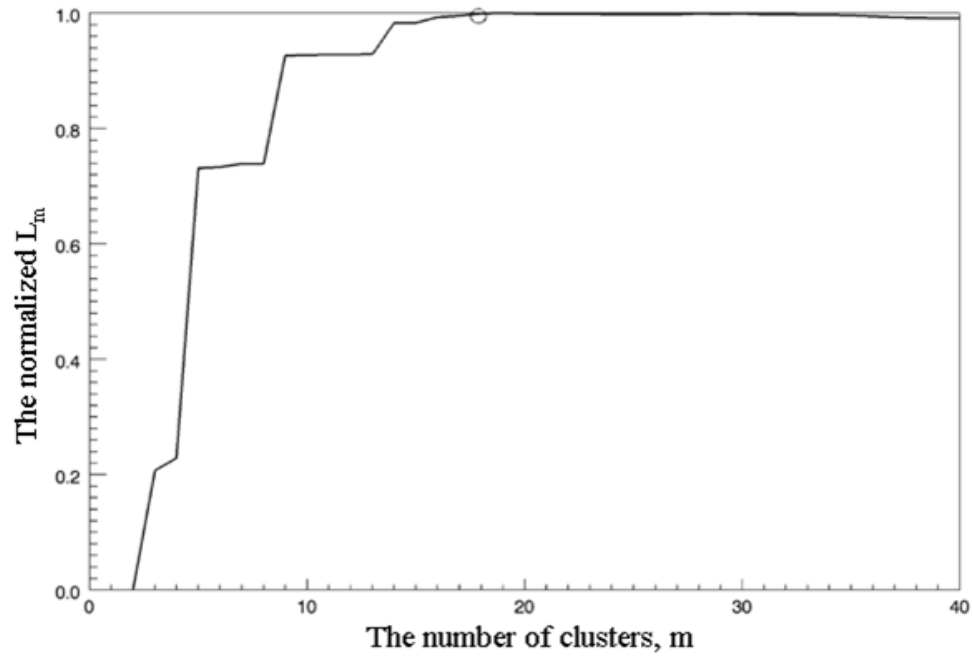
The data log-likelihood algorithm has the potential ability to reveal the inner structure of POLSAR data (Cao et al., 2007). This is because it quantitatively measures the fitness

between the number of clusters and the polarimetric SAR data inner structure. A log-likelihood value is calculated for each number of clusters  $m$ , starting from  $m$  equal to the number of clusters produced by the SPAN/H/A/ $\alpha$  initialization until  $m = 1$ .

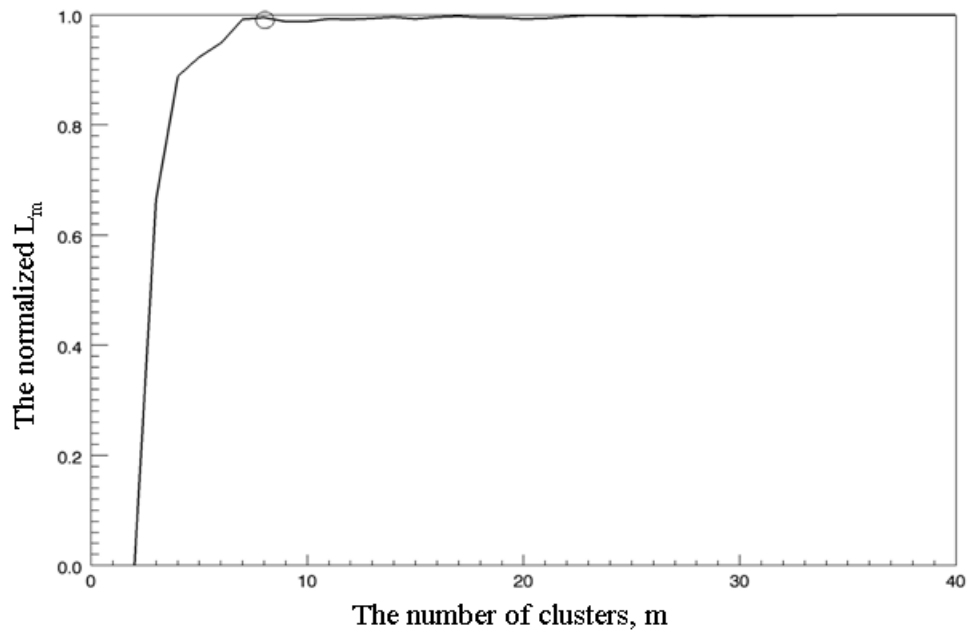
### ***5.3.2 Implementation and Discussion***

The proposed Wishart Chernoff distance is used in an agglomerative clustering approach for the unsupervised segmentation of the available ALOS polarimetric SAR data. In order to reduce speckle noise, Lee's polarimetric SAR speckle filter (Lee et al., 1999b), which uses a multiplicative noise model and  $7 \times 7$  directional windows, was applied on the initial polarimetric SAR image. The application of the Lee speckle filter does not interfere with the estimation of the similarity between clusters.

The proposed unsupervised segmentation approach using the Wishart Chernoff distance is applied to the L-band ALOS polarimetric SAR data acquired in UK. In this case study, the initial division of the data based on the SPAN/HA/ $\alpha$  produces 40 clusters. The appropriate number of classes is calculated based on the data log-likelihood algorithm. As discussed in Tibshirani et al. (2001), as  $m$  decreases the data log-likelihood initially flattens until a certain point, called "elbow", from which the data log-likelihood monotonically decreases. This point indicates that the appropriate number of clusters has been reached. Figure 5.2a gives the data log-likelihood, if the Wishart Chernoff distance is used to merge clusters.



(a)



(b)

**Figure 5.2:** a) Plot of the data log-likelihood calculated using the Wishart Chernoff distance to merge clusters, b) Plot of the data log-likelihood calculated using the Wishart test statistic distance to merge clusters.

As shown in Figure 5.2a, the point in the graph where the flattening stops and the decreasing starts is found for  $m = 18$ , which corresponds to the appropriate number of classes.

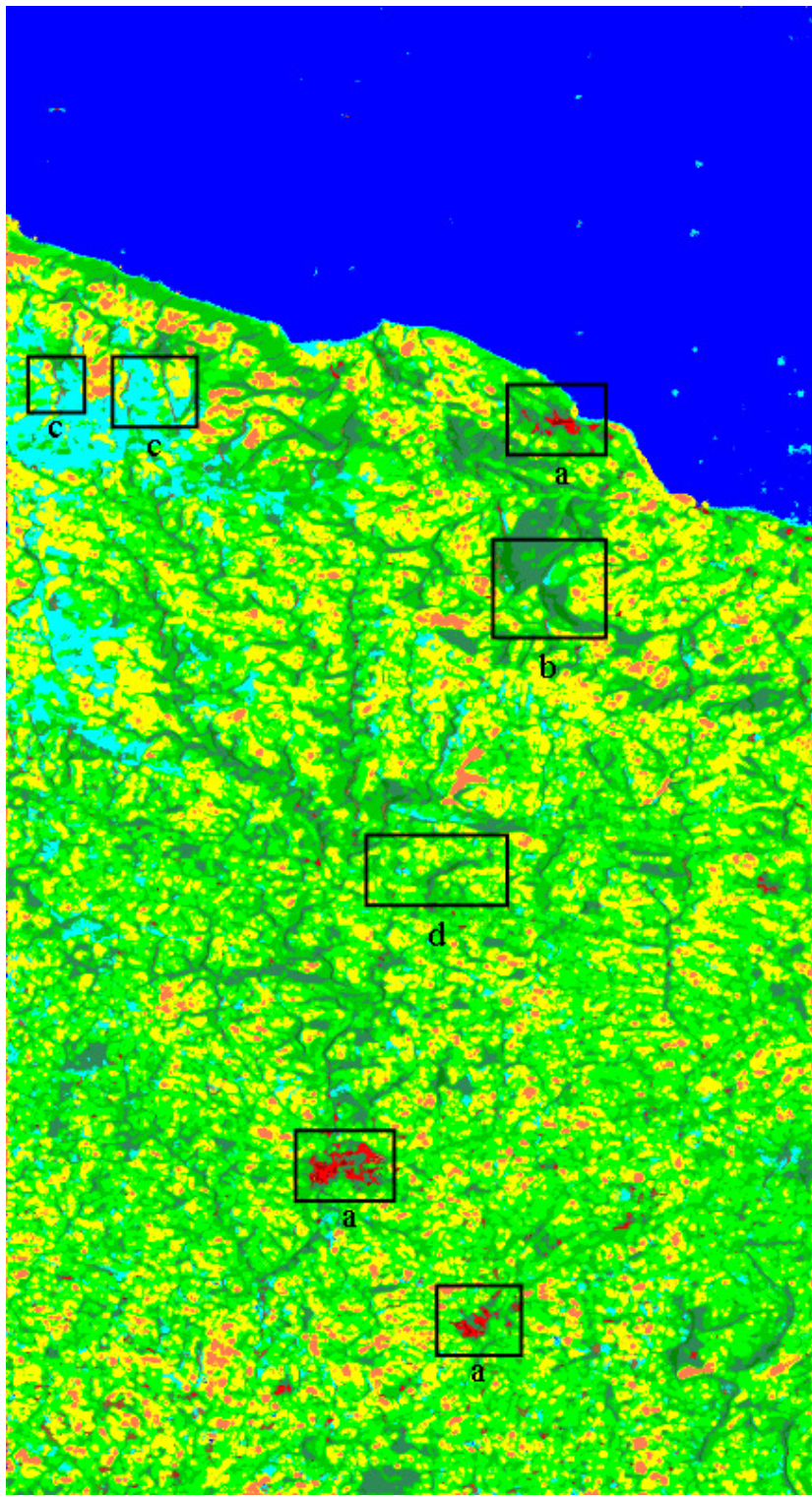
For comparison, the same initial clusters produced based on the SPAN/H/A/ $\alpha$  are used as input data for a segmentation using the Wishart test statistic distance (Cao et al., 2007)

$$d(V_1, V_2) = (N_1 + N_2) \ln|V| - N_1 \ln|V_1| - N_2 \ln|V_2|, \quad (5-21)$$

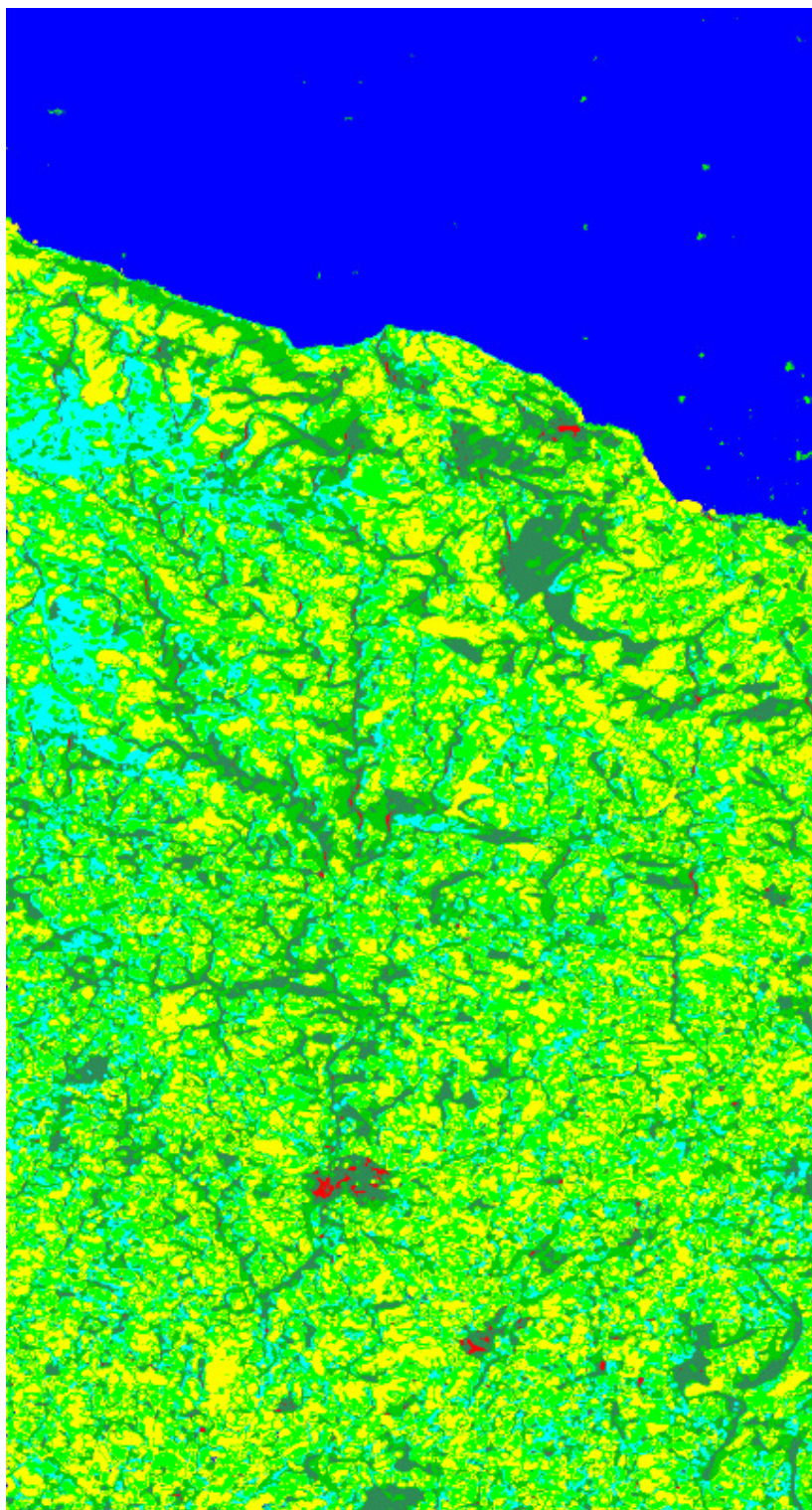
where  $V = \left( \sum_{l=1}^{N_1+N_2} T_l \right) / (N_1 + N_2)$ . The appropriate number of classes is calculated based on the data log-likelihood algorithm and using the Wishart test statistic distance as a criterion for cluster merging. The data log-likelihood results are shown in Figure 5.2b. Here, the appropriate number of classes is determined as  $m = 8$ .

Although the data log-likelihood algorithm depends on the number of clusters  $m$ , the used distance criterion plays an important role in the estimated appropriate number of clusters. In the case of Wishart Chernoff distance, the estimated number of classes is much higher than the estimated number based on the Wishart test statistic distance. This is because the Wishart Chernoff distance is independent of the number of samples in the clusters. This has the advantage of preserving detailed information which corresponds to small discriminated thematic land cover types, e.g., small separate farm houses would still be preserved, although it has fewer samples, so it will not be clustered as no other buildings lie around.

As shown in Figure 5.3a, the segmentation results based on the Wishart Chernoff distance produce compact noiseless classes. From Figure 5.3a, different regions are selected and classes are compared with classes resulting from the unsupervised segmentation based on the Wishart test statistic distance (Figure 5.3b). Furthermore, the resulting classes from the two methods are compared with the corresponding surface types apparent in the study area.



(a)



(b)

**Figure 5.3:** a) POLSAR data classification based on the Wishart Chernoff distance,  
b) POLSAR data classification based on the Wishart test statistic distance.

Comparing the segmentation results based on the Wishart Chernoff distance and the Wishart test statistic distance with map of the study area, more classes can be seen in the high-energy returns associated with urban and forest areas for the case of Wishart Chernoff distance. Two main classes are obtained for the urban areas based on the Wishart Chernoff distance, as shown in Figure 5.4a2. On the other hand, one class is obtained based on the Wishart test statistic distance (Figure 5.4a3). Comparing the two results with the urban blocks in the map (Figure 5.4a1), it is obvious that urban areas are better captured using the Wishart Chernoff distance.

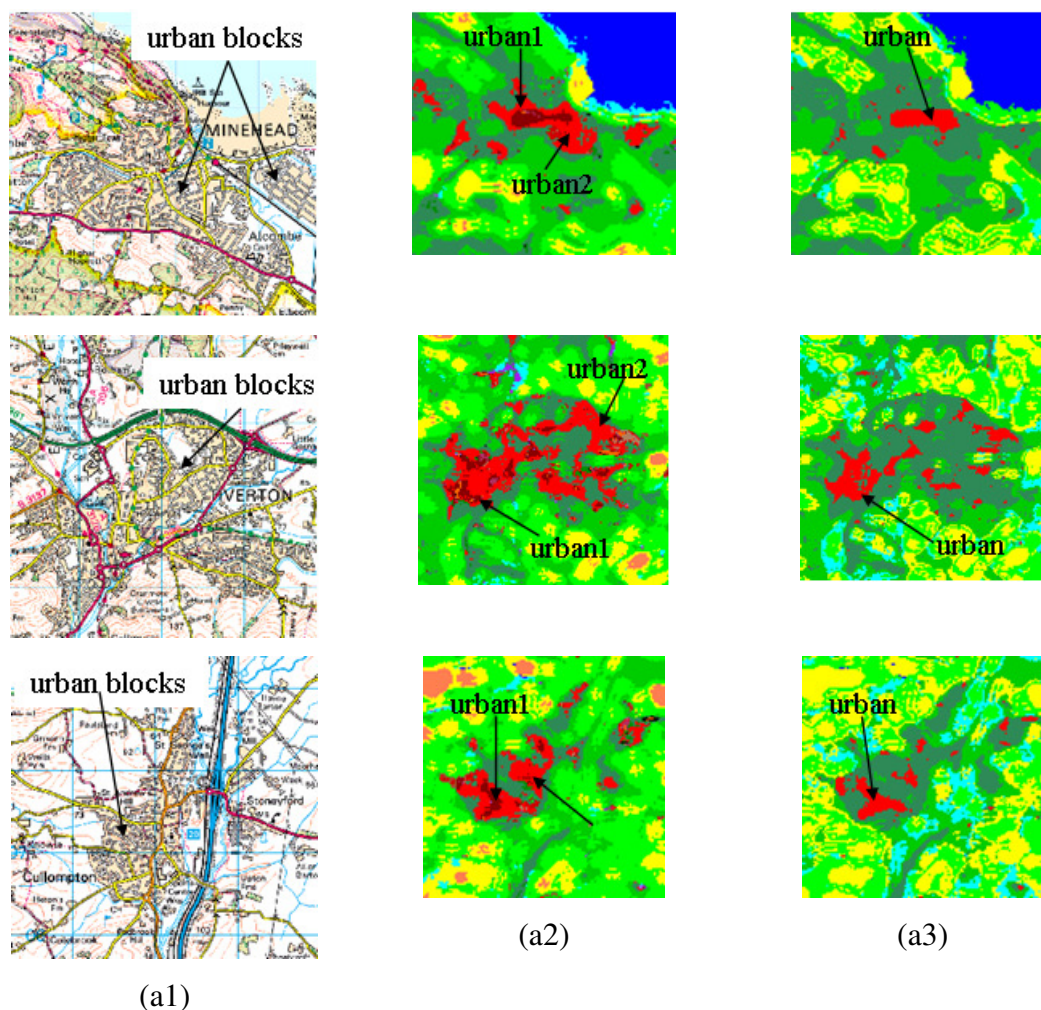
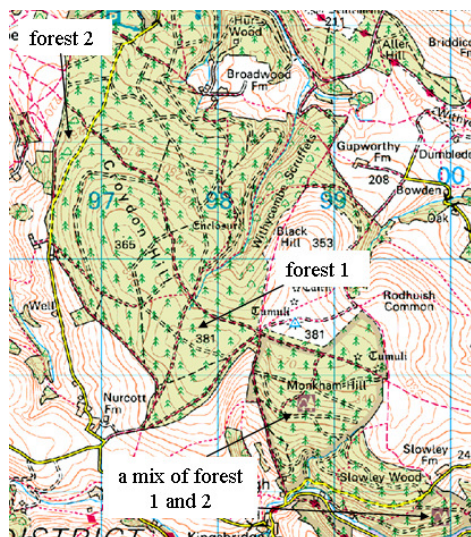


**Figure 5.4:** a1) Urban blocks as shown in a map of the study area, a2) Urban areas captured based on Wishart Chernoff distance, a3) Urban areas captured based on Wishart test statistic distance.

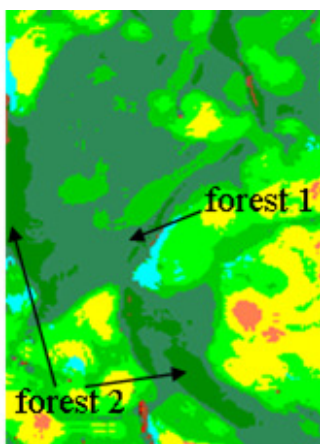
Two classes (dark green and sea green) which correspond to forest areas are identified in the segmentation based on the Wishart Chernoff distance, Figure 5.5b3. This agrees with the fact that two forest types exist in the study area, Figure 5.5b1 and b2. Only one forest class is obtained based on the Wishart test statistic distance, Figure 5.5b4.



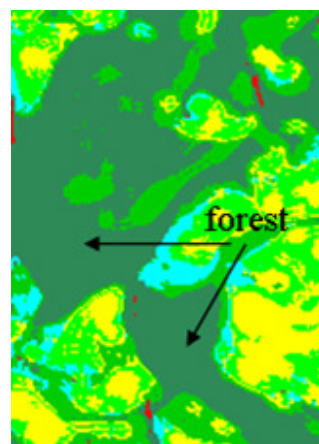
(b1)



(b2)



(b3)



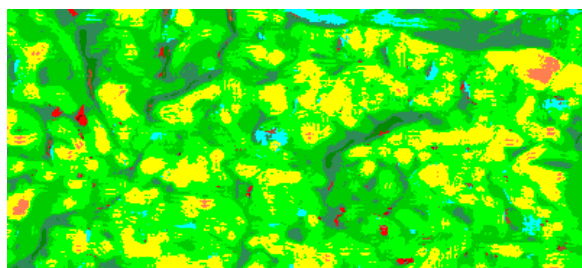
(b4)

**Figure 5.5:** b1) Forests as shown in the map of the study area, b2) Forests as appear in the AVNIR-2 optical image of the study area, b3) Forest areas captured based on the Wishart Chernoff distance, b4) Forest areas captured based on the Wishart test statistic distance.

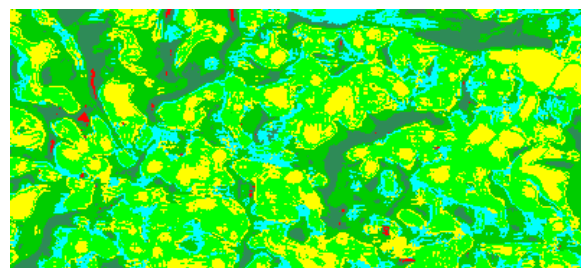
The study area contains various agricultural fields and cropland with different types of crops. Assigning the resulting classes to thematic types of crops was not possible for two reasons. First, agricultural fields and croplands are not mapped in the available study area map. Second, the optical image of the study area was taken one year before the polarimetric data collection, Figure 5.6c1. Thus, the comparison is not reasonable because the type of crops might have changed. Four main classes (yellow, orange, light green and green) correspond to agricultural fields and croplands are obtained using the Wishart Chernoff distance, Figure 5.6c2. Using the Wishart test statistic distance, three classes (yellow, light green and green) are extracted, Figure 5.6c3. Different areas are misclassified as natural grassland (cyan), Figure 5.6c3. These areas appear as noise with approximately linear shapes.



(c1)



(c2)



(c3)

**Figure 5.6: c1) Optical image of the study area for reference, c2) Classified agricultural fields and croplands using Wishart Chernoff distance, c3) Classified agricultural fields and croplands using Wishart test statistic distance.**

A small class (brown) which corresponds to streams in the study area (Figure 5.7d1) is extracted using the Wishart Chernoff distance, Figure 5.7d2. However, streams are misclassified as forest and urban areas using the Wishart test statistic distance, Figure 5.7d3. The results obtained from the Wishart test statistic distance suggest that rivers are covered by trees and canopy as they are classified as forest. However, our method shows that this argument, while reasonable in principle, is not valid as the rivers are detectable using the Wishart Chernoff distance clustering. This is another argument for not using the number of samples in a class as a parameter in the clustering method (as used in Wishart test statistic distance), as it can lead to loss of significant information.

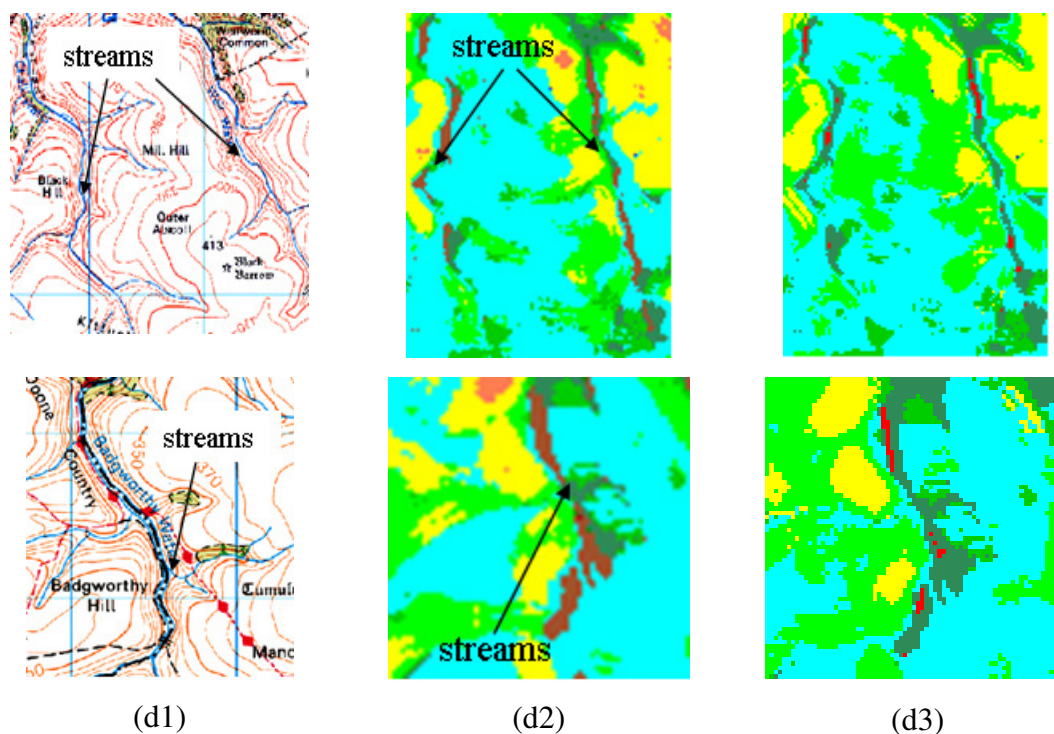


**Figure 5.7:** d1) Streams as shown in the map of the study area, d2) Streams captured based on the Wishart Chernoff distance, d3) Streams captured based on the Wishart test statistic distance.

Classifying POLSAR data into eight classes based on the Wishart Chernoff distance produces classification results where the main information is preserved, some detailed information is lost, e.g., streams and parts of the urban areas. Even noisier

classification results are obtained when the POLSAR data are classified based on the Wishart test statistic into eighteen classes.

An accuracy assessment of the performance of the two classification algorithms can be performed using test samples. These test samples can be selected for the main surface types by labeling pixels of the polarimetric SAR data using the available optical image and map of the study area as a guide. Thus, test samples for ocean, two types of forest, natural grassland, and urban areas are chosen. The percentage of the classification error for the selected test samples is calculated for each classification (Kersten et al., 2005). Table 5.1 presents the relative classification errors for the Wishart Chernoff distance and the Wishart test statistic distance.

	<b>Number of pixels</b>	<b>Error in % for Wishart Chernoff distance</b>	<b>Error in % for Wishart test statistic distance</b>
<b>Ocean</b>	983	0	0
<b>Urban</b>	680	47.25	83.93
<b>Forest1</b>	515	7.25	0
<b>Forest2</b>	316	3.80	100
<b>Natural grassland</b>	515	0	1.75

**Table 5.1: Error in classification in percent for selected land cover regions of the POLSAR image.**

The classification error for both methods on the ocean is zero. The classification error of the urban areas is significantly higher using the Wishart test statistic distance, in comparison to the Wishart Chernoff distance. The Wishart test statistic distance appears to have better classification results (zero classification error) than the Wishart Chernoff distance (7.25% classification error) for the first forest type (forest1). However, this is not true because in the case of Wishart test statistic distance the two types of the forest are merged in one class. This is why the classification error for the second forest type (forest2) is 100% in the case of Wishart test statistic distance. The overall classification

accuracy using the Wishart Chernoff distance is 82.6%, while for the case of Wishart test statistic distance is 54.6%.

#### 5.4 Application to RADARSAT-2 Full Polarimetric SAR Images

Segmentation using the proposed Wishart Chernoff distance was also performed using six RADARSAT-2 full polarimetric SAR images of Churchill, Manitoba, Hudson Bay. The six images were taken every two months for one full year starting October 31, 2009. Table 5.2 reports the calculated appropriate number of classes, obtained using the log-likelihood algorithm for each image.

<b>Image (Churchill_YYYYMMDD)</b>	<b>Number of classes</b>	<b>Temperature (C°)</b>	<b>Weather condition during acquisition day</b>
Churchill_20091031	6	-6.2	snow
Churchill_20091218	7	-21.5	6 hours snow
Churchill_20100124	11	-14.0	12 hours snow
Churchill_20100403	10	-5.9	14 hours snow
Churchill_20100521	7	-1.5	10 hours snow + 5 hours freezing rain
Churchill_20100722	8	16.3	-

**Table 5.2: Number of classes, temperature and weather condition for each RADARSAT-2 image and acquisition time. Data source for temperature and weather condition data is the National Climate Data and Information Archive of Canada.**

A plot indicating the change in the number of classes against the acquisition date of each image is presented in Figure 5.8.

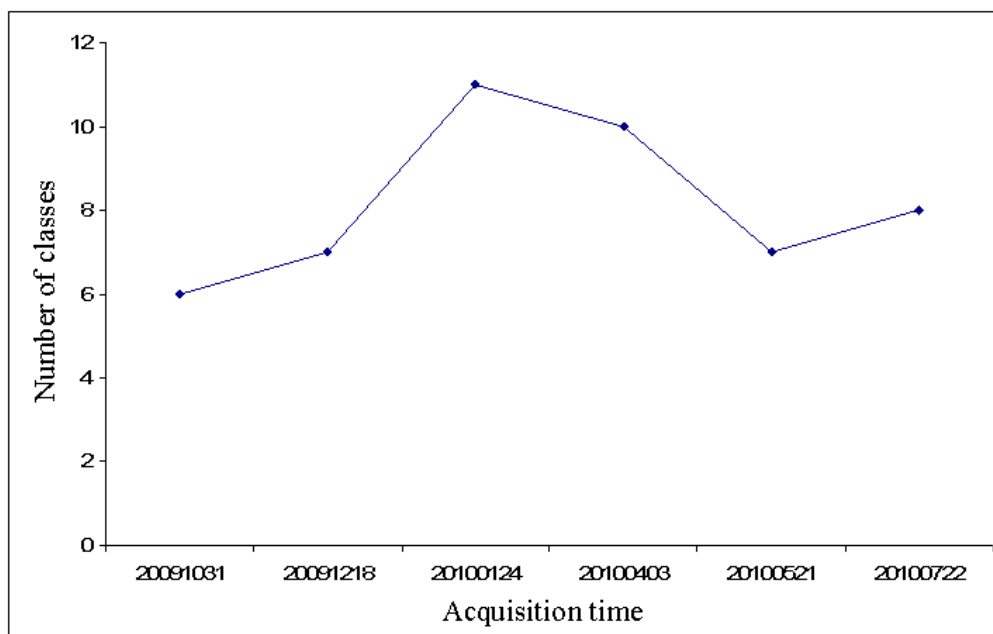
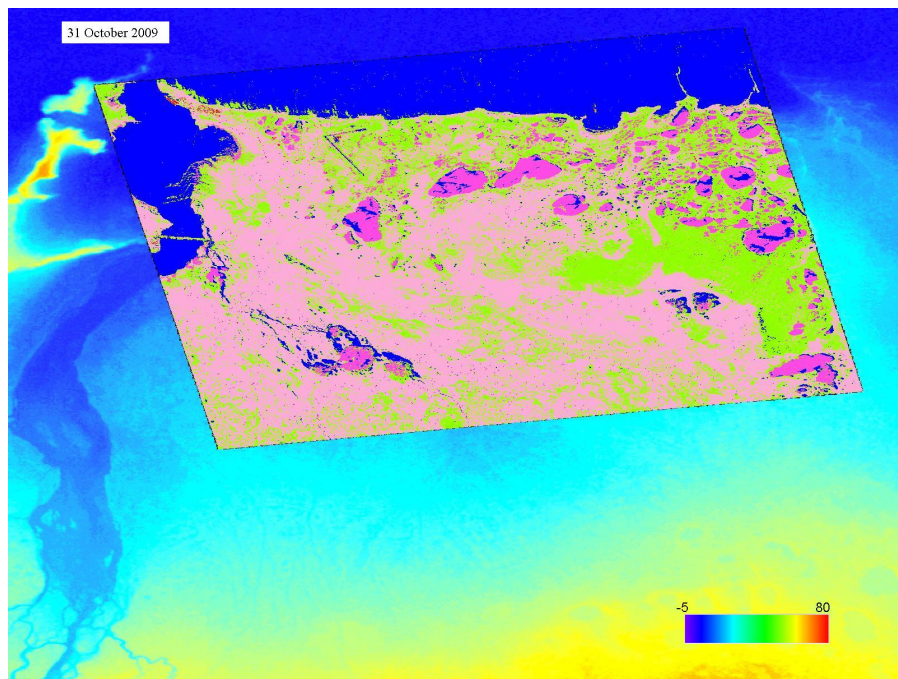
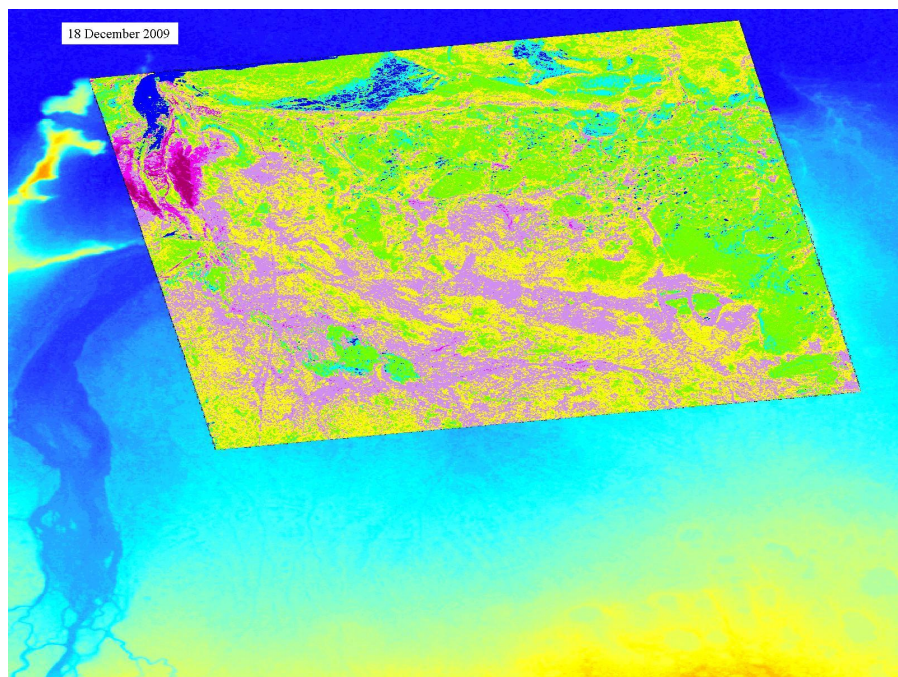


**Figure 5.8: Plot of the number of classes as a function of the acquisition time for each SAR image.**

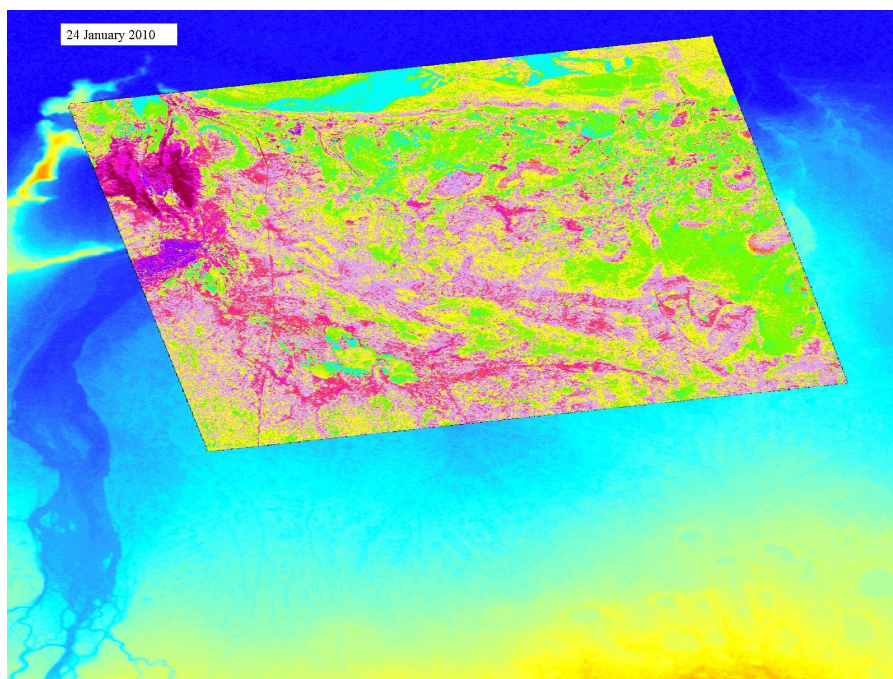
As shown in Figure 5.8, the number of classes for the study area increases through the fall season and reaches its maximum value in January (winter). The number of classes decreases from January to May (spring). From May to July (summer) the number of classes increases by one class. Segmentation results for the six images plotted over a Shuttle Radar Topographic Mission (SRTM) DEM with a resolution of 90 meters are presented in Figure 5.9.



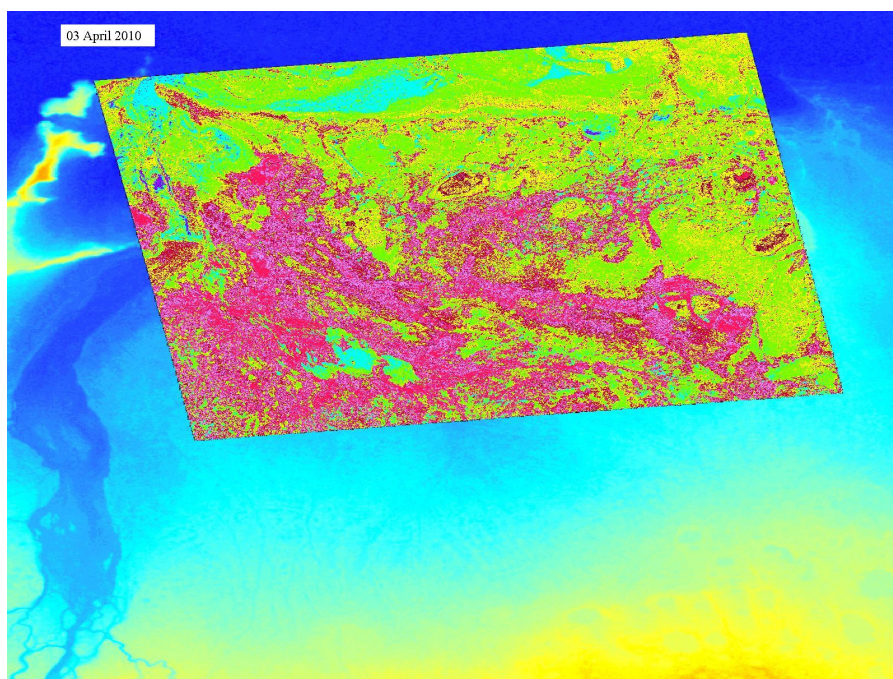
(a)



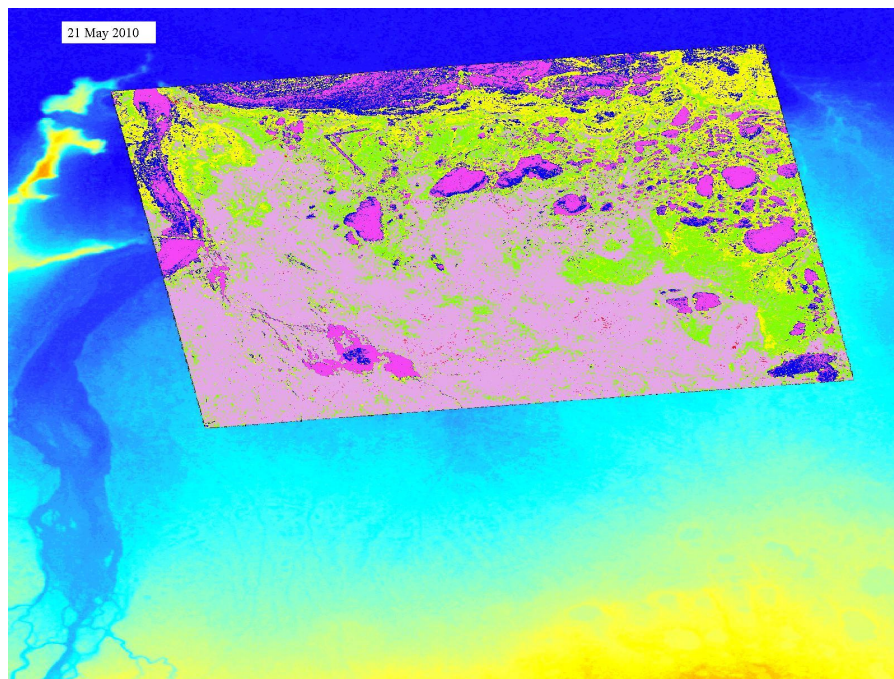
(b)



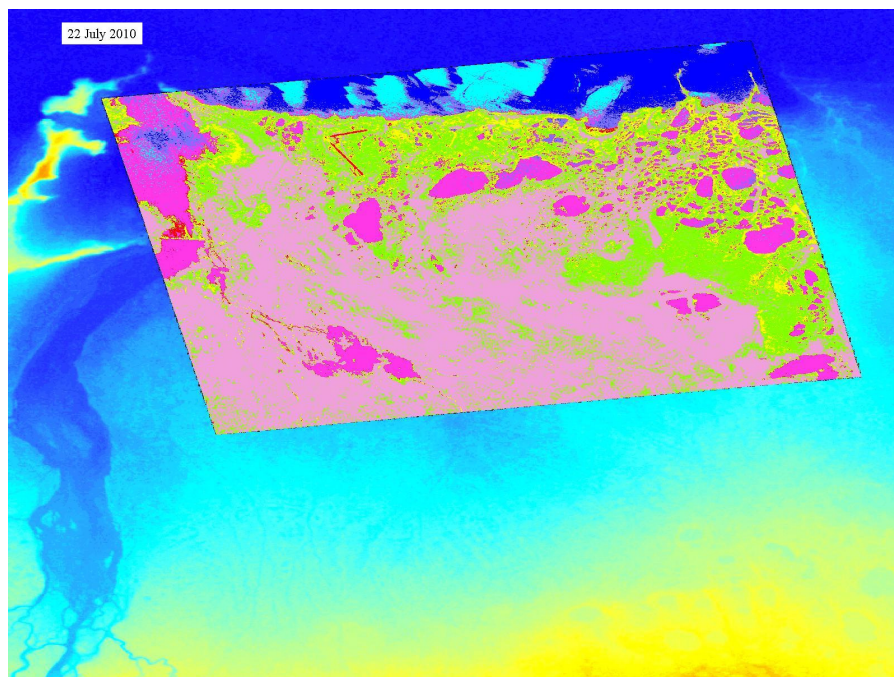
(c)



(d)



(e)



(f)

**Figure 5.9: Segmentation results on top the SRTM 90m DEM of the Churchill area for the RADARSAT-2 images of: a) October 31, 2009, b) December 18, 2009, c) January 24, 2010, d) April 3, 2010, e) May 21, 2010 and July 22, 2010.**

The study area undergoes significant seasonal changes in land cover as the dominant climate controls both vegetation and snow/ice conditions. Churchill is especially of interest as the transition between boreal forest and arctic tundra can be observed. In addition, sea ice cover, lakes and lake ice, the Churchill River, the town of Churchill and the airport, rock outcrops, muskeg and wetlands can be found. Hence, the area is prone to significant change in land cover which this case study is aiming to monitor.

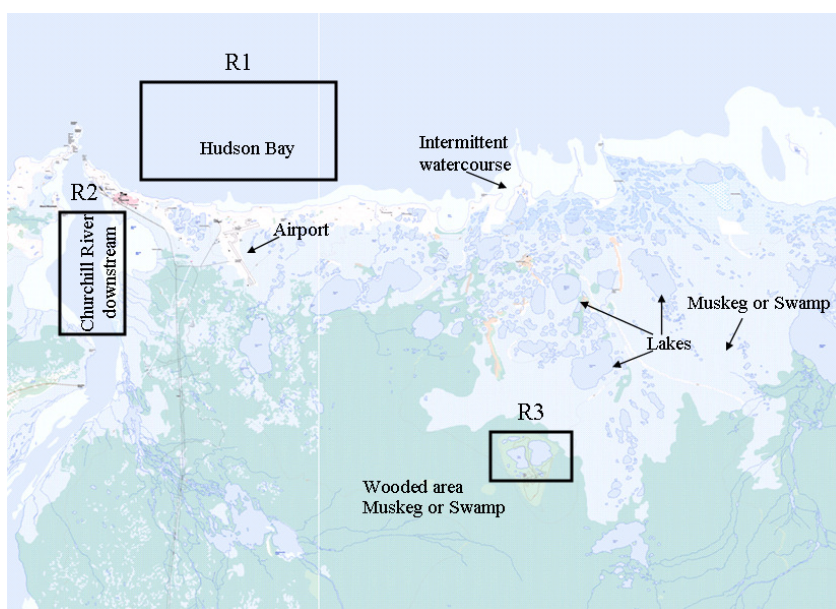
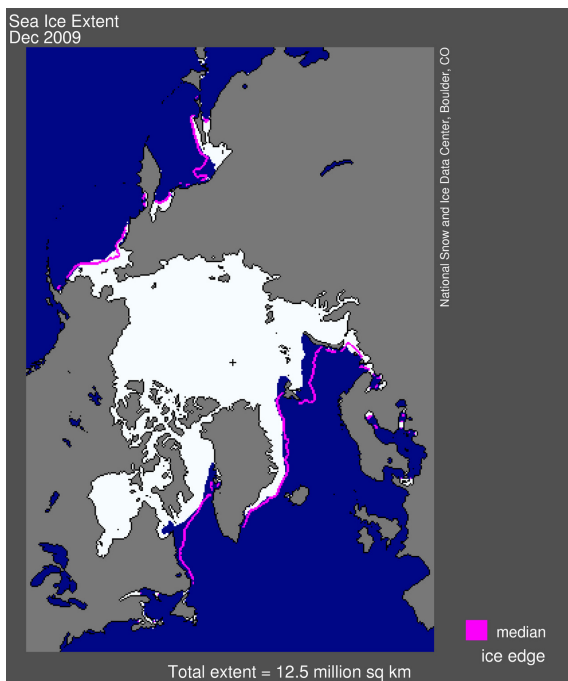
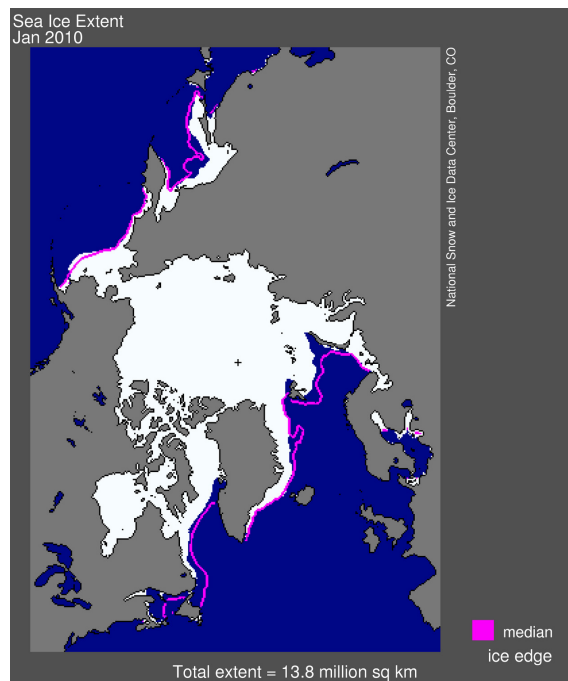


**Figure 5.10: Three selected regions (R1, R2 and R3) in the study area for further investigation.**

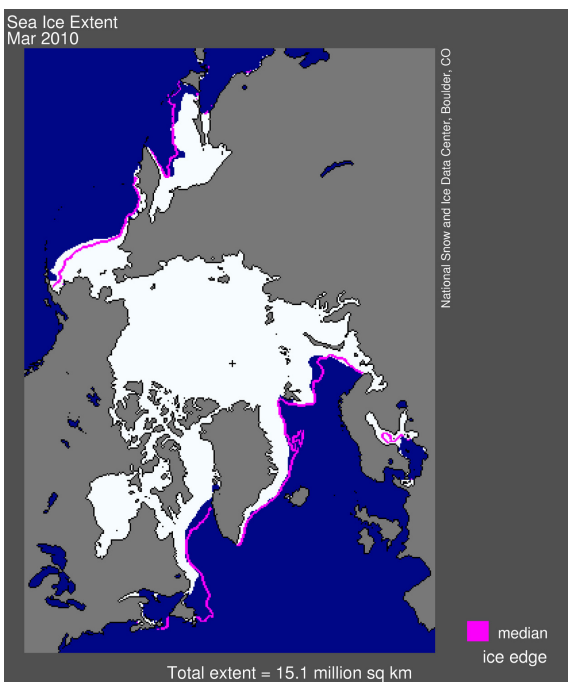
Three regions are selected for the investigation of landscape changes, Figure 5.10. The first region (R1) is selected in Hudson Bay (Figure 5.10). In Oct. 2009, the selected region R1 presents only one class. This class corresponds most probably to water as this time is shortly after the end of the summer season with a temperature of  $-6.2\text{ C}^{\circ}$ . Sea ice formations did not occur yet or the area would be covered by very thin smooth ice.



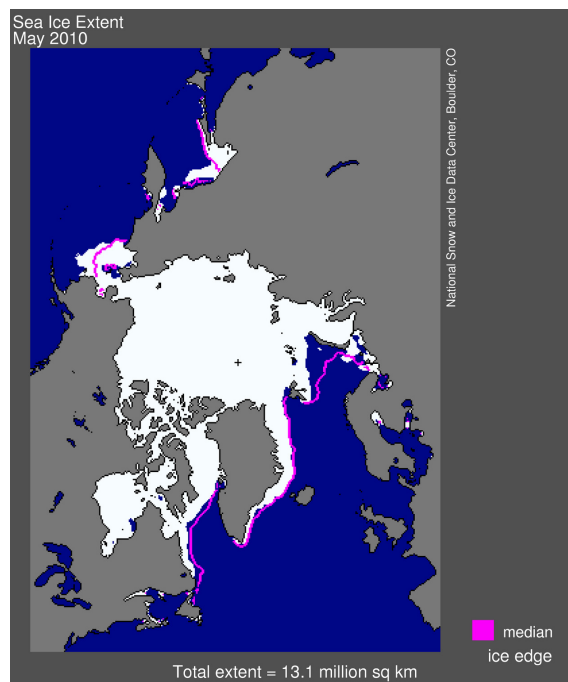
(a)



(b)



(c)



(d)

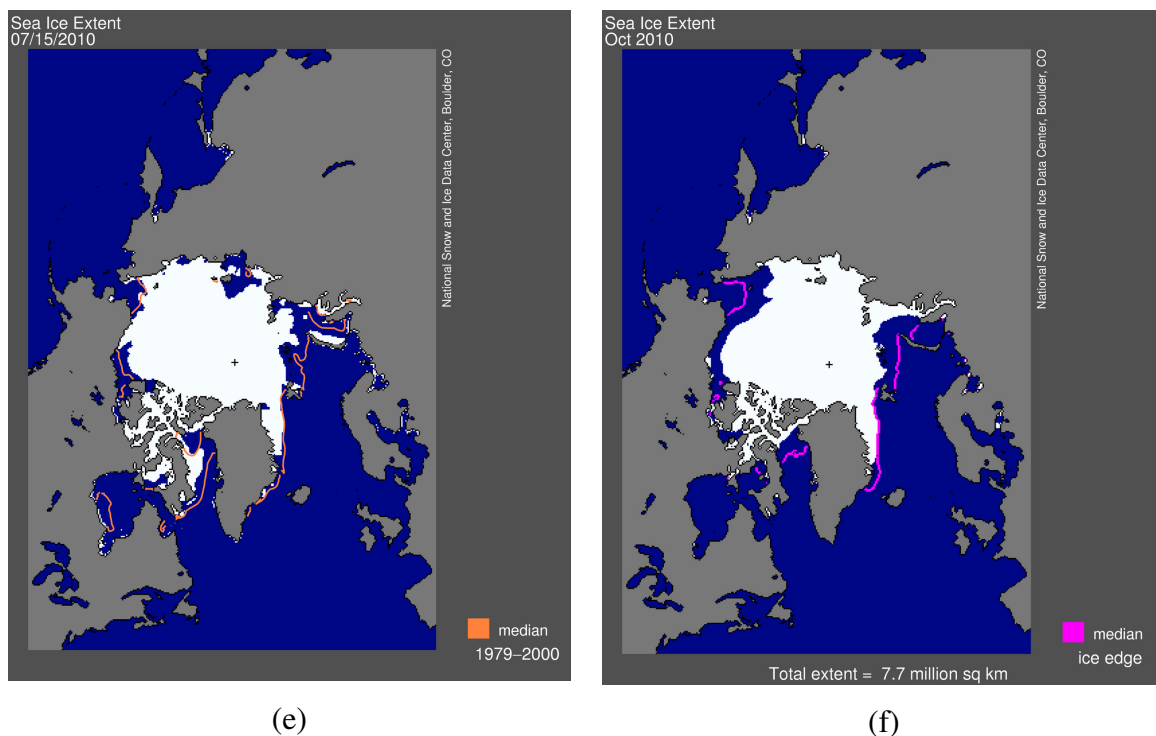


**Figure 5.11: Sea ice extent of the Arctic, including Hudson Bay for: a) December 2009, b) January 2010, c) March 2010, d) May 2010, e) July 2010, and October 2010. Source: National Snow and Ice Data Center (NSIDC).**

Figure 5.11 indicates the sea ice extent of Arctic, including the Hudson Bay, between December 2009 and October 2010. The sea ice extent data times are close to the acquisition times of the RADARSAT-2 SAR data. Figure 5.11f shows that October is a sea ice free month in Hudson Bay. The number of classes increased to four in Dec. 2009, which corresponds to the highest number of classes obtained for the selected area. The acquisition day temperature was the lowest ( $-21.5\text{ C}^{\circ}$ ) among the six temperature measurements. There is still open water in the Churchill River estuary, but also significant areas of sea ice, partially snow covered. The number of classes decreased to three in Jan. 2010, which indicates that the sea ice has formed and changes are not expected at the peak of winter. April still shows a similar picture with two classes and similar sea ice status, but in May the two classes have switched to open water and remaining sea ice fractions. In the summer acquisition of July, the classified SAR image presents three classes in R1 which indicate that there is still sea ice around, but on a

declined level. The temperature of the acquisition day was positive (16.3 C°) and enough to continue melting the ice.

A second region (R2 in Figure 5.10) is selected in the Churchill River downstream from the weir (Figure 5.12a) as seen in Figure 5.9a and e. The selected region R2 presents one class in Oct. 2009 which is open water. The number of classes increases dramatically into six classes in Dec. 2009 and Jan. 2010, where the temperatures are the lowest (-21.5 C° and -14.0 C°, respectively). This could be related to the fact that the Churchill River appears to have moved river ice blocks on top of each other which creates a new surface type indicated by dark pink color. High-energy returns are observed for this region in the SAR images of Dec. 2009 and Jan. 2010. The number of classes decreases to four, four and one main class with three very small classes for Apr. 2010, May 2010 and Jul. 2010, respectively. As with sea ice the time series shows the melting process of river ice.

The third selected region R3 (Figure 5.10) contains the twin lakes of Churchill. The twin lakes present three classes in Oct. 2009. These three classes become two, one main class and another secondary one, in Dec. 2009. In Jan. 2010 and Apr. 2010, these lakes contain three classes. The discrimination of the lakes from the surrounding areas becomes difficult in Jan. 2010. In spring (May 2010), the twin lakes appear to have two classes, one dominant and another secondary one. These two classes become one in summer, Jul. 2010. While the lakes freeze about the same time as the river ice forms, the identification of lake ice is difficult as it is covered by snow throughout the winter. As the lake ice melts in summer, open water can be seen (Figure 5.9e). When the growing season starts, muskeg covers most of the water surfaces and creates one class. Figure 5.12b and c indicates muskeg covered and partially overgrown lakes in Churchill.

It is obvious that full polarimetric SAR data can detect and monitor landscape changes; however, it is not trivial to identify the surface type based on the classification without additional knowledge of climate and landscape processes. The fusion of the SAR data with data such as DEMs, temperature measurements, snow depths, etc., could be useful in analyzing and explaining the resulting classes in more detail. Future research must be directed to achieve this goal.



(a)



(b)



(c)

**Figure 5.12: Pictures of Churchill show: a) Churchill River weir, b) Muskeg covered lake, c) Partially overgrown lake.**

Another potential application is the identification of permafrost and degraded permafrost or active layers. The classification may be sufficiently accurate to separate frozen and water filled soil, but this application cannot be achieved without having accurate ground data for validation of the classification.

## 5.5 Summary

In this chapter, a new probabilistic distance, the Wishart Chernoff distance, based on the probability densities of the complex Wishart distribution, is derived. The Wishart Chernoff distance is always non-negative, with zero distance occurring only if the

probability distributions are identical. An unsupervised agglomerative approach for ALOS PALSAR data segmentation is discussed. Data are divided into clusters based on the SPAN/H/A/ $\alpha$  space. The Wishart Chernoff distance is used to merge clusters hierarchically into an appropriate number of classes, which is calculated using the data log-likelihood algorithm. Although the data log-likelihood algorithm estimates the appropriate number of classes taking into account the inner data structure, the obtained appropriate number differs according to the distance criterion used to merge the clusters. The Wishart Chernoff distance tends to provide a higher number of classes than the Wishart test statistic distance, preserving more detailed information of the polarimetric SAR data, which corresponds to more detailed land cover types. This is mainly because the Wishart Chernoff distance, in comparison with the Wishart test statistic distance, uses the statistical characteristics of the two Wishart distributions in order to estimate their similarity. Moreover, the fact that the Wishart Chernoff distance is independent of the number of samples makes it a much more robust distance criterion. Promising segmentation results are obtained using the Wishart Chernoff distance, including details as well as uniform areas and a relative large number of classes. Thus, the proposed Wishart Chernoff distance can be applied when detailed information is required.

## Chapter Six: Conclusions and Future Perspectives

### 6.1 Conclusions

The main purpose of this research was the development of new segmentation methodologies for polarimetric SAR data which overcome some of the limitations of contemporary methods. To achieve this, we have developed new segmentation methodologies which can be grouped into: 1) methodologies using a divisive clustering technique and 2) methodologies using an agglomerative clustering technique.

For the divisive case, two new segmentation approaches were discussed for full and dual polarimetric SAR data. In order to overcome the drawbacks of already existing divisive segmentation approaches, both divisive approaches were nonparametric, i.e., assumptions about the underlying distributions were avoided. This was accomplished by involving a nonparametric histogram thresholding algorithm in both segmentation approaches. This algorithm has the advantage of being able to automatically determine the number of modes in a histogram. The proposed segmentation methodology for the full polarimetric case was applied to the analysis images of Pauli and Freeman-Durden, in separate cases. Segmentation started by dividing the input data based on the dominant and the second most significant scattering mechanisms in the first and second segmentation levels, respectively. Afterwards, the nonparametric histogram thresholding algorithm was applied on the histograms of the dominant scattering mechanism for further segmentation, exploiting the inherent variations within the dominant scattering mechanism. Scattering information alone was found not sufficient to split data into segments that correlate well with the different RGB colors. Hence, amplitude information of the dominant scattering mechanism was necessary to obtain the required segmentation. The proposed segmentation methodology goes beyond the existing methodologies from two points of view. Firstly, the resulting segments are homogeneous with regard to the amplitude values of the dominant scattering mechanism. Secondly, these segments preserve the polarimetric scattering information. Preserving the scattering mechanism information is very important as this information exploits the advantage that full

polarimetric SAR systems provide, in comparison to single-channel SAR or optical systems. This additional polarimetric information can also be used in a later classification approach of segments into semantic objects. The performance of the proposed methodology was tested against segmentation results from the k-means algorithm. Segments of our methodology were compared with the resulting segments based on the Wishart k-means  $H/\alpha$  and Wishart k-means  $H/\alpha/A/SPAN$ . It was clear that our methodology attains better segmentation results in terms of 1) smooth segment boundaries that nicely fit the RGB composite color variations and 2) non over-segmenting the polarimetric SAR data. It was shown that fewer numbers of segments are obtained in comparison to the numbers obtained by the Wishart k-means  $H/\alpha$  and Wishart k-means  $H/\alpha/A/SPAN$  approaches. The proposed methodology for the dual polarized case uses the nonparametric histogram thresholding algorithm to divide the two histograms of the two SAR channels into unimodal regions. Next, the information of the two channels were used together in order to produce image segments. In this context, the two thresholded histograms were combined together to form a two dimensional histogram-based space divided into subspaces responsible for the segmentation. As in the full polarimetric case, the proposed methodology for dual polarized data segmentation was multilevel. Two criteria were defined, one based on the number of pixels which belong to a subspace and another one based on the standard deviation of these pixels. Both were intended to control the subsequent segmentation levels. These two criteria were successfully able to select those subspaces which need to be considered in the next segmentation levels. This was clear from the final resulting segments, where different variations of the grayscale color were well outlined. The comparison of the concept of the proposed methodology with the segmentation concept implemented by the *eCognition* segmentation algorithm revealed an important feature. As the proposed segmentation approach creates segments of various sizes, it allows for segmentation of small or large regions without discriminating the number of pixels in a region. This feature is a result of using segmentation based on the defined subspaces in each previous segmentation level. Thus, small size segments were found to be contained within large contiguous ones. This was not the case with the *eCognition* segmentation algorithm, which is image-based and

which acts locally, producing contiguous segments only. The difference in the two concepts leads to topological relationships in different spaces. In our case, the mother-child topological relationships were formed in the two dimensional histogram-based space while for the *e*Cognition case, these relationships were formed in the two dimensional space of the image.

For the agglomerative segmentation, a new methodology for the unsupervised segmentation of full polarimetric SAR data was presented. The proposed methodology is new in terms of proposing a new probabilistic distance as a similarity criterion for merging clusters. Concerning the drawbacks of the existing criteria, we proposed a new criterion independent of the number of samples (pixels) in each cluster which evaluates the similarity of clusters by measuring the Chernoff distance between their complex Wishart probability density functions. The Wishart Chernoff distance is always positive symmetric. Two identical distributions have a zero Wishart Chernoff distance. The robustness of the Wishart Chernoff distance results from its independence of the polarization basis which was mathematically proven. In this context, data in covariance matrices, coherency matrices or circular polarization matrices would produce identical segmentation results. In an agglomerative clustering approach, the estimation of the appropriate number of clusters using the data log-likelihood algorithm differs depending on the distance criterion used in the algorithm. In particular, the Wishart Chernoff distance tends to provide higher appropriate number of clusters than the Wishart test statistic distance. This is because the Wishart Chernoff distance preserves detailed data information which corresponds to small classes, e.g., streams in our case study. Moreover, the Wishart Chernoff distance provides more classes in areas with high-energy returns, e.g., forests and urban areas. The Wishart Chernoff distance was further investigated for landscape dynamics monitoring through the agglomerative clustering of a series of full polarimetric SAR data of Churchill, Manitoba. Changes in land cover surface types were successfully determined. The fusion of the classified radar images with data, such as elevations, temperatures, etc., could help in better understanding landscape dynamics.

## 6.2 Future Perspectives

Assessing the results of this research has shown that useful improvements in POLSAR segmentation have been made. Comparisons with contemporary methods were positive. Several lines of future work can be identified. The segmentation results can be directly used as input data for classifying segments into semantic thematic objects. It is important for the classification approach that transferring segments into thematic classes to exploit the advantages of the previously applied segmentation methodologies, e.g., maintaining the scattering information. Subject of future work could also be a comparison study of the proposed Wishart Chernoff distance with other distances, such as Manhattan distance and the Bartlett distance. Interesting would be to point out the effect of each distance on the calculated appropriate number of clusters using the data log-likelihood algorithm. Further investigation to extend the Wishart Chernoff distance to be applicable to dual polarized case is also necessary in light of having much more dual polarized data available even in the new polarimetric SAR missions, e.g., TanDEM-X. Based on the findings in this study, any information about the targets should be included in the segmentation algorithm. Consequently, an optimal segmentation algorithm for particular applications must ultimately be based on a target oriented method. Future methods should therefore strive to include target area information which is not directly accessible from POLSAR, e.g., DEM, slope, soil moisture, surface temperature, or rock type. More research is still needed in the field of radar data fusion with landscape and physical parameters of terrain. This can lead to valuable information about the mechanisms of the landscape dynamics and the effects of the climate change and shed light on the driving forces of dynamic changes.

## References

- AGARWAL, P., ALAM, A. & BISWAS, R. 2010. Analysing the agglomerative hierarchical clustering algorithm for categorical Attributes. *International journal of innovation, management and technology*, 1, 186-190.
- ALBERGA, V. 2004. *Comparison of polarimetric methods in image classification and SAR interferometry applications*. PhD, Technical University of Chemnitz.
- ANFINSEN, S. N., DOULGERIS, A. P. & ELTOFT, T. Estimation of the Equivalent Number of Looks in Polarimetric SAR Imagery. Geoscience and Remote Sensing Symposium, 2008. IGARSS 2008. IEEE International, 2008. IV - 487-IV - 490.
- BAATZ, M. & SCHÄPE, A. 2000. Multiresolution Segmentation: an optimization approach for high quality multiscale image segmentation. *Strobl, J., Blaschke, T., Griesebner, G. (Eds.), applied geographic data processing XII. Wichmann-Verlag, Heidelberg*.
- BEAULIEU, J. M. & TOUZI, R. Hierarchical segmentation of polarimetric SAR images. Geoscience and Remote Sensing Symposium, 2002. IGARSS '02. 2002 IEEE International, 2002. 2590-2592 vol.5.
- BEAULIEU, J. M. & TOUZI, R. 2004. Segmentation of textured polarimetric SAR scenes by likelihood approximation. *Geoscience and Remote Sensing, IEEE Transactions on*, 42, 2063-2072.
- BOERNER, W. M., EL-ARINI, M., CHUNG-YEE, C. & MASTORIS, P. 1981. Polarization dependence in electromagnetic inverse problems. *Antennas and Propagation, IEEE Transactions on*, 29, 262-271.
- CAMERON, W. L., YOUSSEF, N. N. & LEUNG, L. K. 1996. Simulated polarimetric signatures of primitive geometrical shapes. *Geoscience and Remote Sensing, IEEE Transactions on*, 34, 793-803.
- CAO, F., WEN, H., YIRONG, W. & POTTIER, E. 2007. An Unsupervised Segmentation With an Adaptive Number of Clusters Using the SPAN/H/ $\alpha$ /A Space and the Complex Wishart Clustering for Fully Polarimetric SAR Data Analysis. *Geoscience and Remote Sensing, IEEE Transactions on*, 45, 3454-3467.
- CLOUDE, S. R., HAJNSEK, I. & PAPATHANASSIOU, K. 1999. Eigenvectors methods for the extractions of surface parameters in polarimetric SAR. *The Committee Earth observing satellite (CEOS), SAR workshop*. Toulouse, France: Paris: European Space Agency.
- CLOUDE, S. R. & POTTIER, E. 1996. A review of target decomposition theorems in radar polarimetry. *Geoscience and Remote Sensing, IEEE Transactions on*, 34, 498-518.
- CLOUDE, S. R. & POTTIER, E. 1997. An entropy based classification scheme for land application of polarimetric SAR. *Geoscience and Remote Sensing, IEEE Transactions on*, 35, 68-78.
- DABBOOR, M. & KARATHANASSI, V. 2005. A knowledge-based classification method for polarimetric SAR data. *SPIE Europe international symposium in remote sensing*. Brussels, Belgium: Society of photo-optical instrumentation engineers.

- DABBOOR, M., KARATHANASSI, V. & BRAUN, A. 2008. Histogram-based segmentation of ALOS polarimetric SAR data. *The 3<sup>rd</sup> ALOS PI symposium*. Rhodes, Greece: ESA SP-664.
- DABBOOR, M., KARATHANASSI, V. & BRAUN, A. 2010a. Multilevel hierarchical segmentation method for polarimetric SAR data based on scattering behaviour and histograms. *Canadian journal of remote sensing*, 36, 142-153.
- DABBOOR, M., KARATHANASSI, V. & BRAUN, A. 2010b. A multilevel segmentation methodology for dual-polarized SAR data. *International journal of applied Earth observation and geoinformation*, (submitted).
- DABBOOR, M., KARATHANASSI, V., BRAUN, A. & COLLINS, M. 2010c. An unsupervised classification approach for polarimetric SAR data based on the Chernoff distance for complex Wishart distribution. *Geoscience and Remote Sensing, IEEE Transactions on*, (in preparation).
- DE GRANDI, G., HOEKMAN, D., LEE, J. S., SCHULER, D. & AINSWORTH, T. A wavelet multiresolution technique for polarimetric texture analysis and segmentation of SAR images. *Geoscience and Remote Sensing Symposium, 2004. IGARSS '04. Proceedings. 2004 IEEE International, 2004.* 713.
- DE GRANDI, G. F., LEE, J. S., SIQUEIRA, R., BARALDI, A. & SIMARD, M. Segmentation and labeling of polarimetric SAR data: can wavelets help? *Geoscience and Remote Sensing Symposium, 2001. IGARSS '01. IEEE 2001 International, 2001.* 410-413 vol.1.
- DELON, J., DESOLNEUX, A., LISANI, J. L. & PETRO, A. B. 2007. A Nonparametric Approach for Histogram Segmentation. *Image Processing, IEEE Transactions on*, 16, 253-261.
- DU, L., GRUNES, M. R. & LEE, J. S. 2002. Unsupervised segmentation of dual-polarization SAR images based on amplitude and texture characteristics. *International Journal of Remote Sensing*, 23, 4383-4402.
- DU, L.-J., LEE, J.-S. & MANGO, S. A. Texture Segmentation of Sar Images Using the Wavelet Transform. *Geoscience and Remote Sensing Symposium, 1992. IGARSS '92. International, 1992.* 1108-1110.
- DUDA, J., HART, P. & STORK, D. 2000. *Pattern classification*, New York, Wiley.
- DUQUENOY, M., OVARLEZ, J. R., MORISSEAU, C., VIEILLARD, G., FERRO-FAMIL, L. & POTTIER, E. Supervised classification by neural networks using polarimetric time-frequency signatures. *Geoscience and Remote Sensing Symposium, 2009 IEEE International, IGARSS 2009, 2009.* IV-438-IV-441.
- EL AYADI, M. M. H., KAMEL, M. S. & KARRAY, F. 2008. Toward a tight upper bound for the error probability of the binary Gaussian classification problem. *Pattern Recognition*, 41, 2120-2132.
- FREEMAN, A. & DURDAN, S. 1998. A three-component scattering model for polarimetric SAR data. *Geoscience and Remote Sensing, IEEE Transactions on*, 36, 963-973.
- GAO, L. & BAN, Y. 2008. Investigating the performance of SAR polarimetric features in land-cover classification. *International society for photogrammetry and remote sensing* Beijing, China: The international archives of the photogrammetry, remote sensing and spatial information science.

- GRAHAM, L. C. 1974. Synthetic interferometer radar for topographic mapping. *Proceedings of the IEEE*, 62, 763-768.
- GRANDJEAN, G., PAILLOU, P., DUBOIS-FERNANDEZ, P., AUGUST-BERNEX, T., BAGHDADI, N. N. & ACHACHE, J. 2001. Subsurface structures detection by combining L-band polarimetric SAR and GPR data: example of the Pyla Dune (France). *Geoscience and Remote Sensing, IEEE Transactions on*, 39, 1245-1258.
- GRENANDER, U. 1981. *Abstract inference*, New York, Wiley.
- HAJNSEK, I. & EINEDER, M. TerraSAR-X: science exploration of polarimetric and interferometric SAR. IEEE international geoscience and remote sensing symposium, 2005 South Korea. 4882 - 4885.
- HARALICK, R. M. & SHAPIRO, L. G. 1985. Image segmentation techniques. *Computer Vision, Graphics, and Image Processing*, 29, 100-132.
- HELLMANN, M. 1999. *Classification of full polarimetric SAR data for cartographic application*. PhD, Technical University Dresden.
- HENG-DA, C. & YING, S. 2000. A hierarchical approach to color image segmentation using homogeneity. *Image Processing, IEEE Transactions on*, 9, 2071-2082.
- HUYNEN, J. 1970. *Phenomenological theory of radar target*. PhD, Delft university of technology.
- KARATHANASSI, V. & DABBOOR, M. 2004. Land cover classification using E-SAR polarimetric data. *The XX International ISPRS Congress "Geo-Imagery Bridging Continents"*. Istanbul, Turkey.
- KENNAUGH, E. 1952. *Polarization properties of radar reflections*. Master, The Ohio state university.
- KERSTEN, P. R., JONG-SEN, L. & AINSWORTH, T. L. 2005. Unsupervised classification of polarimetric synthetic aperture Radar images using fuzzy clustering and EM clustering. *Geoscience and Remote Sensing, IEEE Transactions on*, 43, 519-527.
- KHATRI, C. G. 1966. On certain distribution problems based on positive definite quadratic functions in normal vectors. *The annals of mathematical statistics*, 37, 468-479.
- KONG, J., SWARTZ, A., YUEH, H., NOVAK, L. & SHIN, R. 1988. Identification of terrain cover using the optimal polarimetric classifier. *Journal of <span style="">electromagnetic waves and applications*, 2, 171-194.
- KOURGLI, A., OUARZEDDINE, M., OUKIL, Y. & BELHADJ-AISSA, A. 2010. Land cover identification using polarimetric SAR images. *ISPRS Technical Commission VII - 100 years ISPRS*. Vienna, Austria.
- KROGAGER, E. & CZYZ, Z. H. 1995. Properties of the sphere, diplane, helix decomposition. *The 3<sup>rd</sup> international workshop on radar polarimetry (JIPR-3, 95)*. Nantes, France.
- KWOK, R., HARA, Y., ATKINS, R. G., YUEH, S. H., SHIN, R. T. & KONG, J. A. Application Of Neural Networks To Sea Ice Classification Using Polarimetric SAR Images. Geoscience and Remote Sensing Symposium, 1991. IGARSS '91. Remote Sensing: Global Monitoring for Earth Management., International, 1991. 85-88.

- LAVALLE, M. 2009. *Full and compact polarimetric radar interferometry for vegetation remote sensing*. PhD, University of Rennes I.
- LEE, J.-S. 1981. Speckle analysis and smoothing of synthetic aperture radar images. *Computer Graphics and Image Processing*, 17, 24-32.
- LEE, J.-S., GRUNES, M. R., AINSWORTH, T. L., LI-JEN, D., SCHULER, D. L. & CLOUDE, S. R. 1999a. Unsupervised classification using polarimetric decomposition and the complex Wishart classifier. *Geoscience and Remote Sensing, IEEE Transactions on*, 37, 2249-2258.
- LEE, J.-S., GRUNES, M. R. & DE GRANDI, G. 1999b. Polarimetric SAR speckle filtering and its implication for classification. *Geoscience and Remote Sensing, IEEE Transactions on*, 37, 2363-2373.
- LEE, J.-S., GRUNES, M. R., POTTIER, E. & FERRO-FAMIL, L. 2004. Unsupervised terrain classification preserving polarimetric scattering characteristics. *Geoscience and Remote Sensing, IEEE Transactions on*, 42, 722-731.
- LEE, J.-S. & POTTIER, E. 2009. *Polarimetric radar imaging: from basics to applications*, CRC press.
- LEE, J. S., GRUNES, M. R. & KWOK, R. 1994. Classification of multi-look polarimetric SAR imagery based on complex Wishart distribution. *International Journal of Remote Sensing*, 15, 2299-2311.
- LEE, J. S., GRUNES, M. R. & MANGO, S. A. 1991. Speckle reduction in multipolarization, multifrequency SAR imagery. *Geoscience and Remote Sensing, IEEE Transactions on*, 29, 535-544.
- LEE, J. S., GRUNES, M. R., POTTIER, E. & FERRO-FAMIL, L. Segmentation of polarimetric SAR images. *Geoscience and Remote Sensing Symposium*, 2001. IGARSS '01. IEEE 2001 International, 2001. 414-416 vol.1.
- LIANG, F., QIU, M.-H., WANG, Y.-X., XIANG, Q.-L., YANG, Y.-F. & LIU, K. 2010. A fast divisive clustering algorithm using an improved discrete particle swarm optimizer. *Pattern Recognition Letters*, 31, 1216-1225.
- LIM, H. H., SWARTZ, A. A., YUEH, H. A., KONG, J. A., SHIN, R. T. & VAN ZYL, J. J. 1989. Classification of Earth Terrain Using Polarimetric Synthetic Aperture Radar Images. *J. Geophys. Res.*, 94, 7049-7057.
- LOMBARDO, P. & OLIVER, C. J. Optimal classification of polarimetric SAR images using segmentation. *Radar Conference*, 2002. Proceedings of the IEEE, 2002. 8-13.
- MDA. 2006. *Radarsat-2 overview* [Online]. MacDonald, Dettwiler and Associates Ltd. (MDA). Available: [http://www.radarsat2.info/rs2\\_satellite/overview.asp](http://www.radarsat2.info/rs2_satellite/overview.asp).
- MORIYAMA, T., URATSUKA, S., UMEHARA, T., MAENO, H., SATAKE, M., NADAI, A. & NAKAMURA, K. 2005. Polarimetric SAR image analysis using model fit for urban structures. *IEICE transactions on communications*, 88, 1234-1243.
- ORLANDO, J. R., MANN, R. & HAYKIN, S. 1990. Classification of sea-ice images using a dual-polarized radar. *Oceanic Engineering, IEEE Journal of*, 15, 228-237.
- PAL, N. R. & PAL, S. K. 1993. A review on image segmentation techniques. *Pattern Recognition*, 26, 1277-1294.

- PAPATHANASSIOU, K. 1999. *Polarimetric SAR interferometry*. PhD, University of Graz.
- PARK, S.-E. & MOON, W. M. 2007. Unsupervised Classification of Scattering Mechanisms in Polarimetric SAR Data Using Fuzzy Logic in Entropy and Alpha Plane. *Geoscience and Remote Sensing, IEEE Transactions on*, 45, 2652-2664.
- PELLIZZERI, T., LOMBARDO, P., OLIVER, C., SCIOTTI, M., MELONI, M. & MCCONNELL, I. A comparison of statistical segmentation technique for polarimetric SAR: region growing versus simulated annealing. *In: LACOSTE, H., ed. ESA PolinSAR workshop - Applications of SAR polarimetry and polarimetric interferometry (ESA SP-529), 2003 Frascati, Italy. Published on CDROM.*
- POTTIER, E. & FERRO-FAMIL, L. 2009. Exploration of ALOS-PALSAR SAR full-polarimetry data to the mapping of an African region. *Geoscience and Remote Sensing Symposium, 2008. IGARSS 2008. IEEE International. Cape Town, South Africa.*
- POTTIER, E. & LEE, J. S. 1999. Application of the H/A/ $\alpha$  Polarimetric Decomposition Theorem for Unsupervised Classification of Fully Polarimetric SAR Data Based on the Wishart Distribution. *The Committee Earth observing satellite (CEOS), SAR workshop. Toulouse, France: Paris: European Space Agency.*
- POTTIER, E. & POTTIER, J. S. 1999. Application of the H/A/ $\alpha$  Polarimetric Decomposition Theorem for Unsupervised Classification of Fully Polarimetric SAR Data Based on the Wishart Distribution. *The Committee Earth observing satellite (CEOS), SAR workshop. Toulouse, France: Paris: European Space Agency.*
- QIN, A. K. & CLAUSI, D. A. 2010. Multivariate Image Segmentation Using Semantic Region Growing With Adaptive Edge Penalty. *Image Processing, IEEE Transactions on*, 19, 2157-2170.
- REIGBER, A. 2001. *Airborne polarimetry SAR tomography*. PhD, University of Stuttgart.
- SANG-EUN, P. & MOON, W. M. 2007. Unsupervised Classification of Scattering Mechanisms in Polarimetric SAR Data Using Fuzzy Logic in Entropy and Alpha Plane. *Geoscience and Remote Sensing, IEEE Transactions on*, 45, 2652-2664.
- SATO, M., WATANABE, M. & IRIBE, K. Polarimetric SAR observation by ALOS. *Microwave Conference, 2007. APMC 2007. Asia-Pacific, 2007. 1-4.*
- SAVARESI, S., BOLEY, D., BITTANTI, S. & GAZZANIGA, G. Cluster Selection in Divisive Clustering Algorithms. *SIAM International Conference on Data Mining, 2002 Arlington, VA, USA. 299-314.*
- SCHEUCHL, B., CAVES, R., FLETT, D., ABREU, R. D., ARKETT, M. & CUMMING, I. 2004. The potential of cross-polarization information for operational sea ice monitoring. *ENVISAT & ERS symposium. Salzburg, Austria.*
- SHIMADA, M., ROSENQVIST, A., WATANABE, M. & TADONO, T. The polarimetric and interferometric potential of ALOS PALSAR. *In: LACOSTE, H., ed. ESA PolinSAR 2<sup>nd</sup> international workshop, 2005 Frascati, Italy. ESA Publications Division.*
- SINCLAIR, G. 1950. The Transmission and Reception of Elliptically Polarized Waves. *Proceedings of the IRE*, 38, 148-151.

- TIBSHIRANI, R., WALTHER, G. & HASTIE, T. 2001. Estimating the number of clusters in a data set via the gap statistic. *Journal Of The Royal Statistical Society Series B*, 63, 411-423.
- TOUZI, R., BOERNER, W. M., LEE, J. S. & LUENEBURG, E. 2004. A review of polarimetry in the context of synthetic aperture radar: concepts and information extraction. *Canadian journal of remote sensing*, 30, 380-407.
- TROUVE, E., PETILLOT, I., BOLON, P., GAY, M., BOMBRU, L., NICOLAS, J. M., TUPIN, F., WALPERSDORF, A., COTTE, N., HAJNSEK, I. & KELLER, M. 2008. Monitoring alpine glacier activity by a combined use of TerraSAR-X images and continuous GPS measurements-the Argentiere glacier experiment. *The 7<sup>th</sup> European conference of synthetic aperture radar*. Friedrichshafen, Germany.
- TZOTSOS, A. & ARGIALAS, D. 2006. MSEG: A Generic region-based multi-scale image segmentation algorithm for remote sensing imagery. *The American society for photogrammetry and remote sensing (ASPRS) conference*. Reno, Nevada, USA.
- VAN ZYL, J., CARANDE, R., LOU, Y., MILLER, T. & WHEELER, K. The NASA/JPL Three-frequency Polarimetric Airsar System. Geoscience and Remote Sensing Symposium, 1992. IGARSS '92. International, 1992. 649-651.
- VAN ZYL, J., ZEBKER, H. & ELACHI, C. 1987. Imaging radar polarization signatures: theory and observation. *radio science*, 22, 529-543.
- YU, P. 2009. *Segmentation of RADARSAT-2 dual-polarization sea ice imagery*. Master, University of Waterloo.
- ZEBKER, H. A. & GOLDSTEIN, R. M. 1986. Topographic Mapping From Interferometric Synthetic Aperture Radar Observations. *J. Geophys. Res.*, 91, 4993-4999.
- ZHANG, L., ZOU, B., ZHANG, J. & ZHANG, Y. 2010. Classification of polarimetric SAR image based on support vector machine using multiple-component scattering model and texture features. *EURASIP journal on advances in signal processing*, 2010, Article ID 960831, 9.